TÉCNICO LISBOA

Trip and History-based range prediction for a light powered vehicle based on real-world data

David Martins Neto

Thesis to obtain the Master of Science Degree in

Engineering Physics

Supervisor(s): Prof. Dr. Horácio João Matos Fernandes
Prof. Dr. João Filipe Pereira Fernandes

Examination Committee

Chairperson: Prof. Dr. João Pedro Saraiva Bizarro
Supervisor: Prof. Dr. Horácio João Matos Fernandes
Member of the Committee: Prof. Dr. Paulo José da Costa Branco

October 2020

To my parents.

Agradecimentos

Em primeiro lugar agradeço aos meus orientadores, proferssor Horácio Fernandes e o professor Jõao Fernandes por todo apoio durante este trabalho. Sem eles certamente este trabalho não teria acontecido. Em particular agradecer ao professor Horácio Fernandes pela disponibilização da mota que foi usada para o teste.

Seguidamente gostaria de agradecer à *ColourTrip* pela disponibilização do material e do *e-tuk* para a aquisição de dados. Um agradecimento especial também ao Miguel Fernandes por toda a ajuda.

Gostaria tambem de agradecer ao pessoal to laboratório do IFPN, em particular ao Rui Dias, e ao Pedro Lourenço pelo apoio durante o teste do sistema de dados.

Finalmente um agradecimento mais geral aos meus pais pelo apoio incondicional durante toda a vida. E a todos os outros companheiros desta viagem a que chamam vida.

Resumo

O foco principal deste trabalho é o alívio da ansiedade de alcance no contexto de veículos elétricos usando dados reais de um ciclomotor elétrico de três rodas.

Dado isto, o banco de baterias de chumbo original foi substituído por um banco de baterias de lítio, atingindo-se um ganho de 25% na autonomia do veículo. Um sistema de aquisição de dados foi desenvolvido e integrado no novo banco de baterias. Este sistema foi usado para a gravação das coordenadas geográficas obtidas de um recetor GPS, e de informação relativas às baterias proveniente do BMS.

Os dados adquiridos foram usados para testar métodos para alívio da ansiedade de alcance com base na viagem e no histórico. Os primeiros usaram modelos físicos e estatísticos para a previsão do consumo do veículo, para viagens com diferentes durações. De entre os primeiros, o método de regressão obteve os melhores resultados com 3% de erro médio e 13% de desvio padrão dos erros para viagens de 150s. Dos métodos estatísticos, os melhores resultados obtiveram-se com a regressão com árvores de decisão, obtendo-se 1% de erro médio e 26% de desvio padrão para viagens de 150s.

Os métodos com base no histórico usaram médias móveis para prever o alcance remanescente do veículo. Neste trabalho a média móvel considerou duas janelas uma com duração constante e outra com distância percorrida constante. Para uma janela de 2h45min foi obtido 8.1% de erro médio com 19.7% de desvio padrão. Para uma janela de 80km foi obtido 2% de erro médio e 8.2% de desvio padrão.

Palavras-chave: veículos elétricos, BEV, mobilidade intiligente, previsão de alcance, modelação de veículos, ciencia de dados.

Abstract

The present work focuses on alleviating the range anxiety in the context of electric vehicles using real world-data collected in a light powered vehicle.

To do this, the original lead-acid battery pack of the vehicle was changed into lithium-ion, achieving a 25% gain in autonomy. A data acquisition system was also developed and integrated with the new battery pack recording global position data from a GPS receiver and battery information from the Battery Management System.

The data collected was then used to test trip and history-based methods to alleviate range anxiety. The trip-based methods used both physical and statistical models to predict the energy consumption of varying duration trips. In the physical models the best results were obtained with the regression, which achieved 3% average error and 13% error standard deviation, for 150s segments. From the statistical models the best results were obtained with the decision tree regression with a 1% average error and a 26% error standard deviation, for 150s segments.

The history-based methods used moving averages to predict the remaining driving range of the vehicle. In this work, the moving average was made in a constant time window as well as in a constant distance window. For a constant time window of 2h45min it was obtained a 8.1% mean error with 19.7% standard error deviation. For the constant distance window of 80km it was possible to obtain a average error of 2% and a standard error deviation of 8.2%.

Keywords: electric vehicles, BEV, smart mobility, range prediction, vehicle modelling, data science.

Contents

Agradecimentos v
Resumo vii
Abstract ix
List of Tables xv
List of Figures xvii
Nomenclature xxi
Glossary xxiii

1 Introduction **1**
1.1 Motivation 1
1.1.1 Electric Vehicle Market 1
1.1.2 The role of light vehicles 2
1.1.3 Is Range Anxiety A Problem? 3
1.2 Solving Range Anxiety 4
1.2.1 Trip-Based Methods 4
1.2.2 History-Based Methods 5
1.3 Objectives 5
1.4 Outline 6

2 Vehicle Modelling **7**
2.1 Physical Model 7
2.1.1 Lumped Mass Model 9
2.2 Statistical Models 14
2.2.1 Decision Trees Regression 14
2.2.2 K-Nearest Neighbours Regression 15

3 Data Collection **17**
3.1 Vehicle Properties 17
3.1.1 *e-tuk* General Properties 18
3.1.2 Gear Ratio 19
3.1.3 Controller Configuration 20
3.1.4 Mass Estimation 20

3.2 Data Acquisition System . . . 21
3.2.1 BMS reverse-engineering . . . 21
3.2.2 Hall Sensor Set-up . . . 23
3.2.3 Experimental Set-up . . . 24
3.2.4 Data Acquisition Software . . . 25
3.2.5 Server Page . . . 27
3.2.6 Testing Results . . . 27
3.3 Battery Setup . . . 29
3.3.1 Batteries . . . 29
3.3.2 Compartment Wiring . . . 30
3.3.3 Mechanical Design . . . 31

4 Preliminary Analysis of the Data Collected **34**
4.1 Measured Features . . . 34
4.1.1 Feature Distributions . . . 35
4.1.2 Geographical Feature Distribution . . . 36
4.1.3 Consumption Curve . . . 37
4.2 Derived Features . . . 40
4.2.1 Real Time . . . 40
4.2.2 Aggregated Data . . . 43

5 Trip-Based Prediction **45**
5.1 Model Evaluation . . . 46
5.2 Input Data . . . 46
5.3 *A priori* Physical Model . . . 48
5.4 *A priori* Physical and Electrical Model . . . 49
5.4.1 Efficiency Map Estimation . . . 49
5.4.2 Power Consumption Estimation . . . 51
5.5 Regression Model . . . 51
5.5.1 Results and Discussion . . . 53
5.6 Statistical Models . . . 55
5.6.1 Decision Trees . . . 56
5.6.2 K-Nearest Neighbours . . . 56
5.7 Model Comparison . . . 58

6 Real Time Approach **61**
6.1 Moving Average . . . 61
6.2 Data Selection . . . 63
6.3 Calibration . . . 63
6.4 Time Window . . . 64

6.4.1 Model Evaluation 65
6.5 Distance Window 68
6.6 Model Comparison 69

7 Conclusions **70**
7.1 Achievements 70
7.2 Future Work 72

Bibliography **72**

A Controller Configuration **79**

B Data Format **81**

C Technical Drawings **82**
C.1 Batteries 82
C.2 Connectors 82
C.3 Battery Compartment 84
C.4 Holding Bars 84
C.5 Assembly 85

List of Tables

2.1 Expected lumped mass model vehicle parameters for the **e-tuk Limo GT** vehicle. 13

3.1 Vehicle data for the **e-tuk Limo GT** taken from the original brochure. The values shown are valid for the original lead-acid battery pack, and some changes are expected for the new battery pack[50]. 19
3.2 **e-tuk Limo GT** motor characteristics. 20
3.3 Battery Menu controller parameters 20
3.4 BMS serial communication parameters 22
3.5 Comparison between the **lead-acid** and the **lithium-ion** battery packs used in the **e-tuk Limo GT**. 30

4.1 Summary of the key features of the data collected. 35

5.1 Features used in the physical models and respective expressions. 47
5.2 Features used in the statistical models and respective expressions. 47
5.3 Coefficients sed in the the *a priori* model of **e-tuk Limo GT**. 48
5.4 Equations of the three regression models used. 53
5.5 Average and standard deviation of the error values for the different methods for segments of duration of 150s. 60

6.1 Mean and Standard Deviation of the R^2. 69
6.2 Mean and Standard Deviation of the relative error. 69

7.1 Average and standard deviation of the error values for the different methods. 71
7.2 Mean and Standard Deviation of the relative error. 71

A.1 Battery Menu controller parameters 79
A.2 Current Limits controller parameters 79
A.3 Throttle Configurations controller parameters 79
A.4 Brake Configurations controller parameters 80

B.1 Table containing the decoding of the serial communication protocol of the BMS. The **Byte Nr** stats at zero. 81

List of Figures

1.1 Expected evolution of the global passenger cars and light duty vehicles sales, as well as market share of electric vehicles in the next decade[5]. 2

2.1 Schematic representation of the battery-to-wheel energy flow (P_{bat} represents the **battery power**, P_{aux} the **auxiliaries power**, P_{mec} the **mechanical power** and η the **drive-train efficiency**). The size of the box is a visual indicator of the relative power reaching each component 8

2.2 Schematic representation of the wheel-to-battery energy flow (P_{bat} represents the **battery power**, P_{aux} the **auxiliaries power**, P_{mec} the **mechanical power** and η the **drive-train efficiency**). The size of the box is a visual indicator of the relative power reaching each component 8

2.3 Example of an efficiency map of a motor as a function of the rotational frequency and the torque [34]. This map concerns a motor with peak power of 47kW, peak torque of 180 Nm and maximum velocity of 8000 RPM. 9

2.4 Graphical representation of forces acting on the vehicle adapted from [44]. (F_t - traction force, F_r - rolling friction, F_a - aerodynamic friction, F_g - gravitational force) 9

2.5 Rolling friction coefficients for different pavements as a function of the tire pressure [44]. . 12

2.6 Comparison between the force magnitudes for the **e-tuk** parameters in table 2.1 as a function of the angle and the velocity. 14

2.7 Example of a decision tree built using the **decision tree regression model** for 50s trip segments with max depth = 2. 15

2.8 Example of how the KNN algorithm works. Points in the training set (blue) that are used in the weighted average prediction of the unknown point (red) are inside the circle for two different values of K. 16

3.1 Pictures of the vehicles used. 18

3.2 Energy consumption versus distance travelled for all the days of data acquired. The linear model obtained had ($A = 1.85 \pm 0.05$ Ah/km), $R^2 = 0.97$ 19

3.3 Original **e-tuk Limo GT** plate on the motor. 20

3.4 Photo of a similar BMS to the one used in the vehicle. 22

3.5 Screen-shot of the Mobile application measurements. It should be noted that the labels in the mobile application were not correct. In appendix B it is shown the correct correspondence of labels. . . . 22
3.6 Wiring diagram for the test of the request message sent from the screen. . . . 22
3.7 Schematic of the connection to the BMS for testing. . . . 23
3.8 Hall Sensor circuit . . . 23
3.9 Waveform of the Hall signal after the circuit 3.8 . . . 24
3.10 Oscilloscope output for the test of the number of poles of the motor. . . . 24
3.11 Schematic of the wiring used for testing the data acquisition system . . . 25
3.12 Schematic of the wiring in the main set-up used. . . . 26
3.13 Inheritance Scheme of the python classes implemented. The arrow is pointing from the class to the class it inherits from. The **FullLogger** class contains one class of each of others, while not inheriting from them. . . . 27
3.14 Screenshot of the webpage hosted in the *Raspberry Pi* . . . 28
3.15 Example of data collected in thhe **e-max** motorcycle during the tests. . . . 28
3.16 Measured consumption for the **e-max** as a function of the vehicle velocity. . . . 29
3.17 Expected Range for the **e-max** motorcycle as a function of the velocity. . . . 29
3.18 Pictures of the two battery packs used in the **e-tuk Limo GT**. . . . 30
3.19 Wiring diagram inside the $LiFePO_4$ battery compartment . . . 31
3.20 BMS wiring scheme in the $LiFePO_4$ battery pack. . . . 31
3.21 Isometric Views of the battery compartment. . . . 32
3.22 Isometric Views of the battery compartment. . . . 32
3.23 Isometric view of the fuse connector . . . 32
3.24 Exploded view of the battery compartment assembly. . . . 33
3.25 Isometric view of the assembled battery compartment. . . . 33

4.1 Distribution of the measurement of the vehicle velocity for the data collected in the vehicle. 35
4.2 Power distribution of the measured data points. . . . 36
4.3 Distribution of the measured current for the vehicle movement. . . . 36
4.4 Distribution of the total voltage values. . . . 36
4.5 Geographical distribution of the GPS height measurements . . . 37
4.6 Estimated Height of the points as a function of the coordinates . . . 38
4.7 Geographical distribution of the error in the height . . . 38
4.8 Average Measured Velocity for the different point coordinates . . . 38
4.9 Average Measured power for the different coordinate points . . . 39
4.10 Average consumption as a function of the velocity of the vehicle for the **e-tuk Limo GT** vehicle. . . . 39
4.11 Average expected remaining driving range as a function of the velocity of the vehicle for the **e-tuk Limo GT** vehicle. . . . 39

4.12 Elevation graph for the Lisbon Area considered in the *Copernicus* dataset. 41
4.13 Geographical distribution of the height values. 41
4.14 Altitude values measured using the GPS receiver (above), and the altitude values predicted using the topographical map (below). 41
4.15 Slope estimation (above) and altitude profile (below) in an example vehicle trajectory. The slope estimation considered used 30 past points, which correspond to 9s of data acquisition. 42
4.16 Representation of the X, Y and Z axis. 43

5.1 R^2 variation with the trip segment duration for the **physical model** (x axis not to scale). . 49
5.2 Relative error distribution for trips with $\Delta E > 1AH$. Average error was -32% and the standard deviation 27% 49
5.3 Different representations of the estimated efficiency maps of the motor of the **e-tuk Limo GT**. 50
5.4 Regenerative braking efficiency during regeneration using a gaussian filter. 51
5.5 Three examples of consumption values estimated for the full lumped mass model. 52
5.6 Three examples of consumption values estimated for the lumped mass model without gravity. 52
5.7 R^2 values as a function of the trip segment for the three models considered. 54
5.8 Details of the estimated model parameters for different trips and different segment lengths 54
5.9 Relative error distribution for trips with $\Delta E > 1AH$. Average error was -3% and the standard deviation 13% 55
5.10 R^2 curves for the different parameters of the Decision Tree model, as a function of the trip length. 57
5.11 R^2 for different trip durations for the Decision Tree model 58
5.12 Relative error distribution for trips with $\Delta E > 1AH$ using the KNN model. Average error was 1% and the standard deviation 26% 58
5.13 R^2 curves for the different parameters of the KNN model, as a function of the trip length. . 58
5.14 R^2 for the final KNN model as a function of the trip duration considered. (X axis not to scale) 59
5.15 Relative error distribution for trips with $\Delta E > 1AH$ using the KNN model. Average error was 7% and the standard deviation 52% 59
5.16 Joint Representation of the R^2 for all the models that were used to describe the vehicle as a function of the trip segment duration. 59

6.1 Example of the velocity measurements for a vehicle at rest 63
6.2 Examples of range predictions and measurements without calibration. 64
6.3 Example of a graph of the calibration 64
6.4 Examples of preliminary range predictions and measurements. 65
6.5 Consumption values for different moving average windows. 66
6.6 Examples of the range prediction profile for two different time windows. 66
6.7 Evolution of the R^2 as a function of the window used. 67

6.8 Values of the mean error and standard deviation of the error values for various time windows. 67
6.9 Evolution of the R^2 values for the constant distance window moving average as a function of the window considered. 68
6.10 Examples of the range prediction profile for two different time windows. 68

7.1 Relative error distribution for trips with $\Delta E > 1AH$. Average error was -3% and the standard deviation 13% 71

C.1 Technical drawings concerning the batteries used in this work. 82
C.2 Technical drawings concerning the horizontal connector. 82
C.3 Technical drawings concerning the vertical connector. 83
C.4 Technical drawings concerning the fuse connector. 83
C.5 Technical drawings concerning battery compartment. 84
C.6 Technical drawings concerning the L-shaped bar. 84
C.7 Technical drawings concerning T-shaped bar. 85
C.8 Technical drawings concerning The full assembly. 85

Nomenclature

Greek symbols

α	Slope of the road
β	Linear regression coefficients
λ	Latitude
λ_m	Average Latitude
μ	Static friction coefficient
ω	Angular frequency of rotation of the motor
ϕ	Longitude

Roman symbols

Δs_{total}	Total Distance travelled by the vehicle.
Δs_{xy}	Horizontal Distance travelled by the vehicle.
ρ_{air}	Air Density.
a	Vehicle acceleration
A_f	Frontal Area.
C_D	Drag Coefficient.
E_R	Earth Radius
F_g	Gravitational Force.
F_t	Traction Force.
F_a	Aerodynamic Force.
F_r	Rolling Friction.
F_{tot}	Total Force.
g	Gravitational Constant

h	Height of the vehicle
m	Vehicle mass
P	Power
r	Total distance covered by the vehicle
R_w	Radius of the wheel of the vehicle
T	Torque acting on the motor
t	Time
v	Vehicle Velocity
v_w	Wind Velocity.
x	Horizontal distance covered by the vehicle

Subscripts

x, y, z	Cartesian components.

Glossary

BEV A Battery Electric Vehicle is a vehicle whose only energy source is electric energy.

BMS A Battery Management System is an electronic device used to protect the battery cells and keep them from working outside their safe operating area

CFD Computational Fluid Dynamics is a branch of fluid mechanics that uses numerical methods and algorithms to solve problems that involve fluid flows.

EU European Union is a political and economic union of several countries primary located in Europe

EV An Electric Vehicle is a vehicle that uses electric energy as power source, through an electric motor.

GPS Global Positioning System is a satellite based navigation system used to find the position in the globe.

ICE Internal Combustion Engine vehicles use an internal combustion engine as the only power source for its motion.

PHEV Plug-in Hybrid Electric Vehicles are vehicles that use in their propulsion an internal combustion engine and an electric motor, while also providing the option of recharging the battery component

PHEV Plug-in Hybrid Electric Vehicles are vehicles that use in their propulsion an internal combustion engine and an electric motor.

RDR Remaining Driving Range is the expected distance that a vehicle is expected to drive until it runs out of fluid

SOC State Of Charge of the battery is the amount of energy it is still possible to extract from it at any given time.

UART Universal Asynchronous Receiver/Transmitor is device that allows the asynchronous serial communication.

Chapter 1

Introduction

1.1 Motivation

Following the 2016 Paris agreement, 195 countries committed to keep the global temperature rise below the 2 degree mark. In order to do that, the greenhouse gas emissions have to decrease drastically worldwide. The transportation sector, responsible for one fourth of the CO_2 emissions[1], will need to go through profound changes.

The European Union (EU) white paper concerning mobility and transport, containing the EU Guidelines for the transportation sector, mandates a decrease in 60% of greenhouse gas emissions by 2050[1]. This requires the widespread replacement of the internal combustion engine (ICE) vehicles with the cleaner electric vehicles (EV), which make use of electric engines to provide the propulsion energy.

It is possible to divide electric vehicles into hybrid vehicles (HEV), which use both the internal combustion and electric engines, plug-in hybrid (PHEV), which are HEV with the added ability to provide electricity through charging, and battery electric vehicles (BEV), which only are only electrically powered. Out of the different EV types, the most promising are the BEV, as they are completely electric and have zero tailpipe emissions. However, BEV emissions depend heavily on the energy mix used to produce the electricity they consume. As of 2019 it is estimated that 52% of life-cycle emissions for a BEV are due to non-renewable electricity production[2].

The shift towards both electric mobility and de-carbonization of the energy grid are fundamental. Following the COVID-19 crisis, the economic recovery strategy for Portugal has called for the increase in economic electrification as well as the move of both the industrial and transportation sectors towards cleaner energy sources[3]. With the expected increase in private vehicle traffic, together with the added need for public transportation complying with social distancing measures, mobility will have to be rethought while keeping this shift in mind[2].

1.1.1 Electric Vehicle Market

The automotive market plays a very important role in the economy of EU. Employing 14.6 million people, it represents 6.7% of all its employment[4]. The EU alone makes up for around 20% of the world

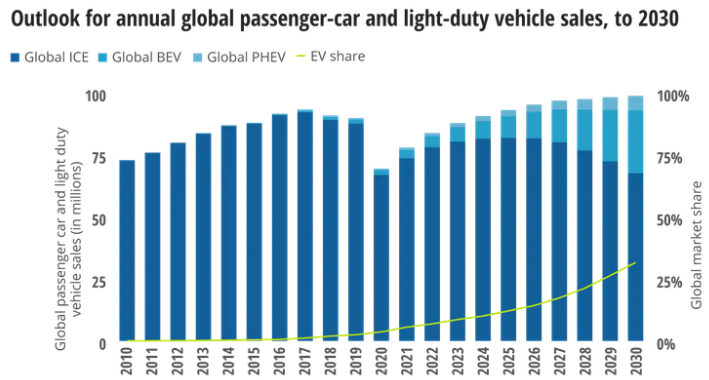

Figure 1.1: Expected evolution of the global passenger cars and light duty vehicles sales, as well as market share of electric vehicles in the next decade[5].

production of vehicles, and is still a major player in the worldwide vehicle manufacturing and sales.

In particular, the electric vehicle market has shown a considerable increase in the last two years. Only last year (2019), 2.1 million electric cars were sold, surpassing 2018 which was already a record year with one million sales and [1] around 75% of these were BEV[2].

In the wake of the recent COVID-19 pandemic, the automotive market suffered a big crash with diminishing sales across the world. However, in Europe during April, when the effects of the pandemic were the largest, EV sales in Western Europe fell just by 31%, with some countries actually reporting a small growth compared to the previous year [5].

A recent report on the state of the EV market predicts that despite its contraction, the electric vehicle sales are expected to match the values before COVID-19 by 2024. Furthermore, they are expected to keep rising throughout the decade at the cost of decrease in ICE vehicle sales, reaching 30% market share by 2030[5].

1.1.2 The role of light vehicles

Up to this point, only the market concerning electric cars has been discussed. However both of the vehicles used in the present work are light powered vehicles belonging to the L category in the European standards[6, 7].

While the electric car market is growing, the light powered vehicle market has done even more so. It is estimated that 350 million electric two- and three-wheelers are in existence on the world, making up 25% of the global stock of two- and three-wheelers[2]. The majority of these are in China where the use of two-wheelers with combustion engine is banned inside cities. Because of their smaller size and consumptions, light powered vehicles are prime candidates for electrification. They are often urban vehicles and travel shorter distances at lower velocities, requiring relatively small battery packs[2].

The main vehicle studied in the present work is commonly known in India as an *auto rickshaw*, but is also known as *tuk-tuk* in Egypt and Thailand. In Asian countries, this type of three-wheeler is widespread; they function as a taxi service and touristic vehicles but also as private and cargo

[1] This number includes not only battery electric vehicles (BEV) but also plug-in hybrid (PHEV).

transport[8]. In India alone there are 2.5 million of these vehicles[9]. In recent years, *tuk-tuks* have been gaining popularity throughout Europe and particularly in Lisbon they are often seen making tours throughout the city centre, contributing to the touristic ecosystem of the city[10].

Despite the prominence of auto rickshaws throughout south-east Asia and some African countries, there is still a considerable lack of studies focusing on them. One study based on simulations was found [11], as well as another focusing on the design of a solar rickshaw [12]. However, no studies were found to use real-world data to estimate the consumption of these types of vehicles, which was the chosen approach in this work.

1.1.3 Is Range Anxiety A Problem?

Electric vehicle technologies have shown significant improvements in the last decade. The battery density of the vehicles is as large as ever, the charging time as low as ever, and the charging grid as dense as it ever was. However, there are several factors still holding back the widespread EV adoption. A survey made in 2018 by **Delloite** showed that the three main concerns of EV costumers were, range, cost and charging infrastructure[13]. Other studies also show prominent concerns with the vehicle range[14].

These three problems are related; essentially the denser the charging infrastructure is, the smaller the vehicle range needs to be given the easier access to a charging point. In addition, the bigger the range of the vehicle the more it generally costs. The present dissertation focuses on developing ways of alleviating the costumer concerns with the vehicle range. This costumer apprehension regarding the vehicle range is caused by a phenomenon known as range anxiety.

Range anxiety can be defined as the fear that the driver has of not being able to reach the destination because of the finite range of the vehicle[15]. This effect arises from the mismatch between the costumer vehicle usage and the vehicle range. In other words, it is caused by the difference between the distance that the driver needs to cover and the range available to him. Two question can now be asked: How long does the costumer actually need to travel and can an electric vehicle cover that distance?

Several consumer surveys have shown that around 50% of the costumers would be satisfied with a vehicle that could cover 450km in a single charge [14], [5]. But they show a considerable amount of costumers that require bigger ranges. Other studies have actually measured the length of the trips to find that in the average daily travelled distance was around 45km[16], which can be covered with a commercial BEV. In another study is shown that although the average daily trip can be covered using an EV, the driver on average wouldn't have enough range for 5% of the trips. Because of this, people with only one vehicle will prefer ICE over BEV [17]. Several studies used test drivers to measure the reaction to EV use and found that this fear is most prevalent in inexperienced drivers[18, 19].

Despite the increase in range of BEVs, there is still a mismatch between the needs of the consumer and the range available. This leads to range anxiety and will be the most prevalent in vehicles with lower range. As this anxiety is mostly felt by inexperienced drivers, it is important to eliminate it in order to make the transition towards electric mobility possible.

1.2 Solving Range Anxiety

The most obvious way of solving range anxiety is to increase the range of the vehicle to fulfil all of the costumer needs. This is happening today as EV technology gets better with the improvement of both efficiency and battery energy densities. However, state of the art vehicle technology is reflected in the price of the vehicle, which is the second biggest costumer concern. If we are to push for widespread use of electric vehicle, the range anxiety problem has to be solved for lower range vehicles, which are more affordable.

Another way of solving the range anxiety problem is to provide the driver with accurate information about the vehicle consumption and its available range. In order to do this, two major approaches exist [20].

The first is through early planning of the trips. For a given route, several methods can be used to predict the energy consumption over the whole trip, with a larger or smaller degree of complexity. These methods can be classified as trip-based and have been shown to reduce range anxiety [19].

The second does not involve early planning of the trip. It uses instead only the past consumption of the vehicle to predict the future behaviour. Because of this they are called history-based methods. They often are less accurate than the trip based methods mainly because they do not have access to the road topology, which is one of the most determinant factors in the vehicle consumption.

In the following section, a comprehensive review of the previous studies is provided using both trip-based and history-based methods and how they relate to the present work. Most of the studies found in literature focus on trip-based methods, because of their better performance, but there is still a considerable sample of history-based methods.

1.2.1 Trip-Based Methods

Several studies have been found where trip-based methods are applied to predict the energy consumption of road vehicles. In order to do this, several types of models can be built. The models can be split into two categories: physical and statistical models. The former attempts to provide the most accurate vehicle representation by using physical laws to describe each part of the vehicle. The latter, instead combines statistical methods and measurements from the vehicle to provide an accurate description. In the following paragraphs we make a fast overview of the models built as well. The detailed description of the methods used is only made in chapter 2.

The physical models are often split into smaller sub-models of the interacting parts of the vehicle. To model the vehicle *chassis* the most common model used is the lumped mass model, which is used in more than ten studies [11, 21–33]. To model the *power-train*, some studies use theoretical models [11, 23, 25] and others use experimental look-up tables[31, 34]. Some studies did not consider the varying power-train efficiency[32, 33].

This model is very often used in the context of vehicle simulations, as in the case of [11, 23–25, 32, 34], but it has also been used in the context of real world data [31, 33]. Several studies have considered multiple linear regression models to extract the vehicle behaviour [21, 33, 35]. Both of these models are

able to extract consistent model parameters for the vehicle.

It is common to find trip-based studies in the context of a route-planner service. In several studies algorithms have been developed to find the minimum consumption path of the vehicle [29, 30, 36]. In some of this studies the integration with the *Google Maps* API was made [29].

On one hand, several statistical models can also be built to describe both the vehicle and the driver behaviours. These models are often advantageous because they do not need to have accurate estimation of the model parameters, which removes the need for laboratory vehicle testing. On the other hand, they rely on the availability and accuracy of collected data.

The statistical models considered to solve the regression problem are often non-linear. For instance, *decision trees* for regression were used in [29]. In [28, 29, 37] neural networks are used and [38] uses K-Nearest Neighbours (KNN) models. In addition to this, [39] uses clustering to make the range prediction by subdividing the route in several segments. Finally, several stochastic methods are used in [40] to predict the energy spent in a route segment.

1.2.2 History-Based Methods

There are several studies concerning history-based methods in the literature. The most common way of estimating the vehicle consumption is through the usage of a moving average. In [41] the calculation is made using a moving average and it is concluded that the most important value to use is the window value of the moving average, which is taken as constant. In [42] several moving averages are blended to converge to a single measurement. In [43] the vehicle range is predicted using both a moving average of the previous values in combination with a regression model, whose dependent variables are related to the destination of the vehicle.

1.3 Objectives

The main goal of this master thesis is to solve the range anxiety problem outlined in the previous sections. Contrary to a considerable portion of previous studies, this work will focus on real-world data collected from a fully electric vehicle, instead of vehicle simulations.

With this in mind, the present work can be divided into three different parts. The first part was the conversion of the battery pack of the vehicle used from the original lead-acid batteries to new lithium-ion batteries. This involved the modification of the previous battery compartment to hold the new batteries as well as devising the new wiring of the previous batteries.

The second part of the work consists in building the data acquisition system in order to collect and log important features in the course of the vehicle movement. In general, the information regarding the battery pack will be collected from the Battery Management System (BMS) and combined with information regarding the vehicle position from a GPS receiver using a *Raspberry Pi*.

In the final part of the work, the collected data will be analysed and used to test different methods of solving range anxiety. Both trip- and history-based methods are tested, using in the first several physical

and statistical methods and in the second a moving average based method.

1.4 Outline

In the present chapter the motivation, the problem context, as well as a overview of the most common methods were provided. In chapter 2 the vehicle models used to eliminate the range anxiety are detailed. This chapter explores both the physical model used as well as the different statistical models. Chapter 3 contains the information regarding how the data acquisition system was implemented and tested, showing details concerning both hardware and software implemented. The new battery pack set-up is also described in this chapter. In chapter 4, a preliminary analysis of the data collected is performed. The distribution of the features considered, as well as their evolution as a function of the vehicle coordinates are explored. In chapter 5, the trip-based energy predictions are described, followed by a discussion of the results. In chapter 6, the implementation of the history-based range prediction is shown and the results are also discussed. Lastly, in chapter 7, the main achievements and conclusions are summarised and suggestions for extensions of this work are given.

Chapter 2

Vehicle Modelling

To make an accurate consumption prediction it is important to have a accurate model of the vehicle. The models described in this section were used throughout chapter 5 in the predictions of the energy spent in a given trip. Therefore the methods described obey the general form of equation 2.1, where ΔE is the total energy spent in a trip, x_i are trip features such as the distance travelled, average velocity etc., and f_j can represent any of the models used.

$$\Delta E = f_j(x_1, ...x_n) \tag{2.1}$$

The two main types of model that were used are physical models, which describe the vehicle using physical principles, and the statistical models that use statistical methods to estimate its consumption.

The present chapter will describe the models used in the trip-based predictions of energy. The first section describes the lumped mass model, which lays the foundation for the physical trip-based methods in section 5.3. In this section a description of the forces and typical parameters considered in the model is provided. The second section describes the two statistical data-driven methods also implemented. To perform the estimation of the spent energy it is made use of decision tree and K-nearest neighbours (KNN) regression algorithms.

2.1 Physical Model

In figure 2.1, a simplified representation of the battery-to-wheel energy flow in a fully electric vehicle is shown. The batteries contain the energy that the vehicle will spend throughout its movement. They are connected to the motor controller, which then feeds energy to the motor. The motor, in turn, generates torque that is transmitted to the driving shaft and finally to the wheels. In each of the energy conversion steps, there are energy losses that need to be modelled. In figure 2.1 it can also be seen that the controller feeds energy to the auxiliary systems, which are systems external to the vehicle movement that are only auxiliary but not fundamental to the vehicle movement. For the remainder of this work, the auxiliary power is discarded because its contribution is small when compared with the other terms. When regenerative braking happens, the power runs from wheels to the battery, also with loss energy in

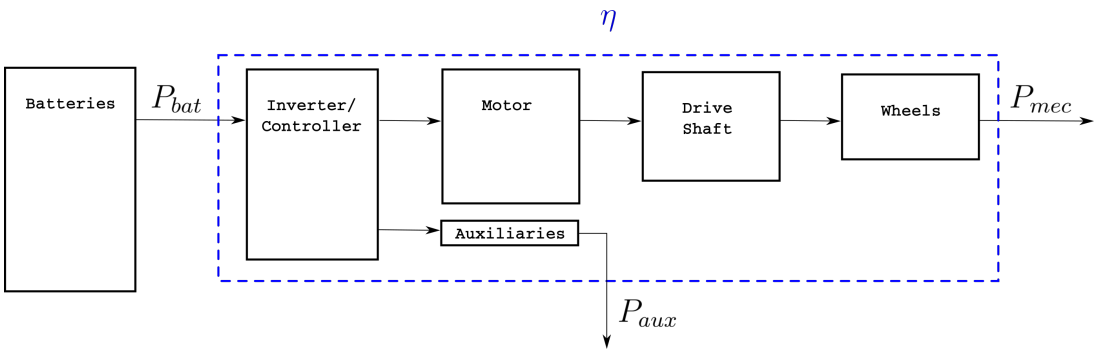

Figure 2.1: Schematic representation of the battery-to-wheel energy flow (P_{bat} represents the **battery power**, P_{aux} the **auxiliaries power**, P_{mec} the **mechanical power** and η the **drive-train efficiency**). The size of the box is a visual indicator of the relative power reaching each component

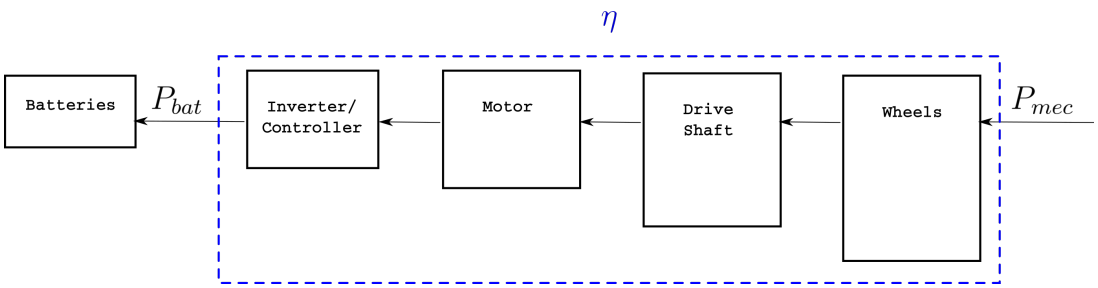

Figure 2.2: Schematic representation of the wheel-to-battery energy flow (P_{bat} represents the **battery power**, P_{aux} the **auxiliaries power**, P_{mec} the **mechanical power** and η the **drive-train efficiency**). The size of the box is a visual indicator of the relative power reaching each component

each transition, as shown in figure 2.2.

In some studies battery models have been developed in order to predict the SOC of the battery. In this work it was tried but using a Kalman Filter, but with no success and the SOC prediction used ended up being the one provided by the BMS.

Of the components in the vehicle, the one that will affect the vehicle consumption the most is the motor. The electric motor changes its efficiency significantly depending on the torque and rotational frequency. Due to this, it is common to use efficiency maps as look up tables to find the efficiency for each torque and velocity value. An example an efficiency map is shown in figure 2.3.

As shown in figure 2.1 the efficiencies of the inverter, the controller, the motor and drive shaft were grouped in a single value. The efficiency is then given by equation 2.2. As it includes the motor efficiency, it will also depend on the rotational frequency and output torque.

$$\eta(T, \omega) = \frac{P_{mec}}{P_{bat}} \tag{2.2}$$

The power output in the battery terminals is often the consumption value that can be measured. To estimate the mechanical power a model of the chassis of the vehicle is needed.

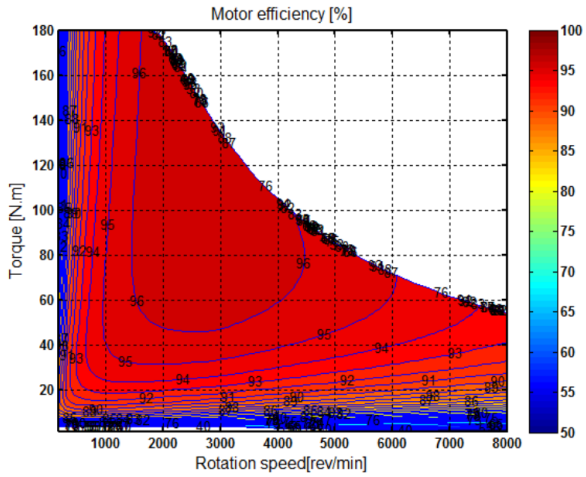

Figure 2.3: Example of an efficiency map of a motor as a function of the rotational frequency and the torque [34]. This map concerns a motor with peak power of 47kW, peak torque of 180 Nm and maximum velocity of 8000 RPM.

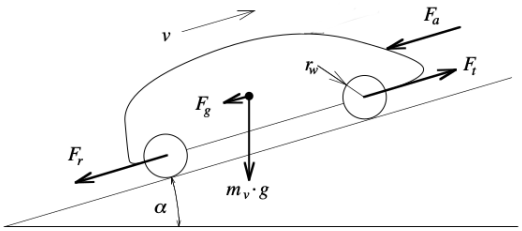

Figure 2.4: Graphical representation of forces acting on the vehicle adapted from [44]. (F_t - traction force, F_r - rolling friction, F_a - aerodynamic friction, F_g - gravitational force)

2.1.1 Lumped Mass Model

As seen in equation 2.2, the power measured in the batteries is proportional to the mechanical power (P_{mec}) provided to the vehicle. The most common physical model to predict this power is the the lumped mass model.

This is a relatively simple model of the vehicle that summarises most of the factors affecting its movement. It relies on the approximation that all the forces are acting in the centre of mass of the vehicle and it is a computationally efficient model, having been used in real-time approaches. Different types of lumped mass models have been successfully used in previous studies, as in [21–29], just to name a few.

There are three main forces considered in these models: the gravitational force (F_g), the rolling friction (F_r), the aerodynamic friction (F_a), and to balance them, the traction force (F_t) applied by the motor. A schematic representation of these forces is shown in figure 2.4.

Considering the forces in the lumped mass model, and applying Newton's second law of motion to the vehicle it is possible to obtain the main equation of the model shown in 2.3, where m_v is the mass

and $v(t)$ is the velocity of the vehicle[44].

$$m_v \frac{d}{dt} v(t) = F_t(t) - (F_a(t) + F_r(t) + F_g(t)) \tag{2.3}$$

In the following section, the forces considered in the model are discussed. A general expression to calculate each of them is provided and the parameters they depend on are discussed. Other effects that were not modelled but may affect the results are also addressed.

Aerodynamic Forces

A major influence in the motion of the road vehicles are the aerodynamic forces. These forces arise from the resistance the air applies on the vehicle as it moves. They are caused by the difference of the velocity of the vehicle and the velocity of the surrounding air. Several types of aerodynamic forces can be generated, such as drag and lift (or downward roll), as well as all other less relevant effects such as lateral forces, etc. [45].

The magnitude of these forces will be heavily dependent on the shape of the vehicle as well as in the material of the surface. As these factors can vary a lot, the exact modelling of the aerodynamic forces is no easy task. Because of this, aerodynamic forces are commonly computed using Computational Fluid Dynamics (CFD) simulations, or/and experimental testing using wind tunnels. Because of this, it is a vehicle dependent process, where a different test or simulation has to be done for each vehicle [45].

As making a simulation of this type would constitute a master thesis on its own, the complexity of the model will be reduced so we can have a simpler formula applicable to the vehicle and problem at hand. First we will only consider the drag force, which is the force that affects the vehicle energy consumption the most, since it acts in the opposite direction of the vehicle movement.

As the vehicle moves, it generates a higher pressure in the vehicle front and a lower air pressure in the rear. This pressure difference, allied with the viscous friction will generate the drag force, that opposes the movement of the vehicle. Luckily the drag force can be predicted using the semi-empirical formula known as drag equation, which can be seen in equation 2.4, where ρ is the *air density*, C_D is the *aerodynamic drag coefficient* and the A_f is the frontal area of the vehicle and v_{rel} is the relative velocity between the fluids [44, 45].

$$F_a = \frac{1}{2} \rho A_f C_D (v_{rel})^2 \tag{2.4}$$

The coefficient of drag is often a function of the Reynolds number(Re), but assumes a constant value for turbulent flow. Making a back of the envelope calculation for the vehicle we have the Reynolds number of approximately 10^6, for a velocity of $1m/s$, as can be seen in equation 2.5. This number is larger than 5×10^5, which means it can be argued that the flow is most of the time turbulent and the aerodynamic coefficient is constant. It is then possible to consider the drag force directly as given in equation 2.4 [46].

$$R_e = \frac{v d \rho}{\mu} = \frac{1 \times 1.4 \times 1.2}{1.8 \times 10^{-5}} \approx 10^6 \tag{2.5}$$

The model did not consider the effect of wind. This means that the relative velocity of the vehicle

and the air (v_{rel}) in equation 2.4 was the vehicle velocity measured in the GPS. This is a common approximation in the implementation of these types of models, due to the lack of availability of the wind values, and has been used in all the studies found. However, as the friction is proportional to the relative velocity squared, the increase in friction caused by the wind against the vehicle will not compensate its decrease when the wind is in the opposite direction.

Given all these approximations, aerodynamic friction is then given by equation 2.6, where v is simply the vehicle velocity.

$$F_a = \frac{1}{2}\rho \cdot A_f \cdot C_D \cdot v^2 \tag{2.6}$$

Rolling Friction

Another important factor that contributes to vehicle consumption is rolling friction. In general, rolling friction can be described as a friction force exerted on any round shaped body rolling over a surface. In the context of road vehicles, rolling friction arises from the tires rolling on the pavement.

In this particular case, several mechanisms cause the loss of energy in the tires. One of them is due to the deflection of the tire surface and threads. In other words, the losses that arise from the deformation of the tires near the contact point with the pavement. This deformation is caused by the weight of the vehicle as well as deformations during vehicle turning. Another mechanism contributing to this type of force is the energy loss due to friction between the tire surface and the pavement. This friction will depend on the type of pavement showing, for example, higher values in sand than in asphalt. Other types of energy loss mechanisms include tire slip, road bumps, among others that will not be mentioned for the sake of brevity. For a depper analysis of energy loss in energy friction, the reader is directed to[45].

All these factors are encompassed in the empirical formula 2.7, where the W is the vehicle weight, and c_r is the rolling coefficient. The formula implies that the larger the weight the more friction is applied. This is expected since the tire deformation increases with the weight of the vehicle. It is important to note that the rolling coefficient might not be constant, and depends on the tire temperature, as well as the type of pavement, vehicle velocity, and tire pressure. Examples of the values expected for the rolling coefficient as a function of the tire pressure and the pavement type consideres can be seen in figure 2.5 [44].

$$F_r = c_r \cdot W \tag{2.7}$$

Unlike aerodynamic friction, which becomes negligible as the velocity of the vehicle approaches zero, rolling friction is always present in the movement of the vehicle, and is even dominant for smaller velocities.

When the vehicle moves in a road of slope α, the weight in equation 2.7 corresponds to the normal force due to gravity. This is only true when lift forces are not relevant, which is the case for the majority of the vehicles [45]. The final form of the rolling friction is then given by equation 2.8, where α is the slope of the road [44].

$$F_r = c_r \cdot W = c_r \cdot m \cdot g \cdot \cos\alpha \tag{2.8}$$

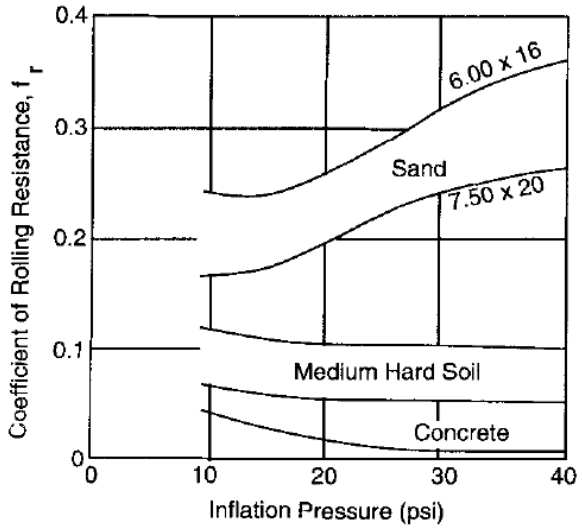

Figure 2.5: Rolling friction coefficients for different pavements as a function of the tire pressure [44].

The rolling coefficient also has a dependency on the vehicle velocity. This is due to increased flexing work and vibration in the tire body as the velocity increases. An empirical approximation for road vehicles in concrete pavement can be made for smaller velocity values. According to this approximation, the rolling friction coefficient depends on the velocty as shown in equation 2.9, where Q is a constant defined to be $44.4m/s$. This formula for the rolling coefficient has been used extensively in vehicle modelling [23, 25, 45, 47].

$$c_r \propto \left(1 + \frac{v}{Q}\right) \tag{2.9}$$

Assuming the general dependence as shown previously the final equation for the rolling friction is given by 2.10, where c_{r0} is the constant rolling coefficient. In the following sections, c_{r0} will be represented as c_r because the other dependencies were ignored.

$$F_r = c_{r0} \cdot m \cdot g \cdot \cos\alpha \cdot \left(1 + \frac{v}{Q}\right) \tag{2.10}$$

Gravitational Force

A major factor affecting the vehicle consumption is the gravity acting on the vehicle. When in irregular terrain, this is the main contributor to the vehicle energy spending. The gravitational force acting on a vehicle in a road of slope α is given by equation 2.11 [44, 45].

$$F_g = m \cdot g \cdot \sin\alpha \tag{2.11}$$

Lumped Mass Energy Prediction

From the previous formulation of the lumped mass model, in equation 2.3 we cannot yet find the energy spent by the vehicle, for a given trip. In order to do that, we have to integrate the traction force in equation 2.12 along the travelled path to find the work. This will be the energy provided by the motor

Name	Symbol	Expected Value
Drag Area	$C_d \cdot A$	$1.75m^2$ [11]
Rolling Coefficient	c_r	0.012 [11]
Vehicle Mass	v_m	829.4(sec. 3.1.4)

Table 2.1: Expected lumped mass model vehicle parameters for the **e-tuk Limo GT** vehicle.

to the vehicle during the trip and will also represent the variation of the energy in the batteries (ΔE), as shown in equation 2.13. Using the model for each of the forces found previously, the result is the integral that can be expressed as shown in equation 2.14.

$$F_t = m\frac{d}{dt}(v(t)) + F_a + F_r + F_g \tag{2.12}$$

$$\Delta E = \int_{s_i}^{s_f} F_t \cdot ds = \int_{s_i}^{s_f} \left(m\frac{d}{dt}(v(t)) + F_a + F_r + F_g \right) \cdot ds \tag{2.13}$$

$$\Delta E = \frac{1}{2} m \cdot (v_f^2 - v_i^2) + c_r \cdot m \cdot g \left(\Delta s_{xy} + \int_{s_{xy_i}}^{s_{xy_f}} v \cdot ds_{xy} \right) + m \cdot g \cdot \Delta h + \rho \cdot c_D \cdot A_f \cdot \int_{s_{xy_i}}^{s_{xy_f}} v^2 \cdot ds_{xy} \tag{2.14}$$

Using the traction force, it is also possible to estimate the instantaneous power provided by the motor. The power delivered will be equal to the work performed by the traction force, which is clear in equation 2.15.

$$P = F_t \cdot v \tag{2.15}$$

Typical Coefficients

The **lumped mass model** that has been described in the previous sections is dependent on the vehicle parameters. The parameters concerning the vehicle studied in this work are shown in table 2.1. Using these coefficients, the different forces acting on the vehicle were estimated using the expressions shown in 2.16.

$$\begin{cases} F_g = m \cdot g \cdot \cos\alpha \\ F_r = c_r \cdot m \cdot g \cdot \cos\alpha \cdot \left(1 + \frac{v}{Q}\right) \\ F_a = \frac{1}{2}\rho \cdot A_f \cdot C_D \cdot v^2 \end{cases} \tag{2.16}$$

Figure 2.6(a) shows the variation of rolling and aerodynamic friction forces as a function of the vehicle velocity. In the rolling friction calculation, road slope was assumed to be zero (i.e. $\alpha = 0$). The velocity range shown represents only velocities consistent with the ones measured in the vehicle. As the velocity values are relatively small, the rolling friction is expected to be the most important force in the vehicle motion. However, due to the its dependency on the square of the velocity, aerodynamic friction grows rapidly, reaching the same magnitude as the rolling friction for higher velocities.

Figure 2.6(b) shows the variation of the forces as a function of the road slope. For the estimation of the aerodynamic and rolling frictions, the maximum velocity of $12m/s$ was considered. It is apparent that, as the slope increases, the gravitational force becomes the dominant term over the friction forces. This means that gravity will be the most important force acting on the vehicle if the road slope is high.

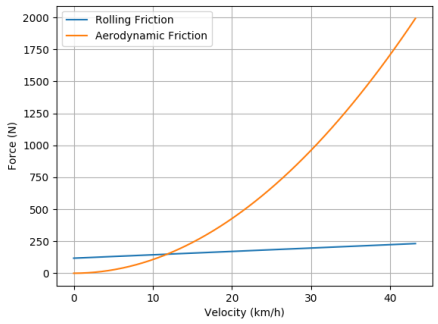

(a) Aerodynamic and rolling friction as a function of the velocity for slope $\alpha = 0$

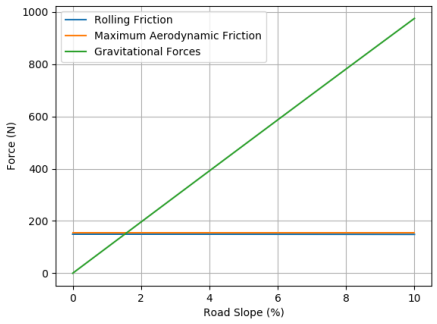

(b) Aerodynamic and rolling friction as a function of the road slope for velocity $v = 43km/h$

Figure 2.6: Comparison between the force magnitudes for the **e-tuk** parameters in table 2.1 as a function of the angle and the velocity.

2.2 Statistical Models

In addition to physical models, statistical models have also been used to estimate the energy consumption of road vehicles. These models do not require the knowledge concerning the physical mechanisms at play in the vehicle motion or any types of parameters which characterise it. In previous studies, models including neural networks[28, 29, 37], decision trees[29] and K-nearest neighbours[38] have been used. The way that these methods work is by using data to build a model that describes them well without any knowledge of the physics involved. Statistical models should improve as the data collected increases, allowing them to capture finer details of vehicle consumption behaviour.

In the present work, two different statistical models were used. The following sections are dedicated to a summary of the methods and outline of the algorithms.

2.2.1 Decision Trees Regression

Decision trees are commonly used in data science to solve both classification and regression problems. In this work, the decision tree method is used to solve the regression problem formulated in equation 2.1. Therefore the target variable to predict is the energy consumption and the features are characteristics of the trip segment, such as total distance, average velocity and acceleration.

In order to better understand how the decision tree algorithm works a simple example taken from the data collected is provided in figure 2.7, where Δh is the height variation from the trip start to finish, a is the average acceleration and ΔE is the total energy spent in the trip. As can be seen, the decision tree can be pictured as a graph where each of the nodes represents a binary decision based on the data features. In order to predict the energy consumption, successive tests are made to the data, starting at the root node and following the chart all the way through until a terminal node is reached.

However, two questions can be asked: how can the best tree configuration be found and what energy value is considered in the terminal nodes? The decision tree was grown using the measured data, with known energy consumption. To grow the decision tree there are three main algorithms that can be used:

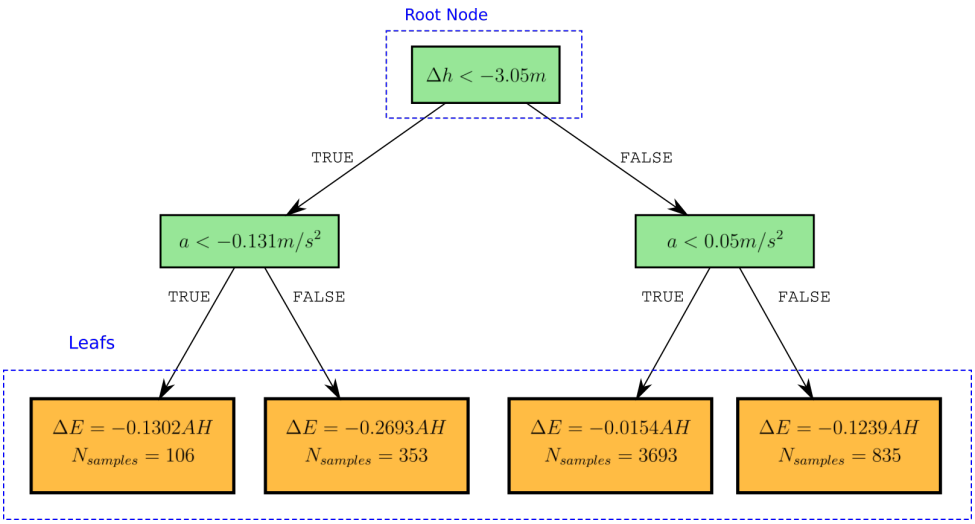

Figure 2.7: Example of a decision tree built using the **decision tree regression model** for 50s trip segments with max depth = 2.

the ID3, its more efficient brother C4.5 and the CART algorithms. In this work, it was used the *sklearn* python library to implement this model, which uses the CART algorithm as a basis. This algorithm was developed by Breiman et al. [48] and is characterised by the use of binary splits in the training data. The best split is found using the Gini index criteria[49].

The value considered in the terminal nodes is given by the average energy consumption measured for the data instances inside each of those nodes. In figure 2.7 the number of instance per leaf is shown as $N_{samples}$.

2.2.2 K-Nearest Neighbours Regression

The K-nearest neighbours algorithm is also a common statistical data-driven method used both in classification and regression. As done previously, this model is also used to solve the regression problem and to predict the energy consumption from the trip segment features.

The way this algorithm works is, when presented with a new data point, it will compute the distances between that point and the ones in the training data. The energy prediction will then be a weighted average of the energy measured in the K points that are closest from the new one. This is the reason for the name K-nearest neighbours. Figure 2.8 shows three examples of the algorithm working in a data set for several values of K.

The distance in between the point can be calculated using several metrics, such as the typical Euclidean (equation 2.17) or Manhattan (equation 2.18) distance metrics. Another possibility to improve the results of the model is considering weights on the average proportional to the inverse of the distance, considering the closer values more relevant than the ones farther away.

$$d_E = \sqrt{\left(\sum_{k=1}^{N}(x_k - y_k)^2\right)} \qquad (2.17)$$

$$d_M = \sum_{k=1}^{N}|x_k - y_k| \qquad (2.18)$$

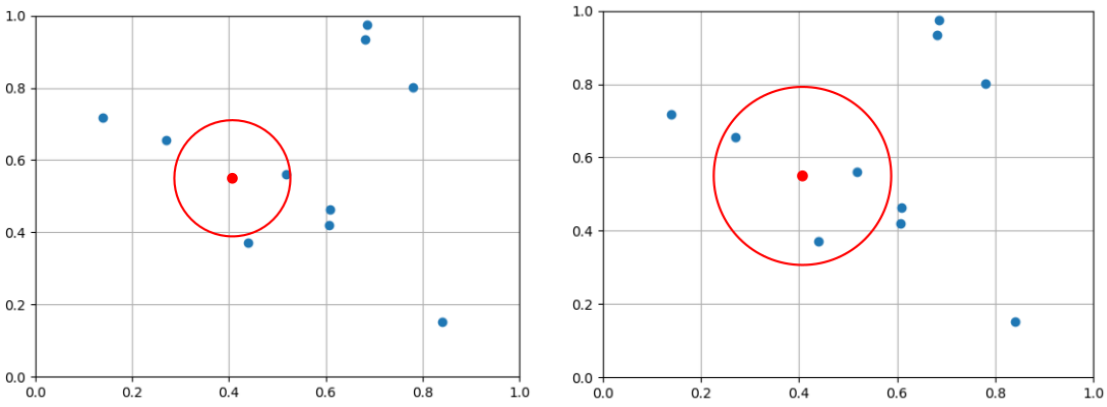

(a) $K = 1$ (b) $K = 3$

Figure 2.8: Example of how the KNN algorithm works. Points in the training set (blue) that are used in the weighted average prediction of the unknown point (red) are inside the circle for two different values of K.

Chapter 3

Data Collection

The main goal of this chapter is to explain the on-board setup used in the vehicles in order to collect the data used in both the trip-based models of chapter 5 and the history-based models of chapter 6. In addition to this, it is detailed the reasoning behind the design chosen and also the tests made.

This chapter starts by providing some context and details concerning the vehicles used and showing how some properties of the vehicles are estimated (section 3.1). The following section is focused on the **Data Acquisition System** and describes it from the software built to the hardware used. In this section are also provided the schematics and software structure used in the system. The final section is focused on the **battery setup** used in the main vehicle. In this section are provided the mechanical drawings of the battery compartment and detail how the batteries were connected with the BMS and between each other.

3.1 Vehicle Properties

In this work, two BEV were used. They differed a lot from one another not just in the type of vehicle but also in the battery capacity and the electric motor.

The first was an **e-max** electric scooter that is shown in figure 3.1(a). This first vehicle was used in the early stage, in order to test the data acquisition system that was then transferred to the second vehicle. The battery bank in the motorcycle consisted of 16 40Ah $LiFePO_4$ batteries with a nominal voltage of 51.2V. The vehicle motor is a 4kW brushless DC motor.

The second and main vehicle used in this work was an auto rickshaw. The vehicle studied in particular was a **LimoGT** model manufactured by *e-tuk Factory* and can be seen in figure 3.1(b). The battery bank of the *e-tuk* consisted of 24 160 Ah batteries, with a nominal voltage of 76.8V. The motor in this vehicle was a 7kW three phase AC motor.

As mentioned before, the motorcycle was only used for testing the data acquisition system, and for this reason, no major data acquisition on in-depth modelling was performed for this vehicle. However, because some detail about the *e-tuk* will be important for the implemented models in later sections of this work, a few general properties of the vehicle, such as the controller configuration, the motor

(a) **e-max**

(b) **e-tuk Limo GT**

Figure 3.1: Pictures of the vehicles used.

specifications and the gearbox ratio will be explained.

3.1.1 *e-tuk* General Properties

The overall properties of the original model of the main vehicle taken directly from the brochure provided by the manufacturer can be seen in table 3.1[50]. The values shown in this table relate to the original lead-acid battery pack, which was converted to a lithium-ion prior to the data acquisition. The details concerning this conversion will be provided in section 3.3. Because of this change, the vehicle mass with battery provided in table 3.1 is not applicable and a new mass estimation was made for the new battery pack in section 3.1.4.

The vehicle has a maximum speed of 50km/h, which makes it a powered light vehicle, classified by Portuguese standards as a L5 vehicle. The original model of the vehicle has a expected range of 80km as provided by the manufacturer. However, the vehicle autonomy has changed with the change of the battery pack. It is possible to find the new expected autonomy by estimating the average consumption of the vehicle. This was done by computing the distance that the vehicle travels during each day (Δs) as well as the correspondent the variation of the state of charge of the battery (ΔE). The measured points can be seen in figure 3.2. A regression to equation 3.1 was done to estimate the average consumption of $A = 1.85 \pm 0.05$ Ah/km, with a R^2 value of 0.97. This model was then used to find that the distance that is expected to be travelled for a complete battery discharge of 180Ah is around 97km.

$$\Delta E = A \cdot \Delta s \tag{3.1}$$

With the lithium-ion battery pack, the vehicle range increased. This was to be expected since the batteries are significantly lighter.

The data concerning the motor can be seen in table 3.2. It is shown that the motor is a three-phase 7kW induction motor with maximum rotational frequency of 3100RPM.

Name	Value
Tire Size	155/80R13
Front Tire Size	145/70R12
Charger Specification	10 A
Battery Voltage	72 V
Weight (w/o battery)	695 kg
Weight (w/ battery)	1030 kg
Maximum Velocity	30-50 km/h
Autonomy	80 km

Table 3.1: Vehicle data for the **e-tuk Limo GT** taken from the original brochure. The values shown are valid for the original lead-acid battery pack, and some changes are expected for the new battery pack[50].

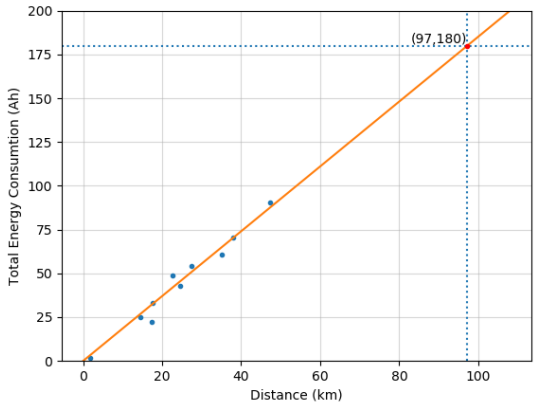

Figure 3.2: Energy consumption versus distance travelled for all the days of data acquired. The linear model obtained had ($A = 1.85 \pm 0.05$ Ah/km), $R^2 = 0.97$

3.1.2 Gear Ratio

No information concerning the gearbox was provided by the manufacturer However, the gear ratio can be estimated. In this work two estimation methods were used. The first consisted on counting the number of turns in the drive shaft in relation to the number of turns in the wheels. This test was done with only one spinning wheel. There were obtained 25.5 turns in the driving shaft for 5 turns in the wheel. The gear ratio is given by equation 3.2, where ω_{drive} is the rotational frequency of the drive shaft and ω_{in} is the average wheel rotational frequency and ω_{w1} and ω_{w2} are the rotational frequencies of the wheels. As only one wheel was spun, ω_{w2} is zero.

$$R = \frac{\omega_{drive}}{\omega_{in}} = \frac{\omega_{drive}}{\frac{\omega_{w1}+\omega_{w2}}{2}} = \frac{25.5 \times 2}{5} = 10.2, \tag{3.2}$$

The other way to estimate the gear ratio considers that the maximum velocity measured in the vehicle corresponds to the maximum rotational velocity of the motor. Using this assumption, it is possible to estimate the gear ratio, which will be a relationship between the number of motor rotations and the number of wheel rotations. The ratio is then given by equation 3.3, where D_t is the tire diameter, the RPM_{max} is the maximum number of rotations in the motor and v_{max} is the maximum vehicle velocity measured.

Name	Value
Rated Power	7KW
Phases	3
Rotational Velocity	3100 RPM
Frequency	104.5 Hz
Current	152 A

Table 3.2: **e-tuk Limo GT** motor characteristics.

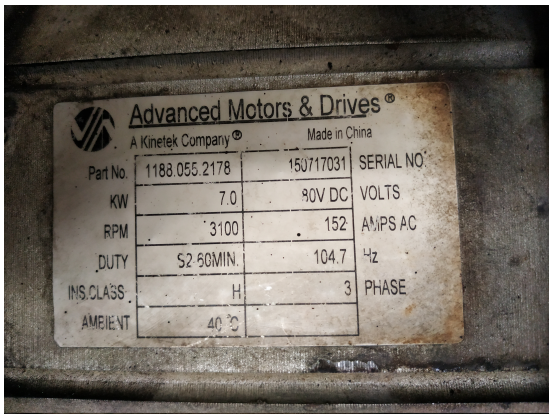

Figure 3.3: Original **e-tuk Limo GT** plate on the motor.

$$R = \frac{\frac{RPM_{max}}{60}}{\frac{v_{max}}{\pi \cdot D_t}} = \frac{\frac{3100}{60}}{\frac{12}{\pi \cdot D_t}} = \frac{\frac{3100}{60}}{\frac{12}{\pi \cdot 0.579}} = 7.8 \tag{3.3}$$

The first method was chosen to be the most reliable because it is a direct measurement of the gear ratio, in stead of an estimation from other values. Because of this, in the following sections the gear ratio was assumed to be 10:1.

3.1.3 Controller Configuration

The controller of the motor is a *Curtis 1234*. The main configuration concerning the battery pack can be seen in table A.4. The configuration of the under and over-voltage was made by testing the vehicle while climbing and descending hill. The full controller configuration can be seen in appendix A. The controller offers three different control options, two options using velocity control and one using torque control. For this application it was chosen the velocity control mode for the vehicle because it was what was already in place previously.

Name	Value
Nominal Voltage	78.5 V
User Overvoltage	115 %
User Undervoltage	80 %

Table 3.3: Battery Menu controller parameters

3.1.4 Mass Estimation

The vehicle factory model is the **Limo GT** with specifications provided by the manufacturer as can be seen in [50], and in the table 3.1. As the vehicle originally had lead-acid batteries, the weight has to be changed to accommodate the lithium batteries that were introduced. The batteries that were put into the vehicle were $LiFePO_4$ lithium ion batteries weighing 5.6kg each. As 24 of these were used, the resultant final mass of the vehicle was of around 830kg without payload.

$$m_v = 1030 - 335 + 24 \times 5.6 = 829.4kg \tag{3.4}$$

3.2 Data Acquisition System

All the models implemented in this thesis require data to be acquired from the vehicle. Therefore, a data acquisition system was developed. In fact, two similar systems were developed: one used only during testing in the **e-max** motorcycle and the other in the *e-tuk*. The main difference is that in testing a measurement of the Hall sensor was included, unlike what was not done in the main system.

In the following sections, it is described how such a system was built and detailed the procedure used to decode the BMS messages (section 3.2.1), described the set-up used to measure the **Hall sensor** in testing (3.2.2), the software used in the acquisition (section 3.2.4), the **schematics** of the system used (section 3.2.3) and lastly the implementation of the webpage used to access the acquisition (section 3.2.5).

3.2.1 BMS reverse-engineering

The data concerning the vehicle batteries was collected from the Battery Management System (BMS) on the battery pack of the vehicle. The same brand of BMS was used in both vehicles. This means that, despite having different specifications, i.e. different number of cells and different maximum current, they were the same from the data acquisition standpoint.

The BMS used in the main vehicle is rated for 300 A of current and has capability of handling 24 cells. It can also be configured to handle the $LiFePO_4$ batteries used. As can be seen in figure 3.4, the BMS came with an auxiliary screen device to display varied information concerning the battery pack. The BMS was also capable of communicating with a mobile phone via bluetooth using a mobile application providing the real time measurements of the BMS shown in figure 3.4. Through the application it is also possible to reprogram the BMS to the parameters of the battery pack used.

The main BMS board exchanged information with the auxiliary screen using serial communication. The serial communication contains all the necessary information concerning the battery pack, such as its voltage, current and power consumption. In order to have access to this information, it is necessary to mimic the screen behaviour in order to interact with the main BMS board using our system. To do this, a *Raspberry Pi* device was used.

The first realisation was that in order to obtain the data, the screen sent a request message to the BMS board. To know what this message was, the characteristics of the serial communication were needed. In order to know this, an oscilloscope was used to measure the time duration of the smallest pulse on the message (T_s). The baud-rate was estimated using equation 3.5 and found to be 19200. The rest of the parameters of the serial communication were assumed to be the most common ones (see table 3.4), and they were proven to be the right choice.

Figure 3.4: Photo of a similar BMS to the one used in the vehicle.

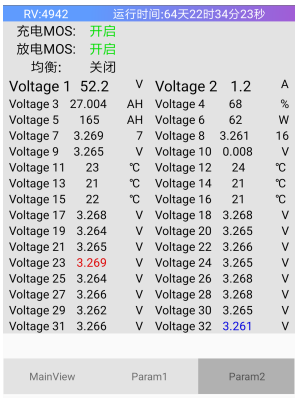

Figure 3.5: Screen-shot of the Mobile application measurements. It should be noted that the labels in the mobile application were not correct. In appendix B it is shown the correct correspondence of labels.

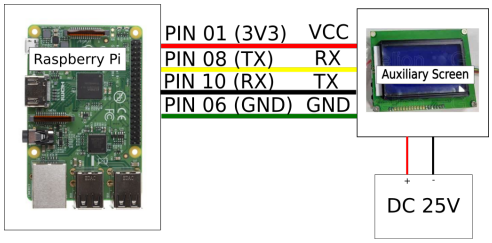

Figure 3.6: Wiring diagram for the test of the request message sent from the screen.

$$f_s = \frac{1}{T_s} \tag{3.5}$$

The message sent by the screen was then extracted by connecting the serial bus of the *Raspberry Pi* and of the BMS board as shown in figure 3.6. The message was found to be *0x5a5a00000101*, here presented in hexadecimal representation.

Parameter	Value
Baud-rate	19200
Parity	None
Stop Bits	1 bit
Byte size	8 bits

Table 3.4: BMS serial communication parameters

By sending this request message to the BMS board it was now possible to receive the battery pack information from the BMS board. However, the manufacturer did not provide any information concerning the communication protocol used in the serial communication. In other words, it was unknown which set of bytes in the incoming message corresponded to which of the physical parameters. This correspondence is fundamental for the logging of the variables.

In order to find this correspondence, the time evolution of the message was saved using the *Raspberry Pi* connected to the BMS of the testing vehicle as shown in figure 3.7. By systematically converting

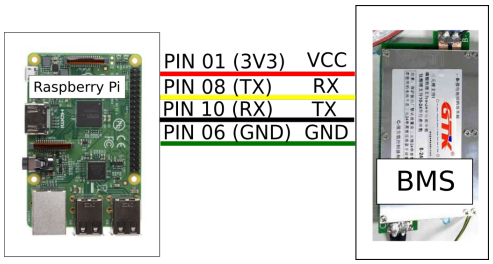

Figure 3.7: Schematic of the connection to the BMS for testing.

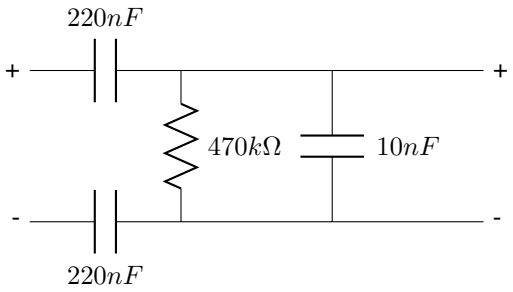

Figure 3.8: Hall Sensor circuit

sets of one, two and four bytes with different offsets and plotting their outcome over time, it was possible to find some locations of the features in the message. In addition to this, the actual decimal value was compared with the ones shown in the mobile application connected to the BMS. Using this method, it was possible to track down the main features such as the battery current, the battery voltage and the individual cell voltages. Finally, the APK of the mobile application was decompiled and in the coding of the bluetooth connection the byte positions of the individual parameters were found. Fortunately, the Bluetooth connection used the same communication protocol as the serial communication and the byte positions of the physical quantities could be found. All the variables collected as well as the byte positions can be seen in appendix B.

3.2.2 Hall Sensor Set-up

As mentioned before, in the testing vehicle it was implemented the measurement of one of the Hall sensors of the motor. This allowed to collect data about the rotational velocity of the motor instead of this information having to be extracted from the vehicle velocity measured using the GPS.

The circuit used to measure the signal from the Hall sensor can be seen in figure 3.8. The two capacitors in series are used for galvanic isolation and the capacitor in parallel is used to act as a low-pass filter to stabilise the signal. Figure 3.9 shows the waveform of the signal obtained, for low and high motor velocities.

In order to extract the motor velocity, the number of poles of the motor must be known. This was done by testing one full turn of the wheel of the motorcycle and counting the signal inversions in the Hall sensor. In figure 3.10 the output of the test for the motor poles can be observed. It was found that the brushless DC motor of the motorcycle contained 20 poles. The measurement of the velocity was made using the measurement of the time between two consecutive pulses using the *pigpio* python

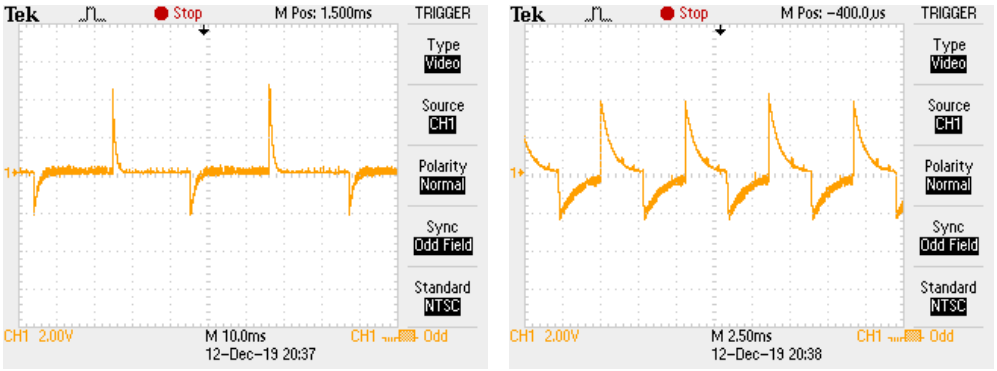

(a) Low Velocity (b) High Velocity

Figure 3.9: Waveform of the Hall signal after the circuit 3.8

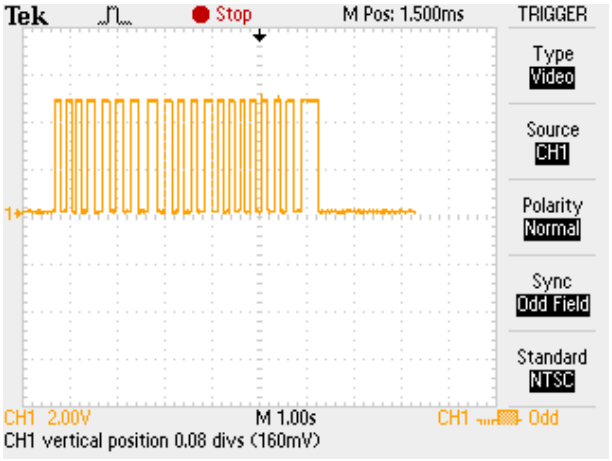

Figure 3.10: Oscilloscope output for the test of the number of poles of the motor.

package. This package allows the almost delay free interaction between python and the IO ports of the Rapsberry Pi, and was used to measure the time between two rising edges of the signal (T_{meas}). The motor frequency is then given by equation 3.6.

$$\omega = \frac{2 \cdot \pi}{T_{meas} \cdot \frac{N_{poles}}{2}} \tag{3.6}$$

3.2.3 Experimental Set-up

Up to this point, it has only been discussed the connection between the *Raspberry Pi* and the BMS. The purpose of this section is to discuss each part of the data acquisition system, as well as how the system was implemented in both the test and main vehicles.

At the centre of the whole set-up is the *Raspberry Pi*. This device is a small computer, where every piece of hardware is condensed into a small 56×85 mm board. It combines the complexity of a computer while still interacting with low level electronics. The size, affordability and versatility of these devices make them good candidates for developing *Internet of Things* and other intelligent devices as a whole. In this particular work, the *Raspberry Pi* is used to collect and save information from the BMS,

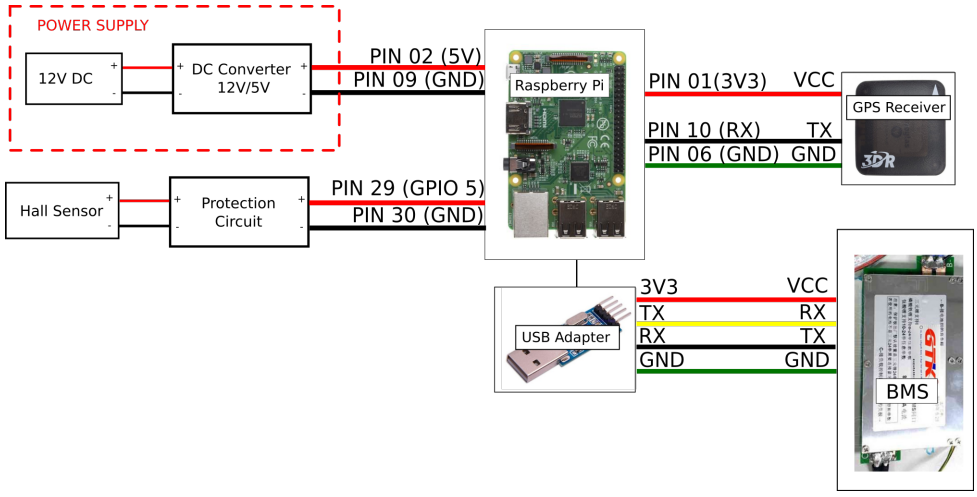

Figure 3.11: Schematic of the wiring used for testing the data acquisition system

the GPS receiver and the Hall sensor (only in testing).

The connection to both the BMS and the GPS receiver is made trough asynchronous serial communication. Because of this, two serial connections are required: one per device. As the *Raspberry Pi* only has one UART, a USB adapter was added in order to make up for this lack. The BMS was then connected to the USB adapter and the GPS receiver was connected to the UART pins of the *Raspberry Pi*. This was done in both the testing and the main vehicle (schematics of which can be found in figures 3.11 and 3.12, respectively).

Figure 3.11 shows the data acquisition system wiring used for testing and in figure 3.12 it can be seen the one used in the main set-up. The set-up used in the testing vehicle had several differences from the one used in the main vehicle. The main one is that the acquisition of the Hall sensor was only implemented in the test set-up. Another difference is that the screen was not used in testing, while it was in the main vehicle. For the second case the main difference is that there is no need to send the message from the *Raspberry Pi* to the BMS board because this is already done by the screen. It is only needed to read the serial connection to intercept the message coming from the BMS, removing the need to connect the TX *raspberry* pin to the RX BMS pin.

A smaller difference is that, while in the testing set-up the components were grouped in the space under the motorcycle seat, was not done in the main set-up. In the main vehicle, the display needed to be visible to the driver, so it is required for it to be in the frontal part of the vehicle. In addition to this, in order to read the GPS signal, the GPS receiver could not be in the battery compartment because it was covered with a metal sheet which would difficult the signal collection. Finally, the 12V supply also came from the frontal part of the vehicle. All the other components were inside the battery compartment as described in section 3.3.

3.2.4 Data Acquisition Software

As seen before, there are three types of data that are acquired and saved into a file. The first is the serial communication of the BMS, containing data concerning the battery pack, such as the consumptions and

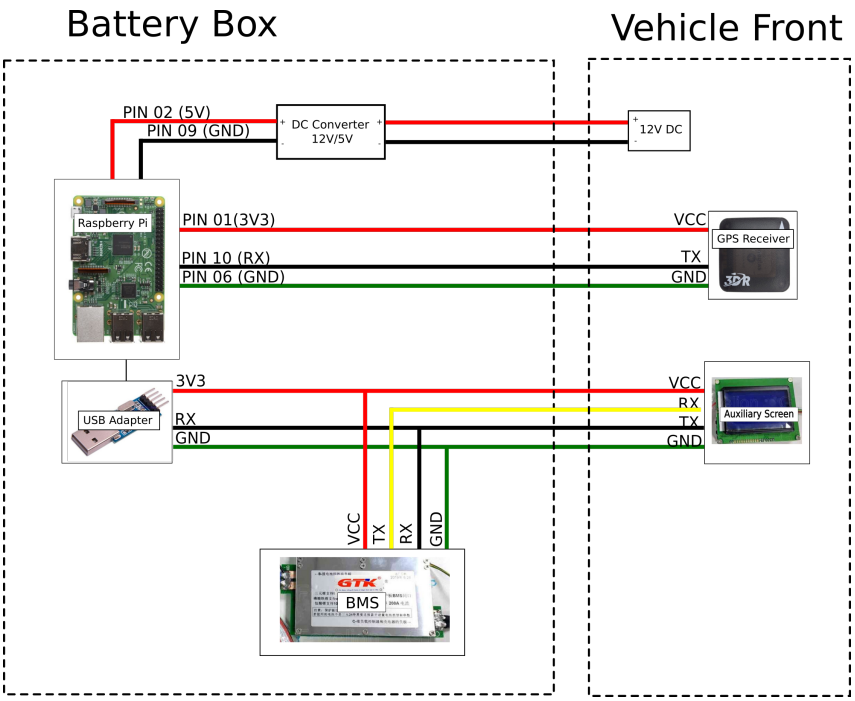

Figure 3.12: Schematic of the wiring in the main set-up used.

battery voltage and current, but also State of Charge (SOC). The second is the GPS data, which will provide information concerning the position of the vehicle and its velocity over time. And the final is the rotational frequency of the motor coming from the hall sensor. For this data to be saved, software was built to make the acquisitions.

The software was built inside the paradigm of **Object Oriented Programming** using *Python 3*. Figure 3.13 presents the inheritance scheme of the classes implemented, where the arrow points from one class to the one it inherits from. In this context, inheritance means basically that when a class inherits from another it will have the same methods as the one it inherits from as well possibly adding some additional ones. This paradigm was chosen in order to keep the three data acquisition processes independent from one another and, as is explained in the next paragraph, running in separate processor *threads*.

As shown, a general class named *SensorThread* was built to act as a blueprint for the following classes. In it, general functions to **return** the last data and to **update** the measurement are defined. This class inherits from the class *Thread*, which is part of the **threading** python package and allows the program to run a function in an independent CPU thread. Three different classes inherit from *SensorThread* and acquire data from the three different sources.

The class **TXThread** was built to send the message found in the previous sections to the BMS board and to read and save its response. This message contained the battery information that was discussed previously.

The **GPSThread** made the acquisition of the data received periodically from the GPS and saved its contents. To make the GPS readings, it was used the GPS python package. This package reads the information coming from a daemon **GPSD** process. This process reads constantly the information

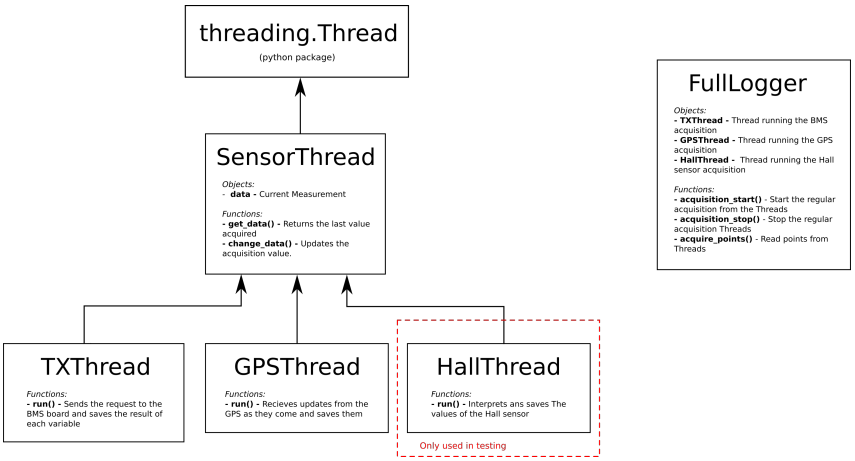

Figure 3.13: Inheritance Scheme of the python classes implemented. The arrow is pointing from the class to the class it inherits from. The **FullLogger** class contains one class of each of others, while not inheriting from them.

coming from the GPS receiver and is initiated at the *Raspberry Pi* startup[51]. The GPS updates were received every second.

The **HallThread** interpreted the signal from the Hall sensor of the motor. This was only used in the testing vehicle because there was no access to the hall sensors of the main one. This provides an auxiliary measurement of the rotation of the motor providing more accurate data than the coming from the GPS.

Figure 3.13 shows an extra class, which is the **FullLogger**. This class is responsible for the regular acquisition of the data in the different threads and saving the data in a file. It has one of each custom Thread classes and extracts the values in a constant time interval using the Multitimer package.

3.2.5 Server Page

One problem with the system was that there was no way of visualising the current state of the vehicle without having to connect to the *Raspberry Pi*, for example, via SSH. In order to avoid having to connect a computer every time to check if the acquisition is correct, the *Raspberry Pi* was converted into a server hosting a webpage. As can be seen in figure 3.14, the page contained the information about the last point recorded, similarly to the BMS application but now containing also the GPS information.

The server was built using python with the **django** package. The data in the table is updated in the refresh http request. One advantage of using the webpage instead of an application is that it can be visualised using any device connected to the raspberry wifi hotspot. With access to internet connection, the implementation of this webpage alone would allow the access to the vehicle information remotely, allowing a more immediate access to the information from anywhere.

3.2.6 Testing Results

Figure 3.15 displays the time evolution of the testing acquisitions made inside Intituto Superior Tecnico. It can be seen that the GPS position has some error on the position, because the acquisition points do

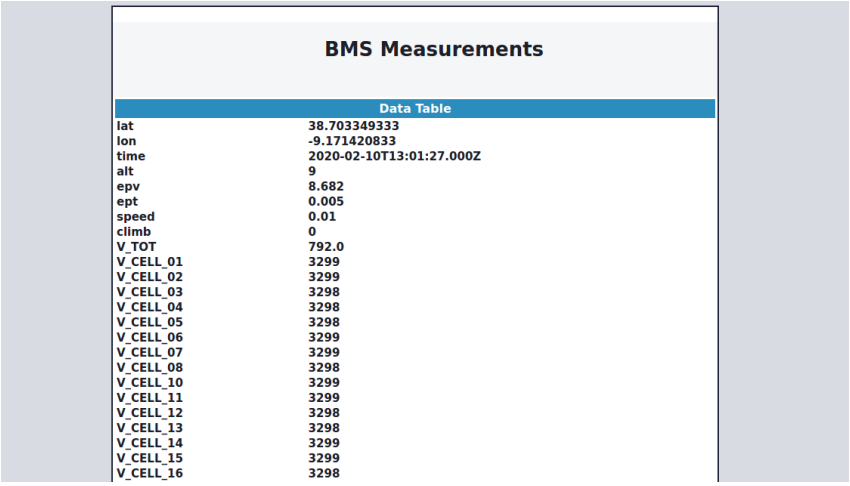

Figure 3.14: Screenshot of the webpage hosted in the *Raspberry Pi*

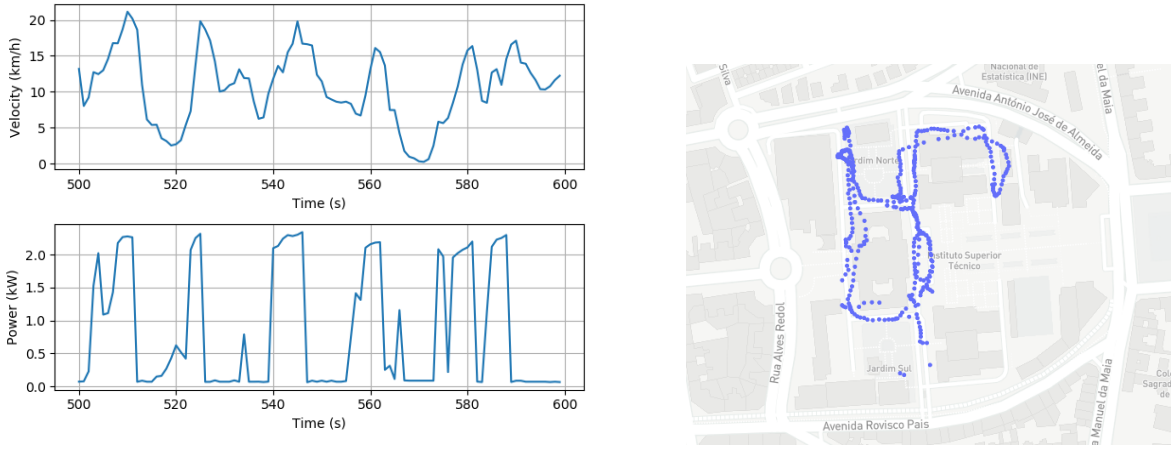

(a) Segment of the power and velocity values measured.

(b) Vehicle positions measured.

Figure 3.15: Example of data collected in thhe **e-max** motorcycle during the tests.

not coincide perfectly with the road maps. This can also be due to a lack of GPS signal from inside the motorcycle seat.

The velocity values in figure 3.15(a) of the vehicle are inside what would be expected given that the maximum velocity of the motorcycle was 45km/h. This also applies to the consumption values, for a 4kW motor.

Consumption Curve Estimation

Testing the vehicle in segments of constant velocity it was possible to extract the consumption curve of the motorcycle. The tests were done in a straight road segment with very low road slope, in Lisbon near the river. To find the consumption curve of the motorcycle the road was travelled in both directions keeping a constant speed measured in the motorcycle speedometer. The velocity values ran from 5 to 40 km/h in increments of 5km/h. Each consumption point is the average of the power consumption inside the constant velocity interval.

The consumption points acquired can be seen in figure 3.16 in blue. It is shown that there are two

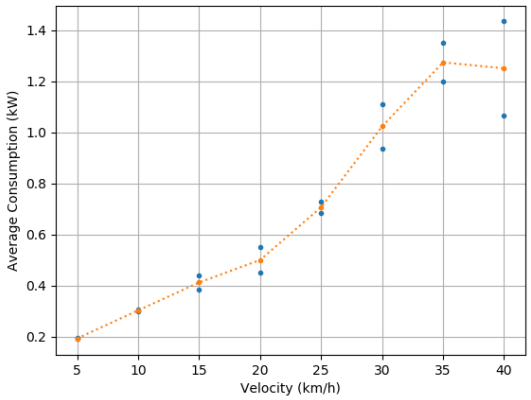

Figure 3.16: Measured consumption for the **e-max** as a function of the vehicle velocity.

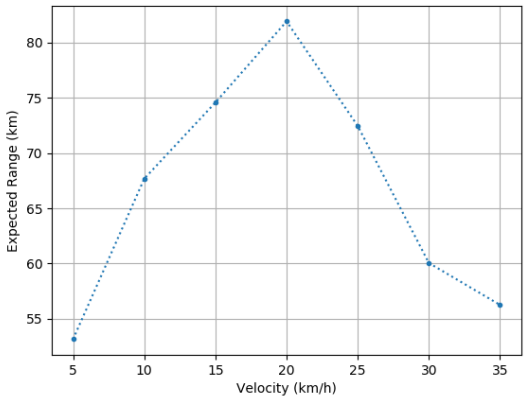

Figure 3.17: Expected Range for the **e-max** motorcycle as a function of the velocity.

points for each velocity, which correspond to the two road directions. One of the values is greater than the other because of the differences in wind direction that caused bigger consumption in one way than in the opposite. The consumption estimation in orange is the average of both points.

The expected remaining driving range of the vehicle is estimated using equation 3.7, where $\bar{p}$ is the average consumption estimated and E_{bat} is the total energy capacity of the batteries. The expected range curve can be seen in figure 3.17. It is also clear that there is an optimal velocity of 20km/h, at which the largest range is achieved.

$$RDR = \frac{E_{bat}}{\bar{p}} \tag{3.7}$$

3.3 Battery Setup

One of the goals of this work was to convert the battery pack of the **e-tuk** from lead-acid batteries into more modern $LiFePO_4$ lithium-ion batteries. The new batteries differ a lot from the ones installed previously, both in their electrical properties as well as in its dimensions. Because of this, a new battery compartment was designed to hold them as well as new battery connectors.

In the following sections, it is first made an overview of the differences between the original and the new batteries (section 3.3.1), it is then shown the battery configuration that was chosen as well as the schematics of the Battery and BMS connections (section 3.3.2), and finally several mechanical drawings of the different parts used can be seen (section 3.3.3).

3.3.1 Batteries

The original battery pack of the **e-tuk** consisted of 12 *Trojan T-105 lead acid* 6V batteries[52]. The capacity of this batteries as provided by their data sheet ranged from 185 to 220 Ah depending of the environmental conditions as well and discharge current. The new battery pack consisted of 24 $LiFePO_4$

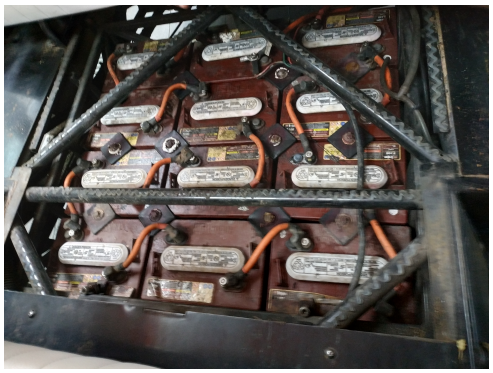

(a) Previous Pack

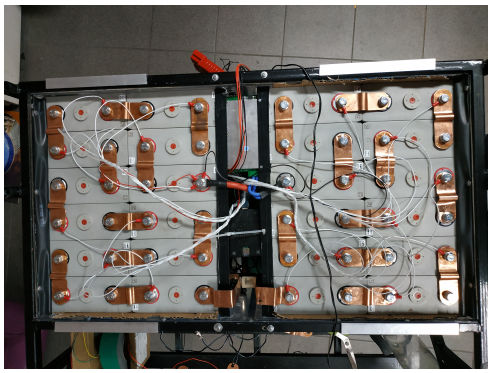

(b) Current Pack

Figure 3.18: Pictures of the two battery packs used in the **e-tuk Limo GT**.

CALB battery cells, with 180Ah capacity[53].

The lead acid batteries are cheaper than the lithium-ion. However, the lithium ion batteries make up for a more reliable and lighter battery pack than the previous one, causing an expected increase in the range of the vehicle due to the reduced rolling friction. While the lead acid batteries are expected to last 600 cycles, which make up for less than two years, assuming one cycle per day is done, the *lithium-ion* batteries are expected to last 2000 cycles, which is around 6 years with the same use. This represents a very high gain in durability of the batteries[54].

Parameter	**Lead-acid**	$LiFePO_4$
Nominal Voltage	72 V	76.8 V
Capacity	180-220 AH [52]	180 AH[53]
Mass	336kg [52]	135 Kg[53]
Expected Cycles	600 [54]	2000 [53]

Table 3.5: Comparison between the **lead-acid** and the **lithium-ion** battery packs used in the **e-tuk Limo GT**.

The $LiFePO_4$ batteries have been shown to be more thermally and chemically stable[55]. Despite having a lower specific energy, having only a voltage of 3.2V they are safer than the standard $LiNiMnCoO_2$ batteries. The batteries used are covered in a flame retardant compound that minimizes the consequences of a possible fire, which is a common problem in lithium-ion batteries.

3.3.2 Compartment Wiring

The connections in between the batteries as well as the batteries and the BMS can be seen in figure 3.19. The 24 cells were connected in series making up a nominal voltage of 76.8V. The connections between the batteries were designed so that the two battery pack connections were placed in the middle of the pack and could easily be connected to the BMS. It is also shown in figure 3.19 that a 200 A fuse was added in the middle of the battery pack in order to add a safety to the vehicle and avoid over-current.

Figure 3.20 shows that the BMS is connected to the positive poles of each of the battery cells. This is the standard wiring of the BMS and allows it to keep the balance between the cells and to provide information about the voltage of each of the them.

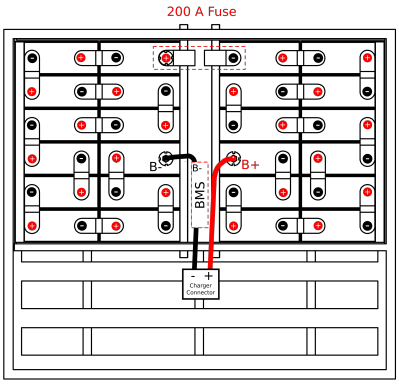

Figure 3.19: Wiring diagram inside the $LiFePO_4$ battery compartment

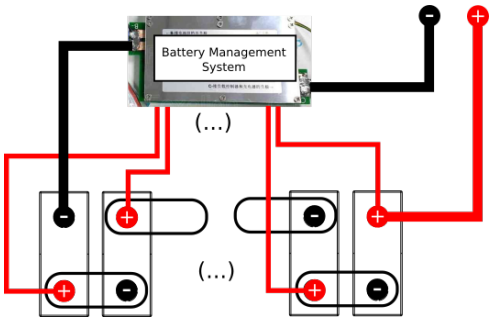

Figure 3.20: BMS wiring scheme in the $LiFePO_4$ battery pack.

3.3.3 Mechanical Design

To make the new battery compartment several mechanical drawings were made using **SOLIDWORKS**. In this section we show some of the drawings done and provided some information about them. In appendix C all the detailed drawings with added measurements can be seen.

Battery Compartment

The first modelled component was the battery compartment. This compartment was adapted from the original, which simplified mounting the device on the vehicle. The final result can be seen in figure 3.21. As the lithium batteries were smaller, a division was added to the original in order to hold the now new batteries in place. In addition to this the bottom of the compartment was covered with a metal plate to provide more support to the pack.

The battery compartment was covered, in all four sides and top in acrylic plates in order to protect the battery. The batteries were also glued to the bottom with foam tape, so that they could be held in place without significant vibration.

Connectors

While the manufacturer of the batteries also provided connectors, these had only one size. However in the chosen configuration (figure 3.19) two different sizes of connectors are needed: one larger for the

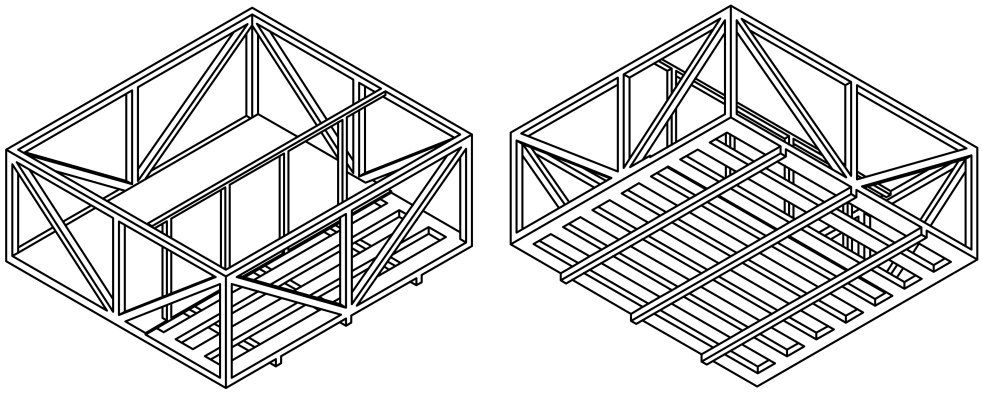

(a) (b)

Figure 3.21: Isometric Views of the battery compartment.

horizontal connections of the batteries and one smaller for the vertical connections ones. Figure 3.22 displays the model chosen for both of the connections. Appendix C contains the particular measurements used in each of the connectors.

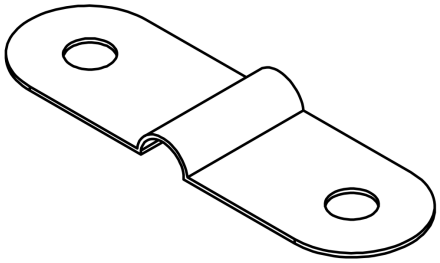

Figure 3.22: Isometric Views of the battery compartment.

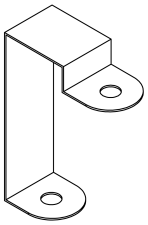

Figure 3.23: Isometric view of the fuse connector

Figure 3.19 shows that a 200A fuse was added for safety. To make the connection with the intermediate fuse with the batteries, two specific connectors were designed. The design used can be seen in figure 3.22. The top of the connector is liked to the battery while the bottom part is liked to the fuse. Once again, detailed measurements are provided in appendix C.

To link the batteries to the connectors, M14 **hex bolt screws** were used in combination with conic contact washers to hold the batteries to the connectors.

Bars

Four bars were used to hold the batteries in place. Two T-shaped bars to hold the middle of the batteries and two L-shaped bars to hold the left and right sides of the batteries.

Full View

Figures 3.24 and 3.25 present, respectively the exploded and assembled views of the final battery compartment.

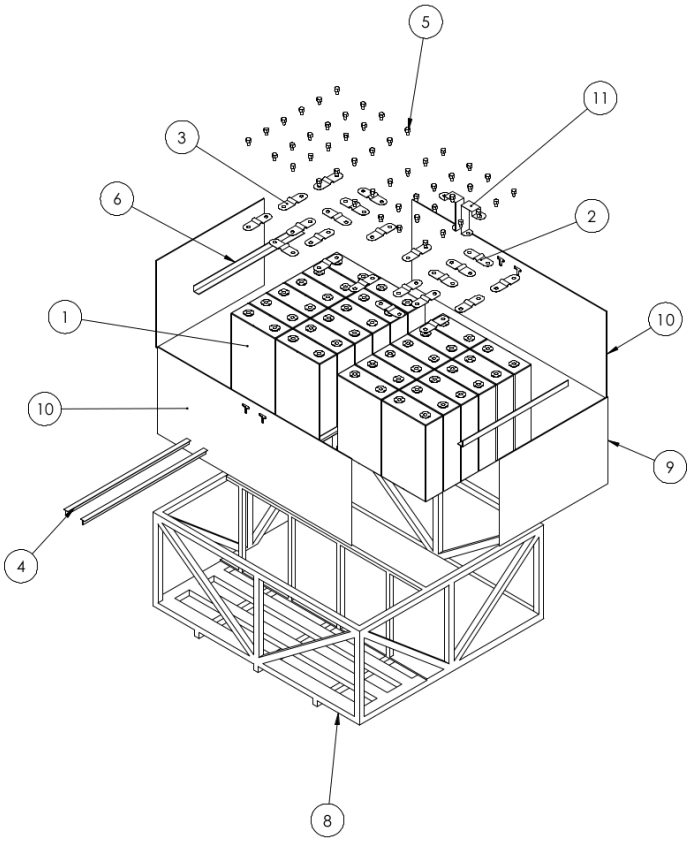

ITEM NO.	PART NAME	QTY.
1	CALB Battery	24
2	Horizontal Connector	8
3	Vertical Connector	14
4	T-shaped Bar	2
5	Battery Screws	48
6	L-shaped Bar	2
8	Battery Compartment	1
9	Frontal Plate	2
10	Lateral Plate	2
11	Fuse Connector	2

Figure 3.24: Exploded view of the battery compartment assembly.

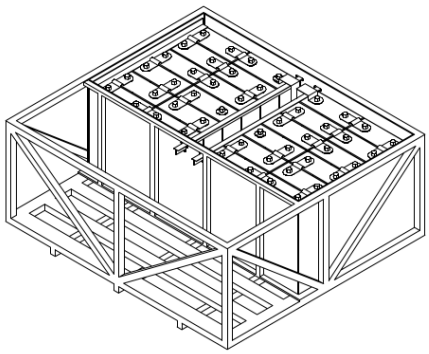

Figure 3.25: Isometric view of the assembled battery compartment.

Chapter 4

Preliminary Analysis of the Data Collected

The first objective of this chapter is to perform a preliminary analysis of the data collected during the vehicle motion, with the objective of ascertaining its main characteristics. This is done without making any data transformation, other than the removal of empty data points. The main purpose of this kind of analysis to detect possible errors or unexpected biases that the data may have, and to prepare it to be used in modelling. This is done in the first two sections, where it is first presented and analysed the distribution histograms of the data, in section 4.1.1. Afterwards, in section 4.1.2, the distribution of the features according to their spatial coordinates is shown .

The second purpose of this chapter is to explore the features that were derived from the data, but not directly measured. These features include, for example, the road slope and the distance travelled. The derived features shown in section 4.2.1 are real-time features that characterize each individual data points, e.g., the altitude. On the other hand, the features in section 4.2.2 characterize trip segments, and represent aggregated data such as the distance travelled and the velocity integrals. These features are important in the modelling sections.

4.1 Measured Features

The data analysed in the following sections and the in the rest of this work was collected from **06/02/2020** to **16/02/2020**. The data contains **485.5 km** of vehicle movement which corresponds to around 60 hours of vehicle usage. In table 4.1 there can be seen some general properties of this data, as well as the average values for some key features.

This is a fairly limited dataset for some of the models used, and it represents only a small part of the operation conditions of the vehicle. The initial plan was to acquire much more data. In stead of a week, it was intended to collect data concerning at least a month of vehicle operation. However, as the COVID-19 pandemic broke out and the company stopped making tours, the acquisition of new data was no longer possible. Therefore, it is worth noting that some of the performance of the models here

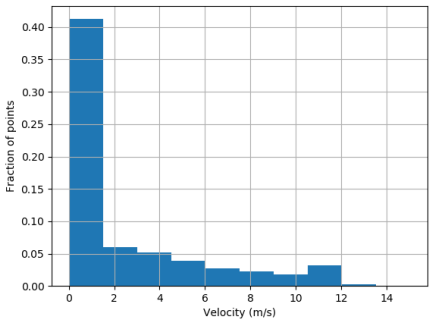

(a) Distribution of the velocity points without filtering.

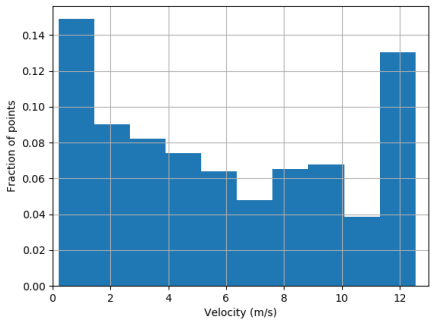

(b) Distribution of the velocity values for the points with velocity above 0.2m/s

Figure 4.1: Distribution of the measurement of the vehicle velocity for the data collected in the vehicle.

presented have been affected by the consequential lack of sufficient data.

Dates of collection	06/02/2020 - 06/02/2020
Total Distance	485 km
Total Time	60 h
Acquisition Frequency	3Hz
Average Velocity	2.26 m/s
Average Battery Current	12.5 A
Average Battery Voltage	88.2 V
Average Battery Power	958.7 W

Table 4.1: Summary of the key features of the data collected.

4.1.1 Feature Distributions

In this section, the individual distributions of four main data features used in the future models will be analysed. Namely, the vehicle velocity, the battery current, voltage and power. The information concerning the vehicle coordinates and altitude will be discussed in further sections.

As said before, this first analysis considers the data as collected without making any preprocessing other than the removal of empty data points, where the GPS connection was lost or the Raspberry failed to read the data from the BMS.

Figure 4.1(a) shows the distribution of velocity values. The most striking feature of this distribution is the existence of a major amount of points with very low velocity. This indicates that the acquisition contains a considerable amount of points where the vehicle is at rest, or very close to it. This can explain why the average velocity shown in table 4.1 has such a low value. Because of this, the points with low velocity were filtered out of the histograms. The resulting distribution can be seen in figure 4.1(b). The upper velocity limit that was chosen was of 0.2m/s.

Looking at this detail, it is possible to observe that as the velocity increases there are less points, but a well defined peak can be seen around the vehicle's maximum measured velocity 12m/s, which corresponds to 43km/h. One possible explanation for this is that, when the road conditions make it possible to go at higher speeds, the driver prefers to go at the maximum speed available.

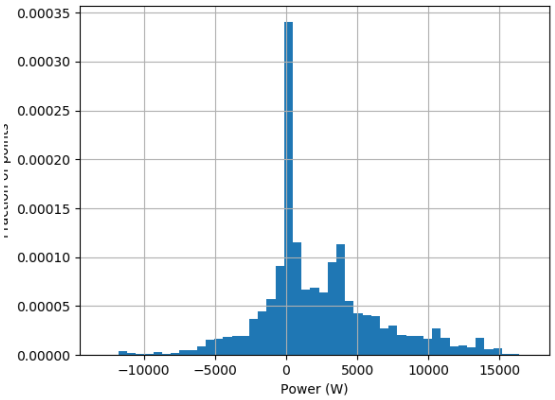

Figure 4.2: Power distribution of the measured data points.

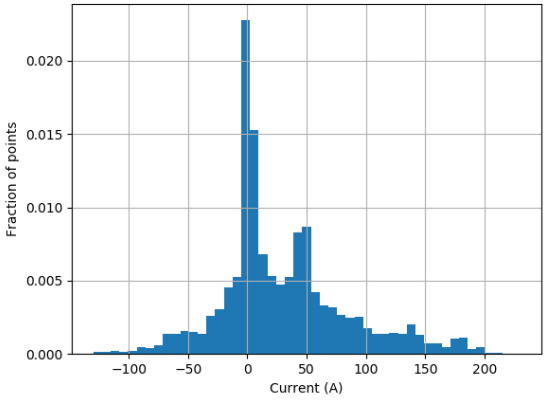

Figure 4.3: Distribution of the measured current for the vehicle movement.

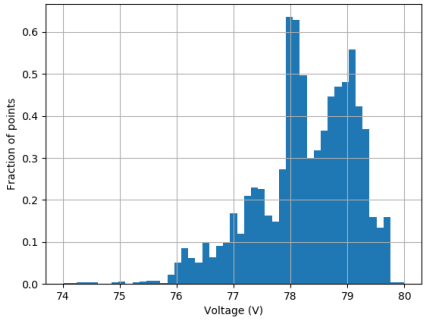

Figure 4.4: Distribution of the total voltage values.

Looking now at the **power** and **current distributions**, shown in figures 4.2 and 4.3, it can be seen that they have quite similar distributions. This is expected because the voltage value remains almost constant, as shown in figure 4.4. The oddest feature of these distributions is the existence of a very pronounced peak near zero for both of them, which is caused by the time the vehicle spends at rest. Another relevant property is that there are more positive than negative values for both power and current. This was expected because the vehicle spends more time in traction than regenerative braking.

4.1.2 Geographical Feature Distribution

In this section, the geographical distribution of some of the measured features was analysed. In order to do that, a discrete map of Lisbon was built with the resolution of 200m^2, which translates into one sample every 15m. The value presented in the graph is the average of the feature with coordinates inside each square.

In figure 4.5 it is possible to see the map of the **altitude** values provided by the GPS receiver, and in figure 4.6 it is shown the expected altitude taken from topographical data provided by *Mapbox*. The map can be seen in figure 4.12 and will be discussed further in section 4.2.1. At first glance, the maps seem to have the same qualitative behaviour, which seems to indicate that on average, the GPS provides a

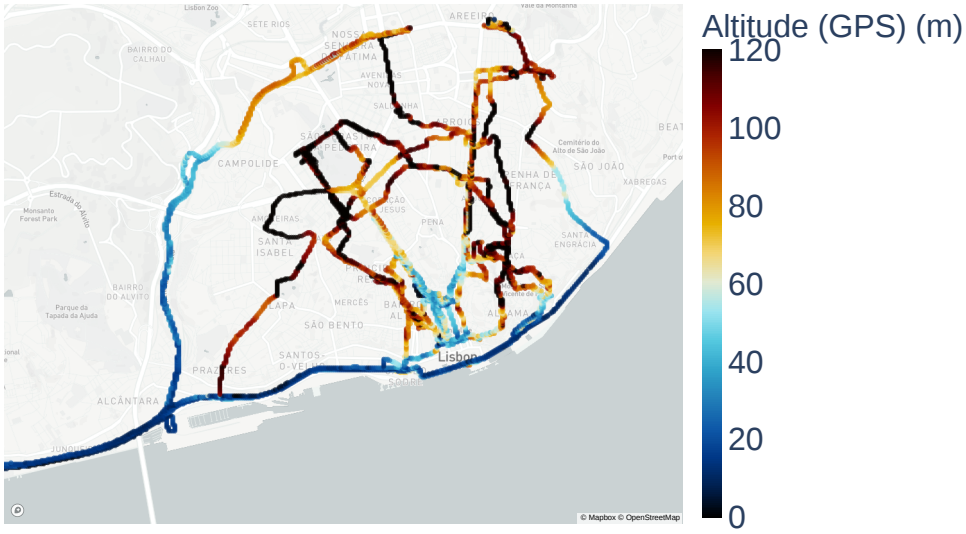

Figure 4.5: Geographical distribution of the GPS height measurements

qualitatively accurate prediction of the altitude values.

Nevertheless, as figure 4.7 shows, the error of the altitude predictions is still significant. It can be seen that the error is larger for the places where the change in height is the largest. Hence the error is not small, showing commonly values up to 60m. An error this large would cause a very large effect on the gravitational potential energy prediction, which is not compatible with the accurate prediction of the range. Because of this, the altitude was taken from the external topological data, as will be discussed further in section 4.2.1.

In figure 4.8 it is possible to observe the measured average velocity for the different coordinates measured. It is possible to see that the vehicle has higher velocities when it travels outside of the old town where the roads are in better condition and have less hazards to prevent, like people walking on the road, etc.

Figure 4.9 shows it can be seen the average power spent for different coordinates that were measured. It is possible to see that the power is higher in some regions where there considerable height variation in the height in the map of the figure 4.6. However, the way this map was made does not consider the direction in which the vehicle is travelling, which in irregular terrain will be determinant, either in increasing consumption when going uphill or decreasing in when going downhill. This causes the average power consumption to decrease, showing a considerable amount of point with a light blue colour.

4.1.3 Consumption Curve

With the data collected it is possible to estimate the **consumption curve** of the vehicle as a function of the velocity. For this, the regenerative braking was ignored, because we want to estimate how much the vehicle would spent on average as a function of the velocity. This might introduce a bias in the results

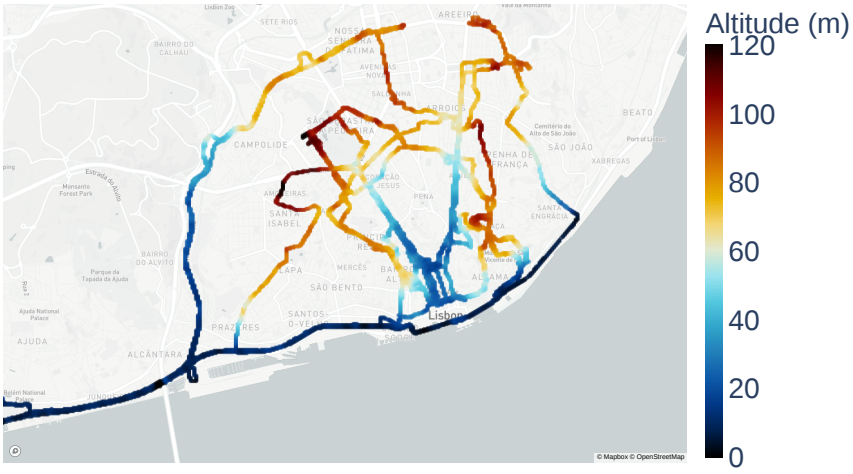

Figure 4.6: Estimated Height of the points as a function of the coordinates

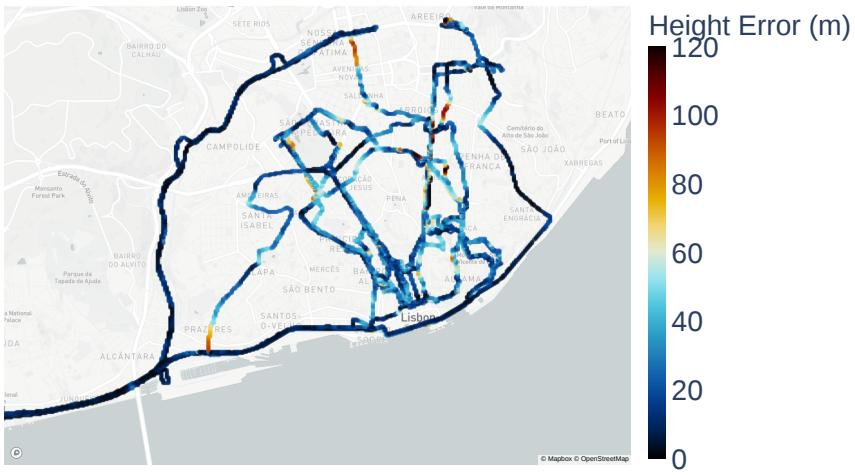

Figure 4.7: Geographical distribution of the error in the height

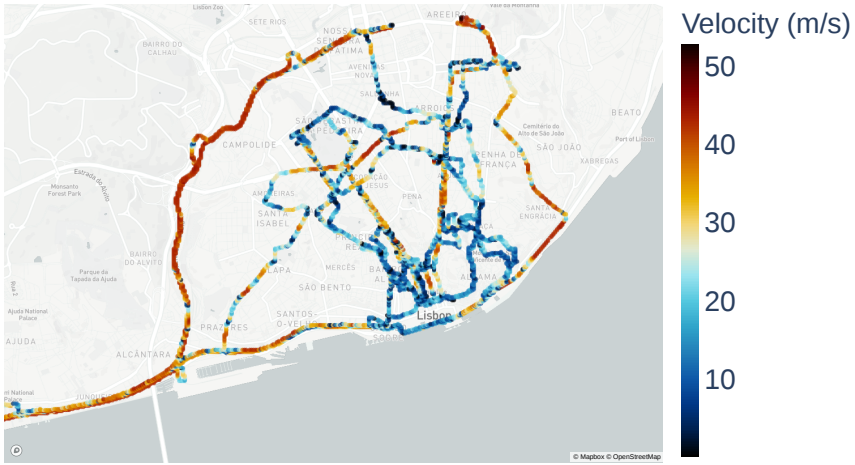

Figure 4.8: Average Measured Velocity for the different point coordinates

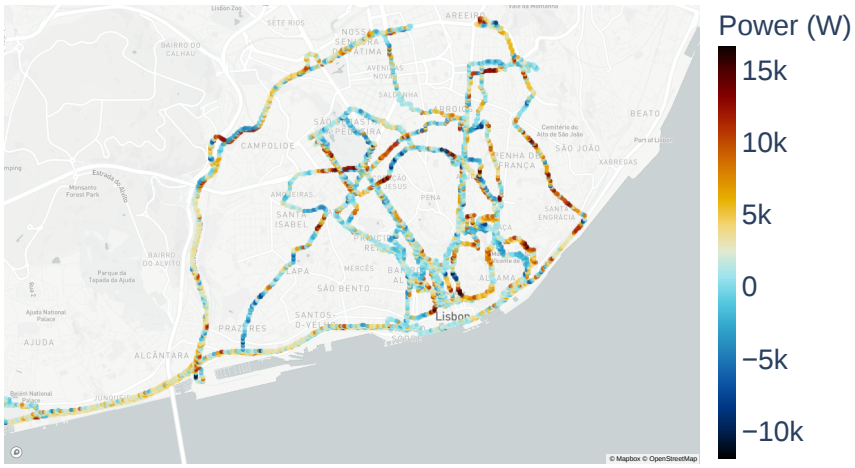

Figure 4.9: Average Measured power for the different coordinate points

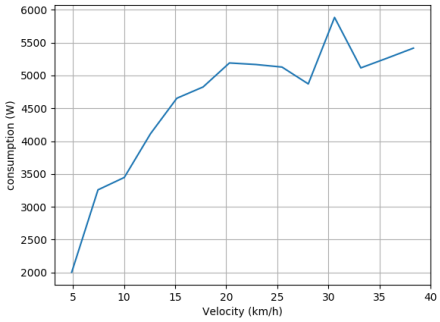

Figure 4.10: Average consumption as a function of the velocity of the vehicle for the **e-tuk Limo GT** vehicle.

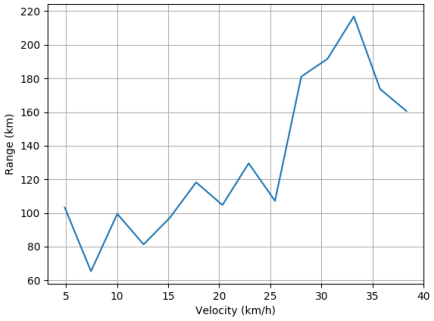

Figure 4.11: Average expected remaining driving range as a function of the velocity of the vehicle for the **e-tuk Limo GT** vehicle.

towards higher values of consumption. To build a more accurate consumption curve, constant velocity in a flat road should have been done for this vehicle in the same way as for the motorcycle.

The consumption curve was built by setting bins in the velocity values and computing the average consumption for the points with velocities inside those bins. Figure 4.10 shows the estimated consumption curve. As we can observe, the energy consumption increases as the velocity increases, which is to be expected because of the larger friction forces acting on the vehicle. The standard deviations of the values inside the bins is not presented because of its very large value, which is caused by the great range of values of power consumption for each velocity.

Another estimation that can be done is the expected range of the vehicle for the consumption estimated. This estimation can be done using equation 4.1, where E_{tot} is the total energy on the batteries when in full charge, P_i is expected power consumption and v_i is the velocity of the vehicle. Using this equation the range curve was determined and can be seen in figure 4.11 it is possible to see the range of the vehicle as a function of the velocity it travels at. This is what is to be expected since, for larger velocities, despite the larger friction, there is also a larger motor efficiency that has a dominant effect.

This will result in a more efficient use of the energy, which increases the expected remaining driving range (RDR) of the vehicle.

$$RDR = \frac{E_{tot}}{P_i} \cdot v_i \tag{4.1}$$

It should be noted that the data collected, as seen in the velocity distribution in figure 4.1(b) has a lower number of points for the intermediate velocity values. This may result in not having enough resolution in the bins to make accurate enough predictions of the range. In order to have better estimations the dataset needed to be bigger.

4.2 Derived Features

The data collected corresponds to sequences of individual measurements as a function of the time. But some of the important data was not directly measured, but can be derived from measured parameters, such as the road slope.

However sometimes this is not the best suited data format to work with. For some models it is better to work with aggregated data concerning small trip segments. These segments have been used in other studies (e.g. [56]) and can be referers to as *micro-trips*. To aggregate the trip data there is the need to extract other derived features (e.g., the length of the trip) which are computed in from the series of coordinate points over time.

This section is split into two parts. In section 4.2.1 it is explained how the real-time derived features were obtained from the data. Section 4.2.2 describes how the aggregated data that characterized the trip segments was obtained.

4.2.1 Real Time

Some of the important features to characterise the data were not measured, or measured with a considerable amount of error. This is the case of the **road slope**, which was not measured and also the case of the **altitude**, which contained a considerable amount of error. This led to the need for them to be derived from other features.

Altitude

Despite having access to the altitude data collected using the on-board GPS receiver, the accuracy that these measurements provide is not suficient for the model to be accurate enough. While this was already mentioned in section 4.1.2, we shall further elaborate on this subject. As another example of this, in figure 4.14 there are provided two graphs, above the altitude measured using the GPS, and below the altitude data taken from the altitude map in figure 4.12 using measured coordinates in figure 4.13. It can be seen that the height values measured by the GPS are very erratic and do not represent the height variation that would be expected as the graph below shows.

The map for the Lisbon city centre used was obtained through *Mapbox*, using their *Mapbox Terrain-RGB* API in *Python 3*, which provided one height measurement with 0.1m height increments for each square of area 17.5m^2. This can be translated into one measurement for every 5m. Nevertheless, the root altitude values provided by *Mapbox* are taken from the *Copernicus* EU project, which derives its data from a weighted average of the *Shuttle Radar Topography Mission* (SRTM) and *Advanced Spaceborne Thermal Emission and Reflection Radiometer* (ASTER). Both of these datasets have smaller area resolution and provide one altitude measurement for every 30 meters (square of area 900m^2). This tells us that the data provided by *Mapbox* is obtained through interpolation of much less accurate measurements. Because of this, the actual accuracy in the final map may be worse than the one it appears to have.

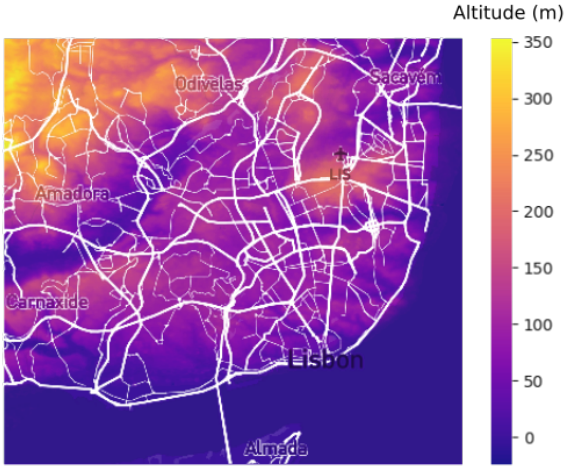

Figure 4.12: Elevation graph for the Lisbon Area considered in the *Copernicus* dataset.

Figure 4.13: Geographical distribution of the height values.

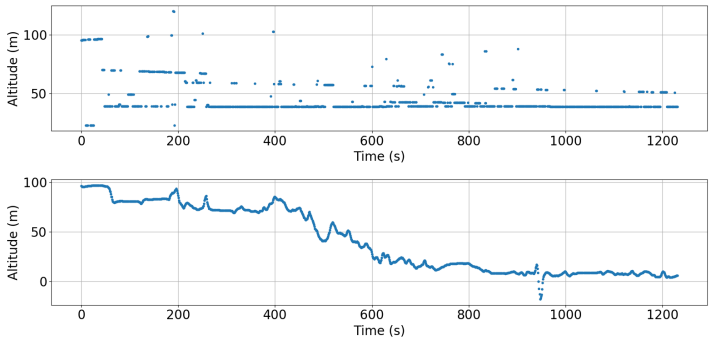

Figure 4.14: Altitude values measured using the GPS receiver (above), and the altitude values predicted using the topographical map (below).

However this is the most accurate dataset that is publicly available. With better height maps of the Portuguese military the results should be much better, but these maps would have to be bought at a considerable price. Because of this, the individual height measurements values ended up not being very reliable. However, for distant measurements it is possible to extract a more accurate height variation due to the error of the individual measurements being small in comparison.

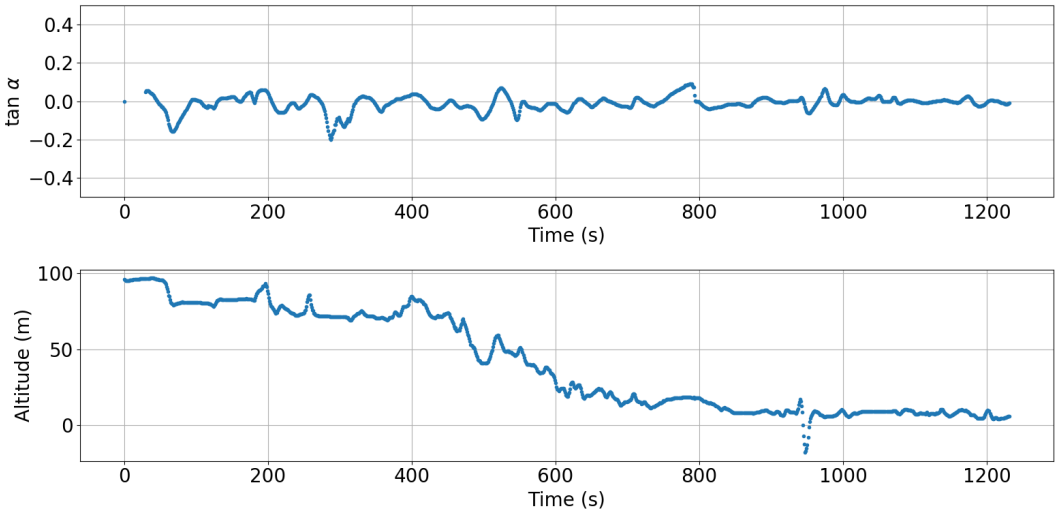

Figure 4.15: Slope estimation (above) and altitude profile (below) in an example vehicle trajectory. The slope estimation considered used 30 past points, which correspond to 9s of data acquisition.

Slope Estimation

The slope of the road is the angle (α) that the road makes with the horizontal, as can be seen in figure 2.4. Using the estimation of the distance travelled in the XY direction (Δs_{xy}), which will be described in the next sections as well as the height values estimated using the height map, it is possible to estimate the slope of the road using a *linear regression* model.

A general linear regression model calculates the line that provides the best fit to the data points. In this case the data is fitted to $(\Delta s_{xy_i}, h_i)$ points, where Δs_{xy_i} is the total distance travelled in the xy plane for the measurement of index i and h is the measured altitude at the same point. The linear model takes the general form shown in equation 4.2, where the coefficient β_1 is given by equation 4.3 and represents the tangent of the slope (α).

$$\Delta s_{xy_i} = \beta_0 + \beta_1 \cdot h_i \tag{4.2}$$

$$\beta_1 = \frac{\sum_i \Delta s_{xy_i} h_i - \frac{\sum_i \Delta s_{xy_i} \sum_i h_i}{n}}{\sum_i \Delta s_{xy_i}^2 - \frac{(\sum_i \Delta s_{xy_i})^2}{n}} = \tan\alpha \tag{4.3}$$

To determine the road slope at each point, an algorithm looks at the previous n estimations of the horizontal distance (Δs_{xy}) and the height and predicts the slope using the linear regression model already described. Figure 4.15 shows the estimated $\beta_1 = \tan\alpha$ value (above) for the altitude profile (below). The number of previous points considered in the example, as well as in the other predictions was of 30 acquisition points, which correspond to 9 seconds of vehicle movement.

4.2.2 Aggregated Data

In order to characterise the segments of the trips, it was built a set of **derived features**. These features include, for example, the *trip distance*. In the following sections it is shown how the **derived features** considered are computed.

Distance Estimation

The GPS receiver measures the sequence of locations of the vehicle. The location is given by a pair of values (λ, ϕ), where λ represents the latitude and ϕ represents the longitude. The distance between two successive points was determined using equation 4.4. Where E_R represents the *Earth Radius*, which was considered to be equal to 6371.0088km, and λ_m represents the average latitude of the two points. As the points are, on average, very close together, there will not be a very large difference in latitude, and the approximation will be valid.

$$\Delta s_{xy} = E_R \sqrt{\Delta\lambda^2 + (\cos\lambda_m \cdot \Delta\phi)^2} \tag{4.4}$$

An important note concerning equation 4.4 is that it gives the distance between two points at the same altitude. This is analogous to the distance in the plane xOy, as shown in figure 4.16. Therefore, the symbol used for this distance was Δs_{xy}. The total distance travelled, if the points have a different altitude is given by equation 4.5.

$$\Delta s_{tot} = \sqrt{(\Delta s_{xy})^2 + (\Delta h)^2} = \sqrt{(E_R \cdot \Delta\lambda)^2 + (E_R \cdot \cos\lambda_m \cdot \Delta\phi)^2 + \Delta h} \tag{4.5}$$

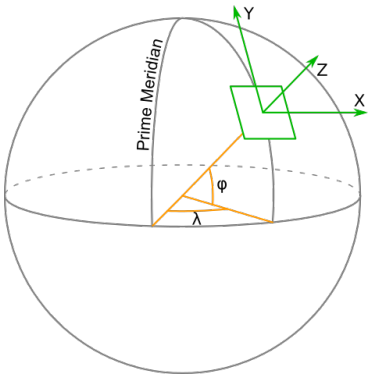

Figure 4.16: Representation of the X, Y and Z axis.

Velocity Integrals

In the lumped mass model, described in section 2.1.1, the energy of a trip segment is a function of both the integrals of the velocity and the square of the velocity over the distance travelled, as can be seen in equation 2.14. These values have to be estimated for every trip segment.

The estimation was made using a trapezoidal estimation of the integral, which are expressed in equation 4.6, where Δs_i is the distance between the acquisition point i and the previous point.

$$\begin{cases} \int_{x_i}^{x_f} v \cdot dx = \sum_i v_i \cdot \Delta s_i \\ \int_{x_i}^{x_f} v^2 \cdot dx = \sum_i v_i^2 \cdot \Delta s_i \end{cases} \tag{4.6}$$

To be more precise, the value of Δs_i should be the total distance. However due to the unreliability of the altitude data the distance considers only the variation on the plane.

Chapter 5

Trip-Based Prediction

As seen before, a common way to tackle the range anxiety problem is by planning the route in advance using a *route-planner* system. For a known route, it is then possible to predict the energy consumption of the vehicle over the duration of the trip and assure the driver that the charge is enough to reach the destination.

The *route-planner* is nowadays a common feature in the vehicle's board computer, which has made the implementation of this type of prediction directly in the board computer much easier than previously. Alternatively, other developed systems such as mobile applications, that commonly use the **Google Maps API** to extract both the traffic information and direction toward the destination as well as characteristics of the road[29].

In order to do an accurate prediction, an accurate vehicle model is needed to predict the energy spent for a given trip characteristics. This section will, therefore, focus on the problem of finding the best model (f) to predict the energy spent, as shown in equation 5.1, where x_i are trip features. For that we will make use of the different segmented trip datasets described in section 4.2.2, which contain the derived features from trip segments of different duration. This modelling is made in the segments because the prediction of the real time consumption was tried and concluded not to be possible, mainly because of the difficulty in determining the road slope from the height data.

$$\Delta E = f(x_1, ..., x_n) \tag{5.1}$$

In the following sections we present the results of the energy consumption predictions using different models. Various physics-based models based on the lumped mass model were used; namely an *a priori* method where the theoretically expected parameters are adopted and regression models where the parameters are extracted using different complexity models. Two different data-driven methods were also implemented, namely the decision tree and KNN regression models, which do not assume any physical model to the system.

In the first section, the main metrics to evaluate all the models are presented, in the second a short description of the input data used in each of the other parts is provided 5.2, then the results from the *a priori* model are presented, followed by the regression models and then the statistical models. The

chapter is finalised by making a comparative discussion of all the models.

5.1 Model Evaluation

In the following sections, the models are evaluated using the R^2 metric. This is a common metric used to evaluate regression models. It is based on the mean squared error and is commonly interpreted as the percentage of data variability that can be explained by the model. The R^2 is given equation 5.2, where SS_{res} is the sum of the squared error of the predictions and SS_{tot} is the sum of the squared error for the average value. In the final term of equation 5.2 y_i the measured value, f_i is the model prediction and $\bar{y}$ is the mean of the measured values[49].

$$R^2 = 1 - \frac{SS_{res}}{SS_{tot}} = \frac{\sum_i (y_i - f_i)^2}{\sum_i (y_i - \bar{y})^2} \tag{5.2}$$

For the regression model, the R^2 value presented is obtained considering all the points in the dataset. This cannot be done for the data-driven methods because, given their high non-linearity, they can start to over-fit to the training data, and stop having generalisation power. To avoid this, the data-driven models were tested using the K-Folds cross validation method with K=10 folds. This is a commonly used method in Data Science to validate models. It consists in splitting the data into K roughly equal parts, and then using $(K-1)$ parts to train the model, and the remaining part as the testing set [49]. The train-test cycle was repeated until all of the ten folds were used as testing. The value of R^2 presented for these models is the average of the R^2 values for each of the folds, as can be seen in equation 5.3, where R_i^2 is the R^2 for the fold i.

$$R^2 = \frac{1}{K} \sum_i R_i^2 \tag{5.3}$$

In the final section of this chapter, to evaluate the energy consumption prediction for a full trip, the metric used to compare the models is the relative error, as shown in equation 5.4, where ΔE_{meas} is the total measured energy consumption and ΔE_{pred} is the energy consumption predicted by the model.

$$e = \frac{\Delta E_{pred} - \Delta E_{meas}}{\Delta E_{meas}} \tag{5.4}$$

5.2 Input Data

In this section the data used in both the statistical models is described. The data used in the physical and statistical models differed from one another in the features used. As said previously, the features considered are computed over the course of a trip segment.

In the case of the physical models, the features are linked with known modelled physical phenomena, which were discussed in section 2.1.1 and contribute to the energy consumption. The features used in these models can be seen in table 5.1. The first feature considered was the variation of the velocity squared from the beginning until the end of the trip, which is associated with the kinetic energy variation

of the vehicle. The second and third features considered were the total distance travelled as well as the integral of the velocity in the distance, which are associated with the energy dissipated by the rolling friction force. Another feature considered was the integral of the velocity squared in the distance, which is associated with the energy dissipated by the aerodynamic friction. The final feature considered was the total height variation in the trip, which is associated with the variation of the gravitational energy of the vehicle.

$$\Delta E = \underbrace{\frac{1}{2} m \cdot (v_f^2 - v_i^2)}_{\text{Kinetic Energy Variation}} + \underbrace{c_r \cdot m \cdot g \left(\Delta s_{xy} + \int_{x_i}^{x_f} v \cdot dx \right)}_{\text{Rolling Friction Energy Dissipation}} + \underbrace{m \cdot g \cdot \Delta h}_{\text{Potential Gravitational Energy}} + \underbrace{\rho \cdot c_D \cdot A_f \cdot \int_{x_i}^{x_f} v^2 \cdot dx}_{\text{Aerodynamic Friction Energy Dissipation}} \tag{5.5}$$

Feature Name	**Expression**
Variation of the velocity Squared	$(v_f^2 - v_i^2)$
Total Height Variation	Δh
Total Distance Travelled	Δs_{xy}
Integral of the Velocity in the Distance	$\int_{x_i}^{x_f} v \cdot dx$
Integral of the Velocity Squared in the Distance	$\int_{x_i}^{x_f} v^2 \cdot dx$

Table 5.1: Features used in the physical models and respective expressions.

On the other hand, in the statistical models, the features used were different and more general, which might influence the energy, but are not directly connected to the energy consumption through a physical process. In table 5.2, the features used as inputs to the statistical models are shown. The variables considered include the average velocity and acceleration in the trip, as well as the total variation of height and total distance travelled

Feature Name	**Expression**
Average Acceleration	$\frac{1}{N} \sum_i a_i$
Integral of the Velocity Squared in the Distance	$\int_{x_i}^{x_f} v^2 \cdot dx$
Average Trip Velocity	$\frac{1}{N} \sum_i v_i$
Total Distance Travelled	Δs_{xy}
Total Height Variation	Δh
Trip Duration	Δt

Table 5.2: Features used in the statistical models and respective expressions.

All these input features were computed for trip segments of several durations. The models provided in the following sections show the results of the models as a function of the duration of the segment considered.

Name	Symbol	Expected Value
Drag Area	$C_d \cdot A$	$1.75m^2$ [11]
Rolling Coefficient	c_r	0.012 [11]
Vehicle Mass	v_m	829.4(sec. 3.1.4)

Table 5.3: Coefficients sed in the the *a priori* model of **e-tuk Limo GT**.

5.3 *A priori* Physical Model

In this section, it is presented the implementation of the *a priori* model. That is to say that this model uses no data collected from the vehicle to base itself on. The prediction is then based only on what is theoretically expected. The study of this type of model is relevant from the mass production stand point, because it can be very easily generalised for similar vehicles without the need for calibration or testing to find the correct vehicle parameters. It is the very first approach that can be taken to predict the energy consumption, and is commonly used in simulations. With a good estimation of the model parameters, good results are expected to be achieved.

This model is based on the **lumped mass model** described in section 2.1.1 and takes the form of equation 5.5, shown previously. The parameters used in this section are some typical values expected for a vehicle of this type. The parameters used can be seen in table 5.3, where both the rolling and aerodynamic coefficient were taken from the model developed in [11], and the vehicle mass was estimated previously in section 3.1.4. This estimated mass does not consider any payload, which renders it unrealistic for the real world operation of the vehicle. However, it is not possible to have an accurate estimation of the payload for the whole data collected because the vehicle changes its number of passengers over time from one to up to seven. Because of this, in this estimation it was considered an average payload of 170 kg, which puts the total mass of the vehicle in the nice round number of 1000 kg.

In figure 5.1, the evolution of the R^2 as a function of the trip segment considered is shown. We can clearly see an increase in performance as the segment duration increases. This has been seen in all of the models implemented, and seems to indicate that the data becomes increasingly well behaved for bigger segments. This is to be expected, because, as described in section 4.2.2, derived features, such as the distance and the velocity and squared velocity integrals, will become larger, dominating over the effects of random noise.

After the initial increase, R^2 remains somewhat constant, indicating that there is not much to be gained for segments longer than 100 seconds. A decline in model performance for segments longer than 600 seconds can also be ovserved. This can be due to the very long length of the segment, which causes it to have a large amount of regenerative braking within it. One of the drawbacks of this model is that it considers the regenerative braking efficiency to be always 100%.

Finally, the model was tested for real trips. The prediction of the total energy consumption of the vehicle was made predicting the energy for each segment and summing up to get the total value of the energy spent. Figure 5.2 shows the distribution of the relative error for the bigger trips taken by the vehicle. The average error obtained was -32%, which indicates that the model is underestimating the energy. This can be due to the underestimation of the friction coefficients. It can also be seen that the

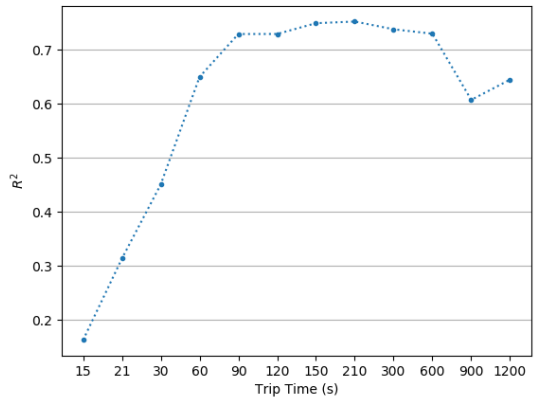

Figure 5.1: R^2 variation with the trip segment duration for the **physical model** (x axis not to scale).

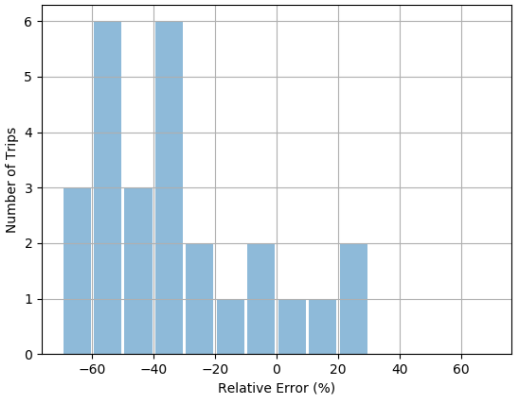

Figure 5.2: Relative error distribution for trips with $\Delta E > 1AH$. Average error was -32% and the standard deviation 27%

standard deviation value is also quite large (27 %) which shows that the model does not fit the data well.

5.4 *A priori* Physical and Electrical Model

The previous model considered only the physical properties of the vehicle. However, it is known that the motor efficiency changes prominently depending on the operation point of the motor. To characterise the efficiency of the motor it is common to use the efficiency map. This map is often represented as a function of the torque and velocity acting on it.

To build an accurate vehicle model that considers both the chassis model and the power-train characteristics of the vehicle, the efficiency of the **power-train** of the vehicle needs to be made. This value represents the joint efficiency of all the components that allow the transmission of the power from the batteries to the wheels, i.e., the motor, power-converter, controller and differential[25].

5.4.1 Efficiency Map Estimation

Unfortunately, no data concerning the efficiency of the motor of the vehicle was not provided by the manufacturer. In addition, the company owning the vehicle had no spare motor to lend so that the appropriate measurements could be done in an adequate test bench. Nevertheless, using the *a priori* model described in the previous section it was possible to estimate the mechanical power pumped into the vehicle, using equation 5.6, where F_t is the traction force given by the lumped mass model as shown in equation 5.7.

The acceleration was estimated using a linear regression to the previous three seconds of velocity values and extracting its rate of change. The slope was also estimated using the linear regression as shown in section 4.2.1. The values of velocity used were the instantaneous measured by the GPS. Lastly, the vehicle parameters used were the ones used in the previous section 5.3.

$$P_{mec} = v \cdot F_t \tag{5.6}$$

$$F_t = m\frac{dv}{dt} + c_r \cdot m \cdot g \left(\cos\alpha + \frac{v}{44.4}\right) + m \cdot g \cdot \sin\alpha + \rho \cdot c_D \cdot A_f \cdot v^2 \tag{5.7}$$

The *power-train* efficiency can be estimated using the power measured in the batteries, as given in equation 5.8. This efficiency is a function of the torque as well as a function of the angular velocity of the motor. The torque was estimated using equation 5.9 and the angular velocity of the motor using equation 5.10.

$$\eta(T, \omega) = \frac{P_{mec}}{P_{meas}} \tag{5.8}$$

$$T = \frac{R_{tire} \cdot F_t}{G_{ratio}} \tag{5.9}$$

$$\omega = \frac{v}{R_{tire}} \tag{5.10}$$

To build the efficiency map, the values of P_{mec} as well as P_{bat} were split in two dimensional bins as a function of their torque and velocity values. The values of the efficiencies were averaged inside the bins to build the two dimensional map that can be seen in figure 5.3(a). In this figure, a clear trend cannot be seen, because of the considerable amount of error in the measurements since some of the bins are still under-represented. A Gaussian filter was, thus, applied to the data to smooth the transitions and make clear the data trend. The resulting data can be seen in figure 5.3(b).

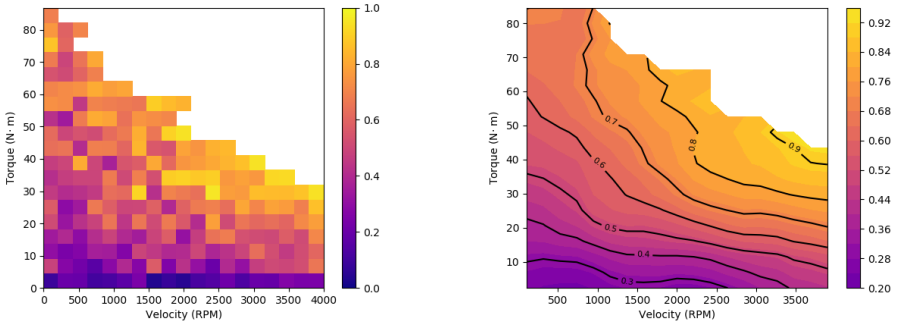

(a) Raw data collected.

(b) Data after application of a Gaussian Filter.

Figure 5.3: Different representations of the estimated efficiency maps of the motor of the **e-tuk Limo GT**.

The efficiency maps shown in figure 5.3 give only the motor working in positive torque region. The data obtained for the negative torque with the Gaussian filter can be seen in figure 5.4. Due to the small sample size, the braking efficiency was considered constant and equal to 50%

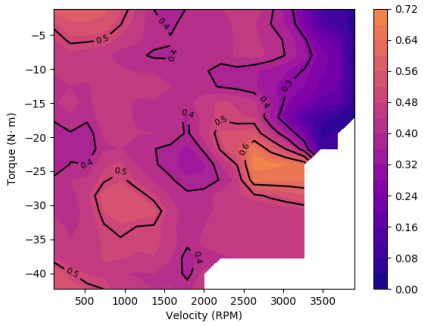

Figure 5.4: Regenerative braking efficiency during regeneration using a gaussian filter.

5.4.2 Power Consumption Estimation

Using the efficiency map, it is possible to estimate the instantaneous power consumption of the vehicle as a function of time, using equation 5.11. The estimations of F_{tot} are made considering the coefficients of table 5.3.

$$P_{tot} = \eta(T, \omega) \cdot v \cdot F_t \tag{5.11}$$

Figure 5.5 shows the consumption estimations of the vehicle as a function of time. Examples 2 and 3 are taken from areas close to the river in Lisbon, with road slopes that are almost zero, while example 1 is taken from the Lisbon city centre, where the slope is higher. It can be seen that the power consumption predictions fail when the battery power is constant, which was hypothesised to be due to the unreliable estimation of the road slope.

Because of this, the predictions were also made for the model without including the gravity term in the predictions, which can be seen in figure 5.6. It can be seen that the gravity term is causing the results to worsen. A possible reason for this is the inaccuracy of the height estimations that causes the unstable predictions of the road slope. It is possible to see that the predictions are much closer to the measured values in the case of examples 1 and 2, where the slope is expected to be low. This improvement dos not happen for example 1, where there is a higher slope.

The overall inadequacy of the consumption predictions make it almost impossible to predict the instantaneous consumption of the vehicle. Because the instantaneous consumption values could not be estimated, this method could not be further applied to the estimation of the energy consumption on the trip. If we have inaccuracy in the individual consumption, the integral will also not have the required accuracy. It was, however, possible to estimate of the efficiency map of the vehicle motor.

5.5 Regression Model

The first logical step towards improving upon the *a priori* model is to try to provide better estimations for the model parameters. Using the general equation of the lumped mass model described before (section 2.1.1 and equation 5.5), it is possible to apply a least squares regression to the data collected and

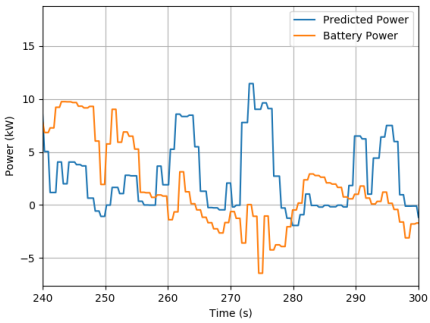

(a) Example 1

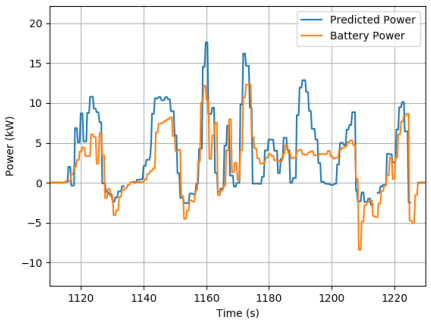

(b) Example 2

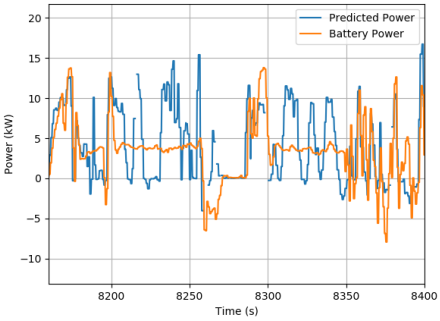

(c) Example 3

Figure 5.5: Three examples of consumption values estimated for the full lumped mass model.

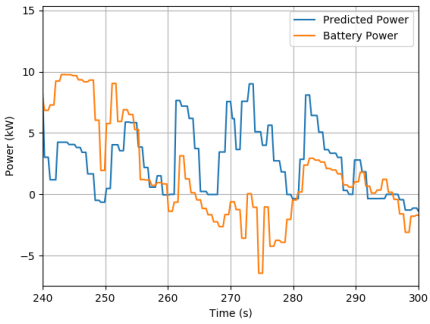

(a) Example 1

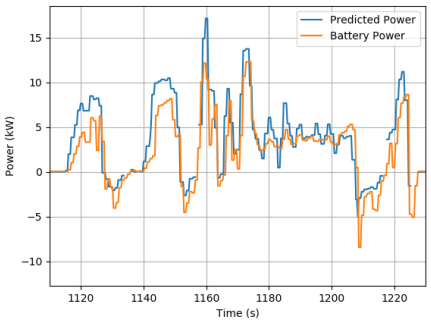

(b) Example 2

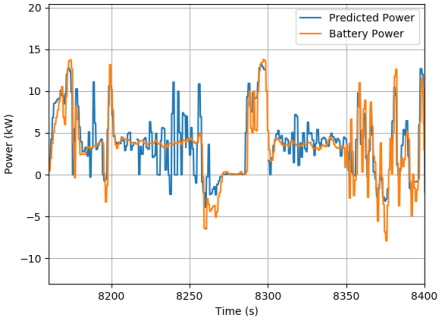

(c) Example 3

Figure 5.6: Three examples of consumption values estimated for the lumped mass model without gravity.

determine the model parameters that are better suited to describe it.

As seen in chapter 4, the velocity values do not go above the 45 km/h mark. In the lumped mass model both the aerodynamic friction term and the velocity term on the rolling friction, gain relevance as the velocity increases. This raises the question of whether these terms are really important for this particular vehicle or not. To solve this question, in this section the least squares regression is applied to three different models, that progressively increase in complexity, as shown in table 5.4. The first model (**model 1**) did not consider the aerodynamic friction or the dependence of the rolling friction on the velocity of the vehicle. The second model (**model 2**) adds the effect of *aerodynamic friction* acting on the vehicle. The third model (**model 3**) considers the effects of both the aerodynamic friction and the velocity term of the rolling friction.

The purpose of this section is to both provide better predictions than the ones in the *a priori* model and to ascertain if the aerodynamic term or velocity term in the rolling friction really are relevant for the vehicle in analysis.

Model 1	$\Delta E = \frac{1}{2}m \cdot (v_f^2 - v_i^2) + c_r \cdot m \cdot g\Delta s_{xy} + m \cdot g \cdot \Delta h$
Model 2	$\Delta E = \frac{1}{2}m \cdot (v_f^2 - v_i^2) + c_r \cdot m \cdot g\Delta s_{xy} + m \cdot g \cdot \Delta h + \rho \cdot c_D \cdot A_f \cdot \int_{s_{xy_i}}^{s_{xy_f}} v^2 \cdot ds_{xy}$
Model 3	$\Delta E = \frac{1}{2}m \cdot (v_f^2 - v_i^2) + c_r \cdot m \cdot g\left(\Delta s_{xy} + \int_{s_{xy_i}}^{s_{xy_f}} v \cdot ds_{xy}\right) + m \cdot g \cdot \Delta h + \rho \cdot c_D \cdot A_f \cdot \int_{s_{xy_i}}^{s_{xy_f}} v^2 \cdot ds_{xy}$

Table 5.4: Equations of the three regression models used.

This model considers only the physical effects of the applied forces and ignores losses in the electrical components, such as the varying efficiency of the motor, as well as the losses in the power-train.

5.5.1 Results and Discussion

As the results obtained for the three models did not differ considerably, in this section we present the results obtained and analysis for all the models. Figure 5.7 shows the R^2 of the models as a function of the trip segment considered. It is shown that the model has a good fit to the data and that R^2 is close to 1.

In figure 5.8, it can be seen the variation of the rolling friction as a function of the trip segment duration considered. We can see that, as the duration increases, the model becomes more accurate. One of the reasons for this was that, as described before, as the segments get bigger, the variables in which the model depends become dominant: larger distances (Δs_{xy}), height variations (Δh) as well as larger values of the velocity and squared velocity integrals ($\int v \cdot dx$ and $\int v^2 \cdot dx$). Because of this, the contribution of the error of each of the measurements becomes smaller, when compared with the other variables. This effect was mainly observed in the gravity term.

Figure 5.8 shows how the model parameters estimated vary with the trip segment that is considered. They all follow a similar trend, in the sense that they all stabilize in a constant value as the trip segment sizes increase. This is to be expected because we know form R^2 that the accuracy of the model gets better for larger trips.

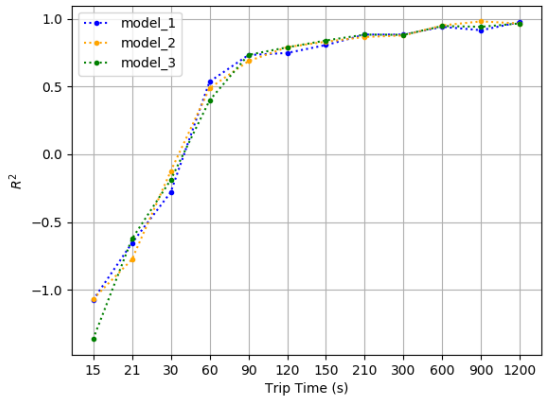

Figure 5.7: R^2 values as a function of the trip segment for the three models considered.

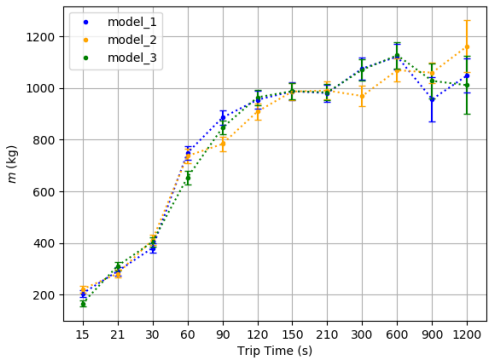

(a) Vehicle Mass (v_m)

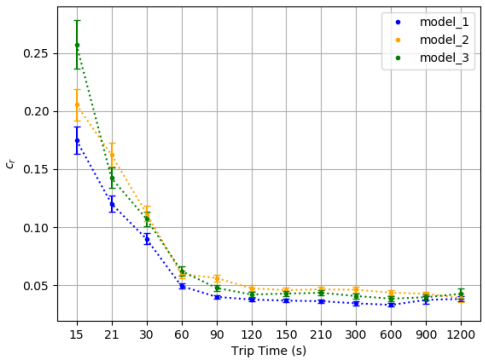

(b) Rolling Coefficient (c_r)

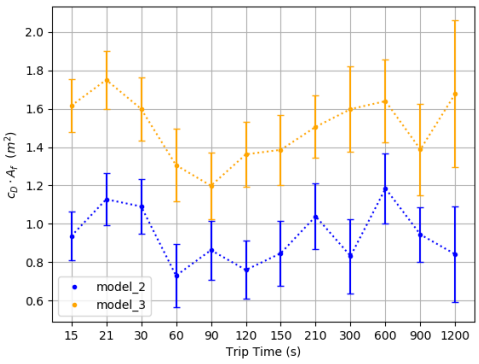

(c) Aerodynamic Coefficient ($c_D \cdot A_f$)

Figure 5.8: Details of the estimated model parameters for different trips and different segment lengths

Figure 5.8 shows the predicted values of the model coefficients. Figure 5.8(a) shows the estimation of the **vehicle mass**. This estimation is close between models 1 and 3, but there cannot clearly be seen consistent difference between one model and the other. Most importantly, it is shown that the predicted vehicle mass is close to the expected value of 1000kg. The apparently random variations can be explained by the variations the vehicle has in payload that cause inconsistencies in the data from

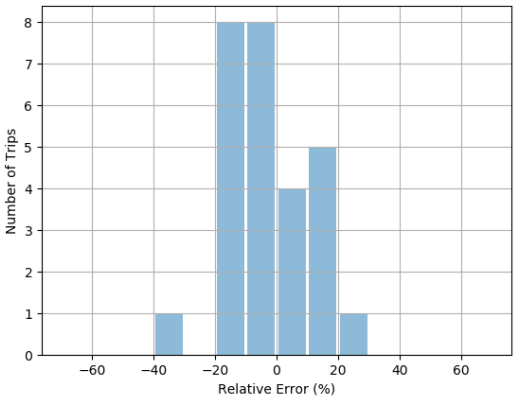

Figure 5.9: Relative error distribution for trips with $\Delta E > 1AH$. Average error was -3% and the standard deviation 13%

segment to segment.

In figure 5.8(b), the estimations for the **rolling coefficient** can be seen. The first thing that comes to mind is that the values are much higher than it would be expected for rolling coefficient of wheels rolling over concrete, which were expected to vary form 0.010 to 0.015. This can be explained by the fact that the vehicle does not move in concrete for a lot of its travel time, since the vehicle spends a considerable amount of time travelling in old-town Lisbon, as seen in section 4.1.2. In this part of town it is common to find bumpy roads, with considerable amounts of holes, which cause the tires to slip and increase the rolling coefficient by a considerable amount. In addition to this, it can be seen that the model 2 produces consistently the highest values of the rolling friction followed by model 3 and model 1.

Figure 5.8(c) shows that the third model produces the highest values of aerodynamic coefficient. The values predicted for the value of $c_D \cdot A_f$ are smaller, but close to what would be expected for the vehicle in study.

Figure 5.9 presents the distribution of the errors for the regression model. The results were very similar for all of the three models used, therefore only model 3 is presented to avoid redundancy. It is possible to see that there is a low bias in the models, because of the low average error of 3%. But the model still presents some imprecisions causing a relatively low standard error deviation of 13%.

5.6 Statistical Models

In this section, two different data-driven statistical models were implemented: the decision tree and KNN regression models. The implementation of these algorithms are those of *sklearn* Python library and for training it was used the same aggregated trip data described in section 5.2. These non-linear models are expected to capture the non-linearities of the vehicle energy consumption such as those caused by the varying motor efficiency. As mentioned before, for these models the performance is evaluated using a 10-Fold cross-validation strategy for different aggregated data of trip segments.

5.6.1 Decision Trees

The decision trees regression was implemented using the class **DecisionTreeRegressor** from the *sklearn* Python library, an implementation of the algorithm outlined in section 2.2.1. This class allows the customisation of different hyper-parameters to tune the model, such as the maximum depth of the tree, the minimum number of samples required to make a split, and the minimum number of samples per terminal node. These three parameters were varied in order to find their effect on the final results and find an optimal set of parameters to use. The results obtained can be seen in figure 5.10.

Figure 5.10(a) shows the R^2 curve for different trip durations and different maximum tree depths. This parameter corresponds to the maximum number of levels in the tree; in other words, it represents the maximum number of decisions before reaching a terminal node of the tree. This was the parameter that affected the results the most. It is possible to see that the performance gets better for larger depths, but only until a maximum depth of 4 levels, after which the increase in complexity of the model stops impacting performance.

Figure 5.10(b) shows the variation of the R^2 curve as the number of samples required to split the tree increases. This parameter corresponds to the minimum number of samples in a node for the introduction of a new split in the tree. It can be seen that as the minimum number of samples required to split the tree increases, the performance gets slightly worse.

Finally, in figure 5.10(c), the effect of the variation of the minimum samples per terminal node in the R^2 curve can be seen. This parameter is the minimum number of training samples inside each of the terminal nodes. The smaller this value is, the more complex the more splits the model will have and thus the more complex. Just as in the case of the minimum number of samples per leaf, the bigger this parameters the performance gets slightly worse.

The final parameters chosen for the decision tree used were a maximum depth of 4, and the default values of 2 and 1 for the minimum number of samples per split and minimum samples per leaf, respectively were chosen.

The final decision tree results can be seen in figure 5.11, it is noticeable, as before an increase in the performance of the model, until a *plateau* beyond which the model performance decreases. This is due to the training set becoming smaller which causes the model to not have enough data to make accurate predictions.

Figure 5.12 depicts the distribution of the error values. Because of the low value of error it is possible to see that the model is not biased toward any side, but it contains a still relevant lack of precision as can is evidenced by the relatively high standard error deviation.

5.6.2 K-Nearest Neighbours

Similarly, the KNN regression was implemented using the **KNeighborsRegressor** class of the *sklearn* Python library. This library allows the customisation of different parameters of the model such as the number of neighbours (K) to consider in the prediction, the distance metric and the weights to use for the different points. Figure 5.13 shows how the different parameters affect the model performance.

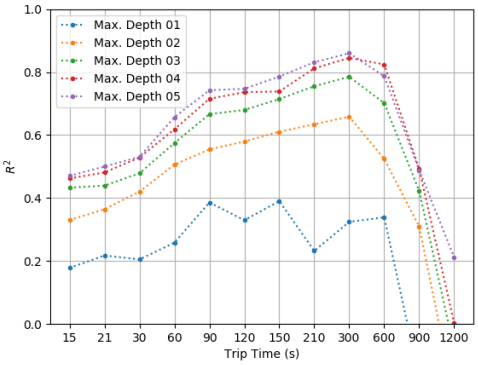

(a) Maximum Depth.

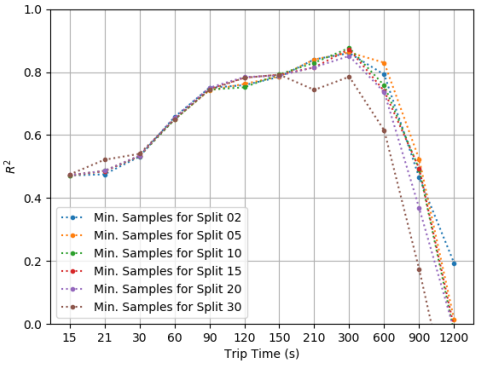

(b) Minimum Number of Samples for Splitting.

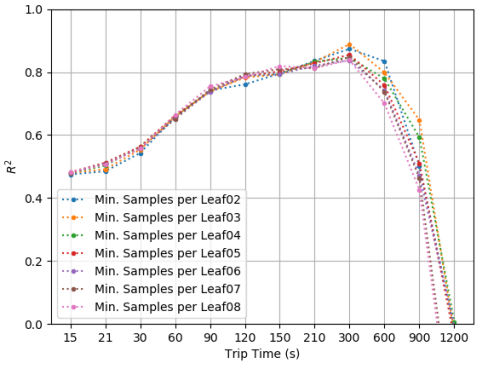

(c) Maximum Depth.

Figure 5.10: R^2 curves for the different parameters of the Decision Tree model, as a function of the trip length.

Figure 5.13(a) presents the R^2 curve for different number of neighbours considered. It is possible to see that the performance improves considerably as more neighbours are considered, but the improvement is not considerable for the neighbours above 40. Figure 5.13(b) shows that better results were obtained using uniform weights, and in figure 5.13(c), it is observed that there is a small difference between the distance metrics that are considered. Because of this, for the KNN model there were considered 40 neighbours, uniform weights and the default euclidean distance metric.

The KNN regression model was applied to the different duration segments that were used in the training of the model. In figure 5.14 it is possible to see the variation of R^2 of the model for the different trip lengths. The general behaviour is similar to the decision tree regression, but with a performance considerably worse overall. This decreased performance is manifested in a value for R^2 much smaller than the one obtained for the previous models. As seen before, there is also an increase of the R^2 with the trip duration, and a decline when the dataset becomes too small to ensure accurate predictions.

Figure 5.15 depicts the distribution of the trip errors. The average error is small (7%) which indicates that it is not biased, but the standard deviation of the error is still very large, which could already be expected given the low R^2 value.

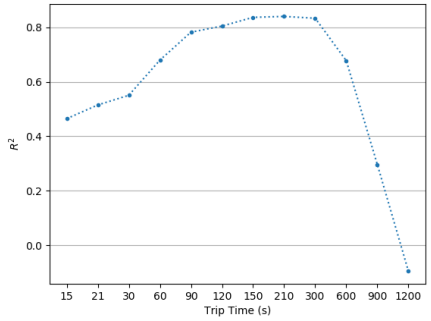

Figure 5.11: R^2 for different trip durations for the Decision Tree model

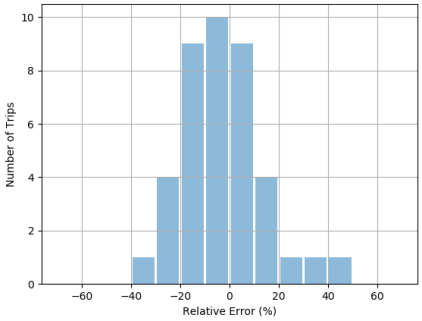

Figure 5.12: Relative error distribution for trips with $\Delta E > 1AH$ using the KNN model. Average error was 1% and the standard deviation 26%

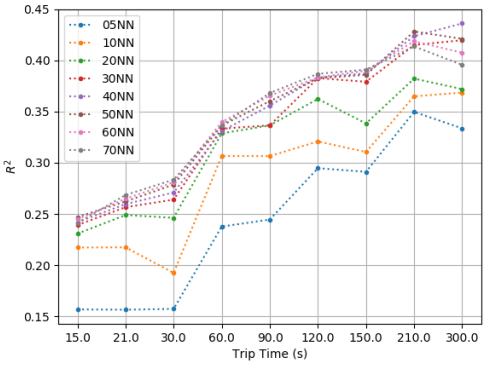

(a) Number of Neighbours.

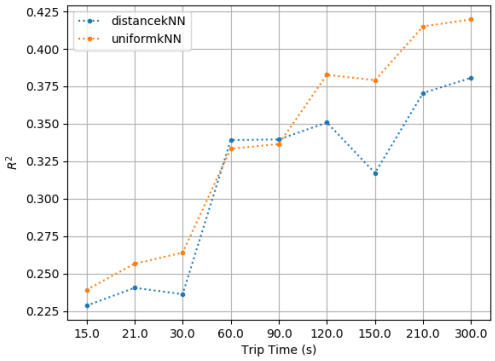

(b) Point Weights.

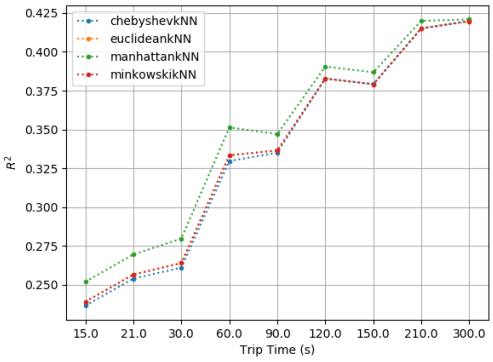

(c) Distance Metric.

Figure 5.13: R^2 curves for the different parameters of the KNN model, as a function of the trip length.

5.7 Model Comparison

In this section we compare the results obtained for the different implemented models, and provide a discussion of the pros and cons of using each model. A summary of the main conclusions of the chapter is also provided. The grouped results obtained can be seen in figure 5.16.

The most striking difference between the data-driven models (KNN and decision tree) and the

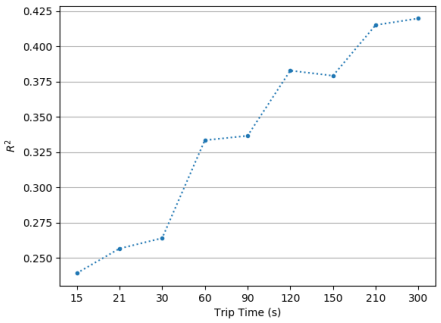

Figure 5.14: R^2 for the final KNN model as a function of the trip duration considered. (X axis not to scale)

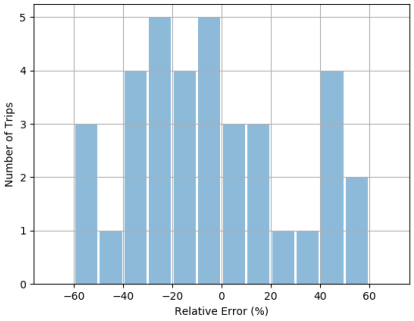

Figure 5.15: Relative error distribution for trips with $\Delta E > 1AH$ using the KNN model. Average error was 7% and the standard deviation 52%

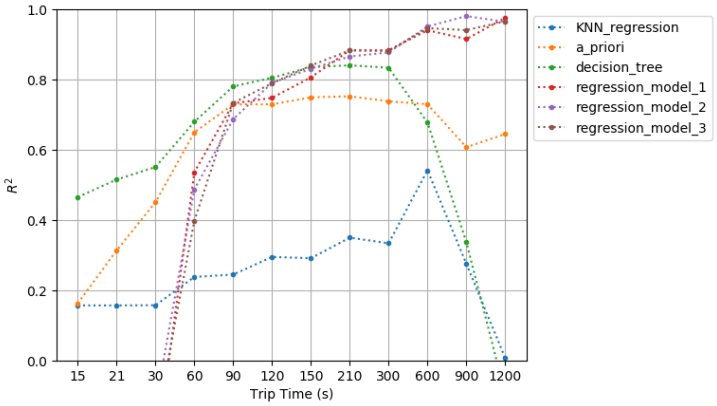

Figure 5.16: Joint Representation of the R^2 for all the models that were used to describe the vehicle as a function of the trip segment duration.

physics-based models (*a priori* and regression models) is that, for longer trip segments, the data-driven models start to fail. This happens because, as said before, the larger the trip segment the smaller the dataset, and the dataset becomes smaller than the necessary for the model to make accurate predictions. On the other hand, the physics-based models already have the information of the vehicle model and can more easily generalise from smaller datasets.

From the data-driven models we can see that the decision tree model provided the best performance. From the physics-based models, the one that provided the best results were the regression models, with small differences between the models, as already discussed in section 5.5.1. But the *a priori* model showed the best results for the smaller trip segments, where the regression models could not find the accurate model parameters to describe the vehicle.

Table 5.5 is a compilation of average errors and standard error mean deviation data for the different models using a segment of duration 150s. We can see that the standard deviation of the error closely follows the performance expected by the R^2 value of the models. However, it is possible to see that it is not quite the case for the bias. It is observed that the model which has the most (absolute) bias, with 32%, is the *a priori* model, followed by the KNN model, with 7%. The model that had the less bias was the decision tree model, despite the fact that the R^2 value was higher than the regression model.

Model	Average Error (%)	Standard Deviation (%)
Regression Model	3	13
A priori Model	-32	27
KNN	7	52
Decision Trees	1	26

Table 5.5: Average and standard deviation of the error values for the different methods for segments of duration of 150s.

Chapter 6

Real Time Approach

In the previous section there were applied different models to the prediction of the energy consumption of the vehicle for a given known trajectory. However, this can only be done when the trajectory is known beforehand, using a route-planner system which might not be readily available. In addition to this, it also important for the driver to have access to a prediction of the total remaining range, without the need for planning every single trip in advance. This will equip the driver with an overall knowledge of the total range available to him at all the times.

The focus of this chapter is to implement and test, using the real-world data collected, a system that allows the estimation of the vehicle range without the knowledge of the future vehicle trajectory. This represents a different problem than the one solved in chapter 5, because now not only do we not have access to the future information concerning the vehicle trajectory, but also we want to predict the remaining total range in stead of the total energy consumption. We also aim develop a real time prediction in stead of the one time energy prediction developed in the previous section.

The real time estimation model implemented was a **history-based** model, which estimates the future behaviour of the vehicle using its past values. In order to do that it considers the future consumption to equal the past. For the model presented, the past consumption is estimated using a moving average approach, with different methods for choosing the window of values to average on.

In the following sections we provide first some background about the method used to estimate the consumption in section 6.1, explaining the general idea and how it was used to make the range prediction. We then show how the points were preselected in order to avoid undesirable effects in section 6.2 and explain how the calibration of the model was done in section 6.3. Finally we show the results for the two different forms of model implemented (sections 6.4 and 6.5) and make a comparative analysis between them (section 5.7).

6.1 Moving Average

The method that that was used to implemented in the range prediction described in this chapter was the moving average method. This is a commonly used method in *time series* analysis which has the purpose

of smoothing the time series reducing its short lived variations, and estimating the average of the past values of the series [57]. The general form that a moving average takes can be seen in equation 6.1, where the y_t are the values that the series takes for time t, and N is the length of the moving average window [58].

$$MA_i(y) = \frac{y_t + y_{t-1} + ... + y_{t-(N-1)}}{N} \tag{6.1}$$

This method eliminates completely any regular variation with the same oscillation period as the window. However, any variation with a different periodicity is only damped and never completely eliminated [59]. In the case of this study, the vehicle consumption does not have predictable periodic variations. Because of this, the moving average will only dampen the variations in energy consumption. This is a favourable characteristic to have because it shows that the model has the ability to variations in consumption values.

If the data is not centred, the moving average is often lagging behind around by half of the sample size[59]. This, on the other hand, is not desirable characteristic and, for bigger samples, will have a non-negligible effect, that we should be aware of.

In this particular case, we want to estimate the consumption per distance travelled by the vehicle ($\bar{p}$). In order to do that, two moving averages are computed as shown in equation in equation 6.2, where $MA_i(I)$ and $MA_i(\Delta s)$ represent the moving average values for time t of the current consumed and the distance travelled by the vehicle. Both of the moving averages are computed in the same way and for the same window. This estimation allows us to then estimate the RDR of the vehicle using equation 6.3, where SOC_t is the instantaneous state of charge in the battery provided by the BMS.

$$\bar{p}_i = \frac{t_w \cdot MA_i(I)}{MA_i(\Delta s)} \tag{6.2}$$

$$RDR_i = \frac{SOC_i}{\bar{p}_i} \tag{6.3}$$

In order to use the moving average method as a range estimation there is one key assumption that has to be done, which is that the past values will remain constant in the future. This is a fairly loose assumption, which can only be applied in cases where the consumption values remain more or less constant. It is expected that it will fail when there are sudden changes in consumption. Considerable changes can happen when there are sudden road slope variations or shifts in environmental factors such as change road conditions, driver aggressiveness, etc..

The prediction will adjust as the time goes by, but these unexpected variations can put the inexperienced driver in a situation where despite the range prediction system indicating enough range to reach to the destination, the change in the consumption profile can rend the destination now unreachable.

Therefore, the consumption prediction should have some stability to be reliable. But it should also not be completely stable, to allow the driver to have an accurate prediction, depending on the driving conditions. To do that there should be found a compromise between the two with the window that is

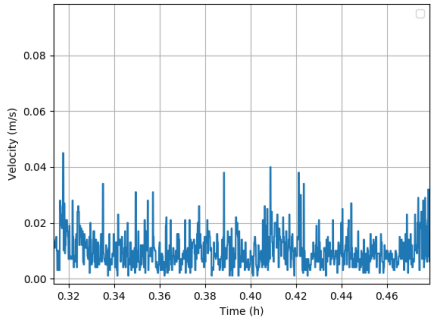

Figure 6.1: Example of the velocity measurements for a vehicle at rest

chosen.

In the following sections there will be discussed different methods for determining the previous consumption as well as considerations regarding the time and distance windows to consider.

6.2 Data Selection

As seen previously in chapter 4, there is a considerable amount of acquisition points where the vehicle is at rest, yet still acquiring data. When the vehicle is at rest, the moving average estimation of the distance will approach zero. As it is in the denominator of equation 6.2 the consumption estimation will increase considerably, affecting the stability of the predictions.

In order to avoid this effect the points were filtered out. The way this was done was using the velocity value, and defining a threshold below which the points were ignored in the moving averages. In figure 6.1 it can be seen the velocity measurements during a time where the vehicle is at rest. From that graph we can see that the velocity values do not exceed the 0.1 m/s. This was the case for all the points where the vehicle was at rest. Therefore, the points bellow this threshold were not considered in the moving average.

In addition to this condition, another filter was implemented in order to filter out the points where there was a wrong reading of the series communication.

6.3 Calibration

When making the first range predictions, using equation 6.3, it was verified that the predicted vehicle range was consistently above the measured. Two examples of this effect can be seen in figure 6.2. This indicates that the consumption is being underestimated. One possible reason why this happens is the low sampling frequency of 3Hz that is being used. This frequency is not enough to capture the finer details of the current profile, and thus can cause underestimation of the current integral.

Because of this, it was determined a calibration factor (f_{cal}) to multiply by the range estimation in order to bring it closer to the measured values. To estimate the calibration factor we compute for all of

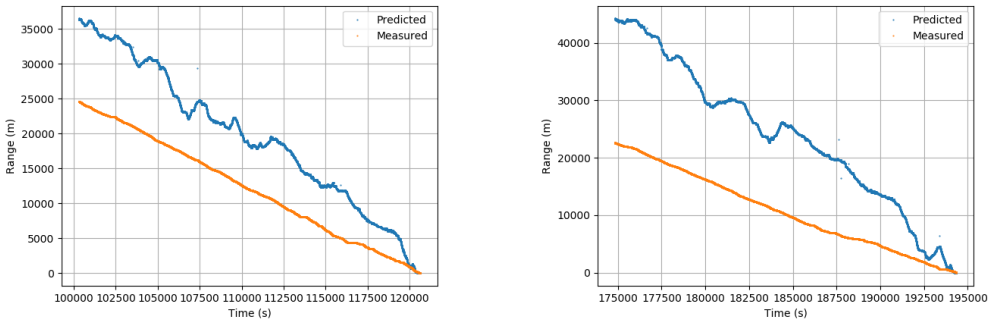

(a) Day 5 (b) Day 9

Figure 6.2: Examples of range predictions and measurements without calibration.

the trips[1] collected the distance travelled (Δs_{trip}) and the range variation ($\Delta RDR_{trip} = RDR_i - RDR_f$) from start to end. This calibration factor is then estimated as the expected slope of equation 6.4, which is calculated using a linear regression.

In figure 6.3 there can be seen an example of a calibration. In figure 6.4 there can be seen the same trip predictions as in figure 6.2, but now considering considering the range estimation with calibration (equation 6.4). Further analysis will be provided in the following sections, with and without the calibration.

$$\Delta RDR_{trip} = f_{cal} \cdot \Delta s_{trip} \tag{6.4}$$

$$RDR_i = \frac{SOC_i}{\bar{p}_i} \cdot f_{cal} \tag{6.5}$$

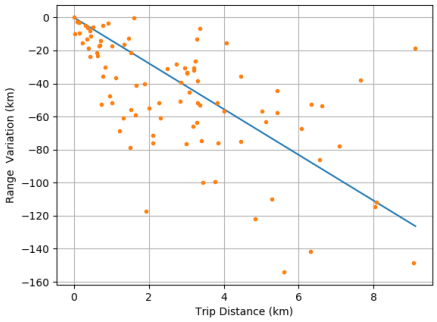

Figure 6.3: Example of a graph of the calibration

6.4 Time Window

The commonly used moving average usually considers a constant time window. In other words the average is taken in the values inside a constant time window to the past. For example, a time window of 10 min. would average the values of the last 10 min. of acquisition. As the sampling frequency is

[1] As seen before in chapter 3 a trip of the vehicle run from the moment the moment the vehicle is turned on until it is turned off.

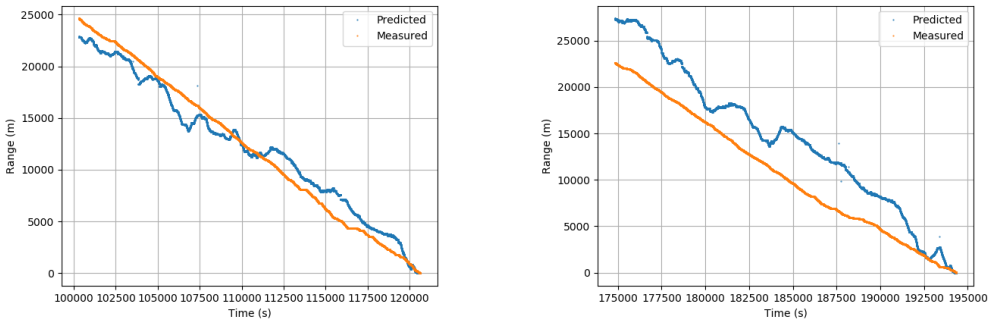

(a) Day 5

(b) Day 9

Figure 6.4: Examples of preliminary range predictions and measurements.

constant, it is an average of the last N values, where N is a constant given by $N = \frac{t_w}{T_s}$, where t_w is the time window and T_s is the sampling period.

For the constant time window, the average consumption per distance ($\bar{p}_i$) travelled can, then, be calculated using equation 6.6. The numerator is the current integral estimation and the denominator is the distance travelled during that window.

$$\bar{p}_i = \frac{T_s \cdot \sum_{k=i-N}^{i} I_i}{\sum_{k=i-N}^{i-1} \Delta s_i} \tag{6.6}$$

The remaining driving range (RDR_i) was calculated with and without using the calibration factor, as shown in equations 6.5 and 6.3, respectively. The computation of the calibration factor was described in section 6.3.

In figure 6.5 it can be seen the estimated consumption per kilometre over time, for two different moving average windows. It is possible to see that as the window increases in size, the average consumption becomes more stable, as one should expect. The delay factor was not as relevant because of the regenerative braking in the series contributing with negative values to the moving average. Another important factor is that is tends to stabilize on the value $5A \cdot s/m$, which coresponds to $13.8kWh/100km$. This value is consistent with the average consumption of $A = 1.85Ah/km = 14.2Wh/100km$ found in section 3.1.1. The average consumption expected for the average EV was found to be around $17kWh/100km$ in a comparative study [60]. However, this study focused on standard road vehicles and the consumption is expected to be smaller in powered light vehicles, given its lower velocities and mass.

6.4.1 Model Evaluation

In the trip based methods described in chapter 5, it was possible to use the entire dataset for the evaluation because in that case the predictions were not dependent in the chronological order of the values. However, for the present method, that is pretty much not the case, because the prediction is dependent on the moving average of the previously measured values. Because of this, the predictions have to be evaluated in the context of an evolving series of data points.

Therefore, to accurately test the range measurement we have to choose segments of length com-

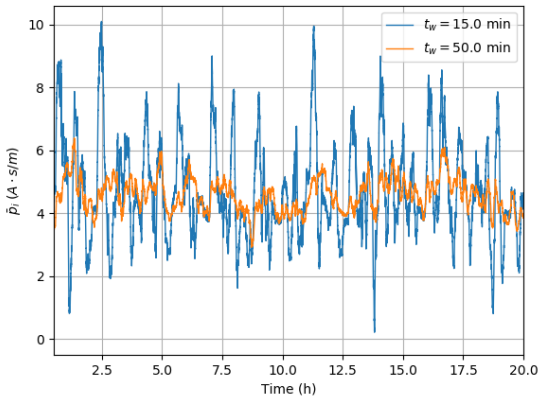

Figure 6.5: Consumption values for different moving average windows.

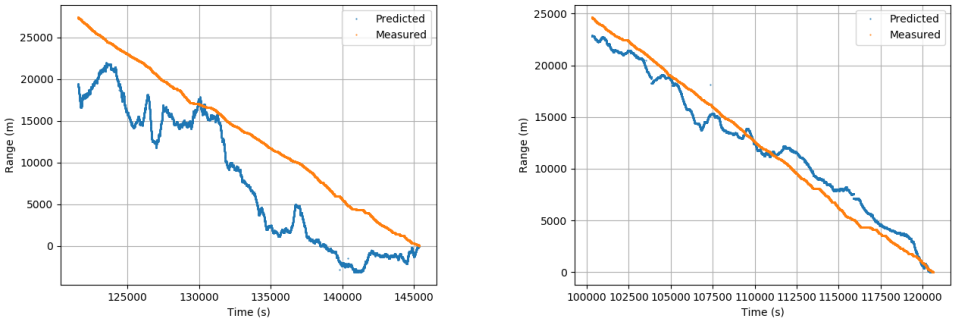

(a) $R^2 = 0.41$, error = 30 %, $t_w = 50min$

(b) $R^2 = 0.96$, error = 7%, $t_w = 8:20h$

Figure 6.6: Examples of the range prediction profile for two different time windows.

parable with the vehicle range to guarantee that the prediction remains valid for enough time. The segments used contain all the data acquired for a given day, from the moment the vehicle leaves the garage, fully charged until the moment it is charged again at the end of the day.

For each of this segments, the R^2 (computed as described in section 5.1) between the range prediction and the measured range is determined. The measured range was computed for each trip as shown in equation 6.7, where Δs_{tot} is the total distance travelled in the whole trip and Δs_i is the distance travelled from the beginning of the trip until the point i. This was done for different moving average window values. In figure 6.8 there can be seen the range prediction for the same day and for two different time windows. As expected, the curve becomes smoother as the time window increases, and the predicted values become closer to the measured, which is reflected in both a smaller relative error and R^2 closer to one.

$$RDR_{meas_i} = \Delta s_{tot} - \Delta s_i \tag{6.7}$$

The range prediction was made over all the charging cycles that were acquired for varying time windows. The average value of R^2 obtained can be seen in figure 6.7 as a function of the time window considered. It is possible to see that for the points **with calibration** the R^2 approaches 1 for windows

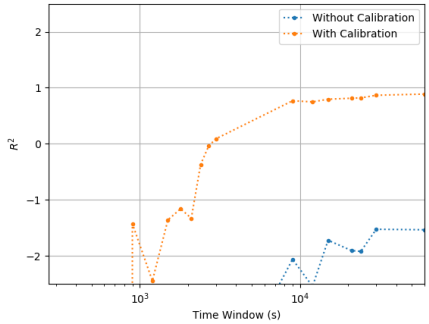

Figure 6.7: Evolution of the R^2 as a function of the window used.

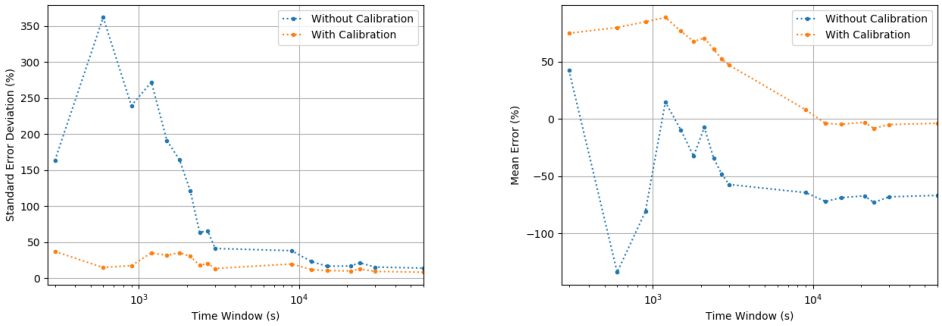

(a) Standard Deviation of error

(b) Mean of Error

Figure 6.8: Values of the mean error and standard deviation of the error values for various time windows.

above 10000 s (around 2:45 h), which indicates that this is the minimum value for a correct description of the measured data. On the other hand, for the predictions **without calibration** the value of R^2 stabilizes in a negative values. This happens because of the large error present, in this cases.

For the cycles it was also determined the relative error of the prediction using equation 6.8. This metric was used in other works [61] and represents relative error between the value of range that was used and the distance that the vehicle actually travelled.

$$e = \frac{\Delta RDR - \Delta s}{\Delta s} \tag{6.8}$$

From the values of errors for the charging cycles, it was computed the average error and the standard deviation of the values. In figure 6.8 it can be seen the evolution of the average error as well as the evolution of the standard deviation of the errors. As seen before the values tend to stabilise for bigger time windows, as the bigger the window the less the values will vary.

It can also be seen that the calibrated points perform much better. For larger windows the average error approaches zero, while this does not happen for the non-calibrated values. The standard deviation of the values is also closer to zero for the calibrated model than it is for the non-calibrated model. From this we can conclude that the calibrated model is both more exact and more precise.

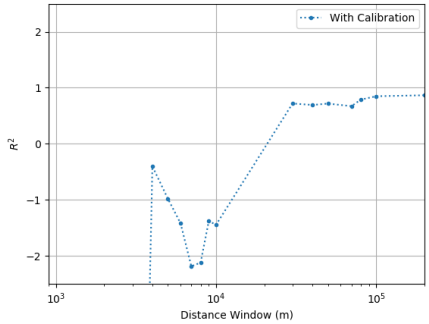

Figure 6.9: Evolution of the R^2 values for the constant distance window moving average as a function of the window considered.

6.5 Distance Window

Another way of choosing a value window can be by using a constant distance window, in stead of a constant time window. This is to say, for example, in stead of looking at the data in the last 10 min., we will look at the data for the last 10 km. This is commonly used when building range estimators. When making this type of prediction, the number of points in the moving average window is going to change as the time moves forward. This window is determined so that the condition in equation 6.9 is obeyed, where d_w is the distance window that is considered. The estimation is now determined by the equation 6.10, which is the same as previously, only now the N is not constant.

$$\sum_{i=t-N_t}^{t} \Delta s_i \approx d_w \tag{6.9}$$

$$\bar{p_i} = \frac{T_s \cdot \sum_{k=i-N_t}^{i} I_i}{\sum_{k=i-N_t}^{i-1} \Delta s_i} \tag{6.10}$$

The evaluation of the model was made in the same way as for the **time window** models. For this model, the results also improved upon calibration. Because of this the data presented corresponds only to calibrated data. In figure 6.9 it can be seen that the value of R^2 once again stabilizes close to one for widows above 30 kilometres. However, as can be seen in figure 6.10 the average error is still considerable and only becomes close to zero for windows of around 80 km. For these bigger windows, it can be seen that the standard deviation of the error is close to 10%, which is a acceptable value.

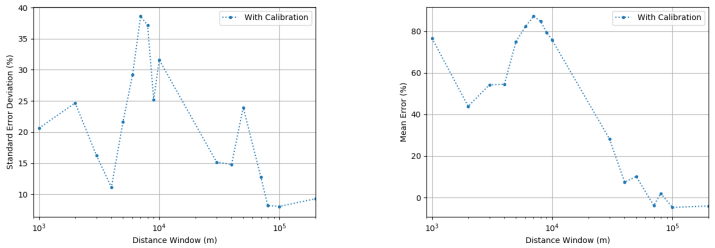

(a) Standard Deviation of error (b) Mean of Error

Figure 6.10: Examples of the range prediction profile for two different time windows.

6.6 Model Comparison

The objective of this section was to determine which of the ways of choosing the window produced the best results for this real time methods. We make this by comparing the best results obtained with the **constant time window** to the best ones obtained using the **constant distance window**. Table 6.1 shows the R^2 average and standard deviation for both models. It is verified that both values are relatively close to one another. Both present an acceptable fit to the measured data and the results show consistency across the different days considered, showing a relatively low standard deviation. In table 6.2 it can be seen the mean and the standard deviation of the relative error for the cycles considered. It can be seen that the distance window method showed itself to be more accurate with a lower average error, as well as more precise with a lower error standard deviation.

Overall we have similar results for both methods, but the **distance window** method proved to be slightly more accurate and precise.

Window	**Mean** R^2	**Standard** R^2 **Deviation**
$t_w = 2:45min$	0.77	0.13
$d_w = 80km$	0.79	0.18

Table 6.1: Mean and Standard Deviation of the R^2.

Window	**Mean Error** (%)	**Standard Error Deviation** (%)
$t_w = 2:45min$	8.1	19.7
$d_w = 80km$	2.0	8.2

Table 6.2: Mean and Standard Deviation of the relative error.

Chapter 7

Conclusions

This last section sums up the work of this master thesis project, summarising the main results and achievements as well as analysing what could be improved and several ways to extend the scope of the project.

7.1 Achievements

As discussed previously it is possible to divide the work of this thesis in three main parts. In the first part, it was successfully converted the battery pack of the *e-tuk* Limo GT from the original lead-acid batteries to a new $LiFePO_4$ lithium-ion pack. In order to do this, a new battery compartment was designed to hold the now smaller and lighter batteries in place. After the battery pack conversion, it was achieved a increase of 25% in the vehicle range, relatively to the range provided by the manufacturer. It is also expected the increase in the durability of the batteries to 2000 cycles in stead of the previous 600, which corresponds to a 230% increase in durability.

In the second part of this work, a data acquisition system was successfully developed and tested to log the geographical position of the vehicle as well as information concerning the battery pack. The geographical information contained latitude and longitude of the vehicle vehicle as well as the velocity of the vehicle. The battery information contained the battery pack voltage, current, SOC, power etc.. This system was done using a *Raspberry Pi* connected to a GPS receiver and also to the BMS through serial communication. The set-up was successfully tested using a **e-max** motorcycle and successfully adapted to fit the new battery pack of the *e-tuk*. The software used to make the data acquisition was developed in *Python* using one individual class for each acquisition. It was also implemented a webpage hosted in the *Raspberry Pi* to read the last point recorded without need for connection via SSH.

In the third part the data collected was used to test methods of eliminating range anxiety. Two different types of methods were successfully implemented: the trip-based methods and the history-based methods. The first predict the energy consumption for known vehicle trip, and the second are used to estimate the full remaining driving range of the vehicle from the consumption history. The trip-based methods implemented make use of both physical and statistical models to predict the energy

Model	Average Error (%)	Standard Deviation (%)
Regression Model	3	13
A priori Model	-32	27
KNN	7	52
Decision Trees	1	26

Table 7.1: Average and standard deviation of the error values for the different methods.

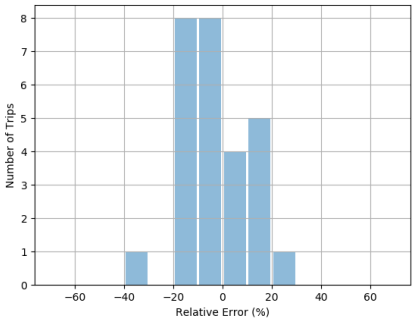

Figure 7.1: Relative error distribution for trips with $\Delta E > 1AH$. Average error was -3% and the standard deviation 13%

consumption.

For all the models it was shown an overall performance improvement as the duration of the trip segments increase. In table 7.1, it can be seen the main results for the trip-based predictions for segments of duration of 150s. The method that provided the best results overall was the regression model having the lower error standard deviation. It was concluded that the best performance was provided by the regression model. In [33], where a similar study was done, obtained $R^2 = 0.968$, which was generally higher than the one obtained of 0.840. For energy consumptions comparable to the considered in this study, the errors obtained in [33] are up to 15%, which is comparable with the predictions made in this thesis, as shown in figure 7.1. The results are then expected to improve as the data sample gets bigger, compared with the one used for this study.

Due to the fact that the altitude estimations were not reliable, the road slope estimations were not reliable. Because of this, it was not possible to accurately predict the instantaneous consumption of the vehicle, making the introduction of the efficiency of the electric motor impossible. However it was successfully extracted a efficiency map of the vehicle.

Two different formulations of history-based were also implemented using methods based on the moving average algorithm. These two differ in the way that the moving average was chosen. The first method considered a constant time window and the second a constant distance window. In table 7.2 can be seen the two best values obtained with each of the ways of choosing the window.

Window	Mean Error (%)	Standard Error Deviation (%)
$t_w = 2:45min$	8.1	19.7
$d_w = 80km$	2.0	8.2

Table 7.2: Mean and Standard Deviation of the relative error.

In [61] is shown a study of a commercial **history-based** range prediction system in the 2011 Nissan

Leaf. It showed relative errors above 50% for distances comparable with the ones considered in this study (around 50 km). For this particular case, the method implemented showed better results than the commercial.

7.2 Future Work

There are several ways to extend the scope of the present work in each of its parts. Starting on the vehicle, the *e-tuk* itself can be improved by adding the possibility for the vehicle to be charged during movement with the addition of a solar panel. This addition will reduce the dependence of the vehicle on the grid and also extend the vehicle range beyond the charge of the batteries. This addition would affect the range prediction of the vehicle would have to be updated in order to estimate not only the vehicle consumption but also the energy that is charged using the solar panel.

In the second part of the work, the most important way of improving the data acquisition system in order to better the quality of the data collected would be the change of the GPS receiver. With a GPS receiver capable of accurately measuring the altitude of the vehicle, it would be possible to estimate the road slope correctly, allowing the introduction of the motor efficiency in the energy consumption predictions. Another way of doing this would be by introducing an inclinometer in the vehicle to directly measure its angle.

Another logical step to take is to add internet connection to the system. This would allow the access to the state of the vehicle at all times and allow a better management. The internet connection enables the integration of the system with *GoogleMaps API*. This in turn allows the access to traffic data as well as directions to the destination in real time as done in [29]. Adding a screen connection to the raspberry it would then be possible to use the *Raspberry Pi* system as a on-board computer, which could provide trip planning and implement the trip-based methods, whose implementation was proved possible in this work. In addition to this, the connection of the *Raspberry* to the controller would allow for the remote access to the vehicle controller. This would add the ability to troubleshoot the vehicle while in driving, without the need for the vehicle to be taken to the shop immediately.

In the models implemented there are some improvements possible. To improve the physical models used in the trip-based methods, it is possible to add the experimental tests to the vehicle to estimate the model parameters. It is also possible to measure experimentally the efficiency map of the motor and use it to make the predictions of the consumption instead of having to estimate this map. To improve the statistical models, the size of the dataset should be increased in order to have more significant training set. In this larger dataset other improved methods such as neural networks can be implemented.

Bibliography

[1] European Comission. Roadmap to a Single Europoean Transport Area - Towards a competitive and resource efficient system. 2011. URL https://ec.europa.eu/transport/themes/strategies/2011{_}white{_}paper{_}en.

[2] International Energy Agency. Global EV Outlook 2020, 2020. URL https://www.iea.org/reports/global-ev-outlook-2020.

[3] A. C. Silva. Visão Estratégica para o Plano de Recuperação Económica de Portugal. Technical report, 2020.

[4] Automotive European Manufacturers Association. The Automobile Industry Pocket Guide 2020-2021. Technical report, 2020.

[5] M. Woodward, D. B. Walton, D. J. Hamilton, G. Alberts, S. Fullerton-Smith, E. Day, and J. Ringrow. Electric vehicles: Setting a course for 2030. Technical report, 2020. URL https://www2.deloitte.com/uk/en/insights/focus/future-of-mobility/electric-vehicle-trends-2030.html.

[6] Motorcycle Industry Association. L-Category Vehicles: Examples & Definitions. (June), 2019.

[7] Instituto da Mobilidade e Trasportes I.P. Homologação de Veículos. URL http://www.imt-ip.pt/sites/IMTT/Portugues/Veiculos/Aprovacoes/HomologacoesVeiculos/Paginas/HomologacaoVeiculos.aspx.

[8] V. D. Truong, X. Liu, and Q. Pham. To be or not to be formal? Rickshaw drivers' perspectives on tourism and poverty. *Journal of Sustainable Tourism*, 28(1):33–50, 2020. doi: 10.1080/09669582.2019.1665056. URL https://doi.org/10.1080/09669582.2019.1665056.

[9] K. S. Reddy, S. Aravindhan, and T. K. Mallick. Techno-economic investigation of solar powered electric auto-rickshaw for a sustainable transport system. *Energies*, 10(6):1–15, 2017. doi: 10.3390/en10060754.

[10] F. A. Sell. O Universo tuk tuk em Lisboa: territorialidades, "drivers" e consumidores. Technical report, 2019.

[11] C. Chaiyamanon, A. Sripakagorn, and N. Noomwongs. Dynamic modeling of electric tuk-tuk for predicting energy consumption in bangkok driving condition. *SAE Technical Papers*, 1, 2013. ISSN 26883627. doi: 10.4271/2013-01-0113.

[12] C. Cochrane, T. Muneer, and B. Fraser. Design of an Electrically Powered Rickshaw, for Use in India. *Energies*, 12(17):3346, aug 2019. ISSN 1996-1073. doi: 10.3390/en12173346. URL https://www.mdpi.com/1996-1073/12/17/3346.

[13] Deloitte. 2018 Deloitte Global Automotive Consumer Study. pages 1–47, 2018.

[14] M. Singer. Consumer Views on Plug-in Electric Vehicles – National Benchmark Report. (January): 38, 2016.

[15] C. King, W. Griggs, F. Wirth, K. Quinn, and R. Shorten. Alleviating a form of electric vehicle range anxiety through on-demand vehicle access. *International Journal of Control*, 88(4):717–728, 2015. doi: 10.1080/00207179.2014.971521.

[16] G. Pasaoglu, D. Fiorello, A. Martino, L. Zani, A. Zubaryeva, and C. Thiel. Travel patterns and the potential use of electric cars - Results from a direct survey in six European countries. *Technological Forecasting and Social Change*, 87:51–59, 2014. ISSN 00401625. doi: 10.1016/j.techfore.2013.10.018.

[17] N. S. Pearre, W. Kempton, R. L. Guensler, and V. V. Elango. Electric vehicles: How much range is required for a day's driving? *Transportation Research Part C: Emerging Technologies*, 19(6): 1171–1184, 2011. doi: 10.1016/j.trc.2010.12.010.

[18] T. Franke and J. F. Krems. Interacting with limited mobility resources: Psychological range levels in electric vehicle use. *Transportation Research Part A: Policy and Practice*, 48:109–122, 2013. ISSN 09658564. doi: 10.1016/j.tra.2012.10.010.

[19] M. Nilsson. Electric Vehicle: A range anxiety interview study. (November), 2011.

[20] A. Enthaler and F. Gauterin. Method for reducing uncertainties of predictive range estimation algorithms in electric vehicles. *2015 IEEE 82nd Vehicular Technology Conference, VTC Fall 2015 - Proceedings*, pages 1–5, 2016. doi: 10.1109/VTCFall.2015.7391023.

[21] J. Hong, S. Park, and N. Chang. Accurate remaining range estimation for Electric vehicles. *Proceedings of the Asia and South Pacific Design Automation Conference, ASP-DAC*, 25-28-Janu: 781–786, 2016. doi: 10.1109/ASPDAC.2016.7428106.

[22] C. Moure, M. Roche, and M. Mammetti. Range estimator for electric vehicles. *2013 World Electric Vehicle Symposium and Exhibition, EVS 2014*, pages 1–15, 2014. doi: 10.1109/EVS.2013.6914917.

[23] N. Denis, M. R. Dubois, K. A. Gil, T. Driant, and A. Desrochers. Range prediction for a three-wheel plug-in hybrid electric vehicle. *2012 IEEE Transportation Electrification Conference and Expo, ITEC 2012*, pages 1–6, 2012. doi: 10.1109/ITEC.2012.6243415.

[24] J. A. Oliva, C. Weihrauch, and T. Bertram. Model-based remaining driving range prediction in electric vehicles by using particle filtering and Markov chains. *2013 World Electric Vehicle Symposium and Exhibition, EVS 2014*, pages 1–10, 2014. doi: 10.1109/EVS.2013.6914989.

[25] Z. Yi and P. H. Bauer. Adaptive Multiresolution Energy Consumption Prediction for Electric Vehicles. *IEEE Transactions on Vehicular Technology*, 66(11):10515–10525, 2017. ISSN 00189545. doi: 10.1109/TVT.2017.2720587.

[26] K. S. Grewal and P. M. Darnell. Model-based EV range prediction for electric hybrid vehicles. *IET Conference Publications*, 2013(621 CP):1–6, 2013. doi: 10.1049/cp.2013.1895.

[27] T. S. Kim, C. Manzie, and R. Sharma. Model predictive control of velocity and torque split in a parallel hybrid vehicle. *Conference Proceedings - IEEE International Conference on Systems, Man and Cybernetics*, (October 2009):2014–2019, 2009. ISSN 1062922X. doi: 10.1109/ICSMC.2009.5346115.

[28] T. Liu, X. Hu, S. E. Li, and D. Cao. Reinforcement Learning Optimized Look-Ahead Energy Management of a Parallel Hybrid Electric Vehicle. *IEEE/ASME Transactions on Mechatronics*, 22(4):1497–1507, 2017. ISSN 10834435. doi: 10.1109/TMECH.2017.2707338.

[29] F. Foiadelli, M. Longo, and S. Miraftabzadeh. Energy Consumption Prediction of Electric Vehicles Based on Big Data Approach. *Proceedings - 2018 IEEE International Conference on Environment and Electrical Engineering and 2018 IEEE Industrial and Commercial Power Systems Europe, EEEIC/I and CPS Europe 2018*, pages 1–6, 2018. doi: 10.1109/EEEIC.2018.8494573.

[30] L. Bedogni, L. Bononi, A. D. Elia, M. D. Felice, M. D. Nicola, and T. S. Cinotti. Driving Without Anxiety : a Route Planner Service with Range Prediction for the Electric Vehicles. *2014 International Conference on Connected Vehicles and Expo (ICCVE)*, pages 199–206, 2014. doi: 10.1109/ICCVE.2014.7297541.

[31] C. Moure, M. Roche, and M. Mammetti. Range estimator for electric vehicles. *2013 World Electric Vehicle Symposium and Exhibition, EVS 2014*, pages 1–15, 2014. doi: 10.1109/EVS.2013.6914917.

[32] D. Baek, Y. Chen, A. Bocca, L. Bottaccioli, S. D. Cataldo, V. Gatteschi, D. J. Pagliari, E. Patti, G. Urgese, N. Chang, A. Macii, E. Macii, P. Montuschi, and M. Poncino. Battery-Aware operation range estimation for terrestrial and aerial electric vehicles. *IEEE Transactions on Vehicular Technology*, 68(6):5471–5482, 2019. ISSN 19399359. doi: 10.1109/TVT.2019.2910452.

[33] C. De Cauwer, M. Messagie, S. Heyvaert, T. Coosemans, and J. Van Mierlo. Electric vehicle use and energy consumption based on real world electric vehicle fleet trip and charge data its impact on existing EV research models. *World Electric Vehicle Journal*, 7(3):436–446, 2015. ISSN 20326653. doi: 10.3390/wevj7030436.

[34] F. Badin, F. Le Berr, H. Briki, J. C. Dabadie, M. Petit, S. Magand, and E. Condemine. Evaluation of EVs energy consumption influencing factors: Driving conditions, auxiliaries use, driver's aggressiveness. *World Electric Vehicle Journal*, 6(1):112–123, 2013. ISSN 20326653. doi: 10.3390/wevj6010112.

[35] J. C. Ferreira, V. Monteiro, and J. L. Afonso. Dynamic range prediction for an electric vehicle. *2013 World Electric Vehicle Symposium and Exhibition, EVS 2014*, pages 1–11, 2014. doi: 10.1109/EVS.2013.6914832.

[36] W. Dib, A. Chasse, P. Moulin, A. Sciarretta, and G. Corde. Optimal energy management for an electric vehicle in eco-driving applications. *Control Engineering Practice*, 29:299–307, 2014. ISSN 09670661. doi: 10.1016/j.conengprac.2014.01.005.

[37] N. Jinil and S. Reka. Deep Learning method to predict Electric Vehicle power requirements and optimizing power distribution. *5th International Conference on Electrical Energy Systems, ICEES 2019*, pages 1–5, 2019. doi: 10.1109/ICEES.2019.8719243.

[38] C. Simonis and R. Sennefelder. Route specific driver characterization for data-based range prediction of battery electric vehicles. *2019 14th International Conference on Ecological Vehicles and Renewable Energies, EVER 2019*, pages 1–6, 2019. doi: 10.1109/EVER.2019.8813579.

[39] K. Gebhardt, V. Schau, and W. R. Rossak. Applying stochastic methods for range prediction in E-mobility. *2015 15th International Conference on Innovations for Community Services, I4CS 2015*, pages 1–4, 2015. doi: 10.1109/I4CS.2015.7294483.

[40] P. Ondruska and I. Posner. Probabilistic attainability maps: Efficiently predicting driver-specific electric vehicle range. In *IEEE Intelligent Vehicles Symposium, Proceedings*, number Iv, pages 1169–1174. IEEE, 2014. ISBN 9781479936380. doi: 10.1109/IVS.2014.6856572.

[41] J. Dedek, T. Docekal, S. Ozana, and T. Sikora. BEV Remaining Range Estimation Based on Modern Control Theory - Initial Study. *IFAC-PapersOnLine*, 52(27):86–91, 2019. ISSN 24058963. doi: 10.1016/j.ifacol.2019.12.738.

[42] L. Rodgers, D. Frey, and E. Wilhelm. Estimating an Electric Vehicle's "Distance to Empty" Using Both Past and Future Route Information. In *Proceding ASME 2013 international Design Engineering Technical Conferences and Computers and Information in Engineering Conference*, pages 1–9. American Society of Mechanical Engineers, aug 2013. ISBN 978-0-7918-5584-3. doi: 10.1115/DETC2013-12880.

[43] A. Bolovinou, I. Bakas, A. Amditis, F. Mastrandrea, and W. Vinciotti. Online prediction of an electric vehicle remaining range based on regression analysis. *2014 IEEE International Electric Vehicle Conference, IEVC 2014*, pages 1–8, 2014. doi: 10.1109/IEVC.2014.7056167.

[44] L. Guzzella and A. Sciarretta. *Vehicle Propulsion Systems: Introduction to Modelling and Optimization*. Springer Berlin Heidelberg New York, 2013. ISBN 9783540251958.

[45] D. D. Thomas Gillespie. *Fundamentals of Vehicle Dynamics*. SAE International. ISBN 978-1-56091-199-9.

[46] F. M. White. *Fluid Mechanics*. 4th edition, 2001.

[47] T. Selten. Stella Lux: the energy-positive family car. *Europhysics News*, 48(3):13–16, may 2017. ISSN 0531-7479. doi: 10.1051/epn/2017301. URL http://www.europhysicsnews.org/10.1051/epn/2017301.

[48] A. D. Gordon, L. Breiman, J. H. Friedman, R. A. Olshen, and C. J. Stone. Classification and Regression Trees. *Biometrics*, 40(3):874, sep 1984. ISSN 0006341X. doi: 10.2307/2530946. URL https://www.jstor.org/stable/2530946?origin=crossref.

[49] T. Hastie, R. Tibshirani, and J. Friedman. *The Elements of Statistical Learning*. Springer Series in Statistics. Springer New York, New York, NY, 2009. ISBN 978-0-387-84857-0. doi: 10.1007/978-0-387-84858-7. URL http://link.springer.com/10.1007/978-0-387-84858-7.

[50] E-Tuk Factory. e-Tuk Limo GT Brochure, 2020. URL https://etukfactory.com/limo.

[51] E. S. Raymond. GPSD Client HOWTO. URL https://gpsd.gitlab.io/gpsd/client-howto.html.

[52] Trojan T-105 Batteries Documentation. URL http://www.trojanbattery.com/pdf/datasheets/T105{_}Trojan{_}Data{_}Sheets.pdf.

[53] CALB 180AH LiFePO4 Battery Datasheet. URL https://shop.gwl.eu/index.php?cur=1{&}cl=details{_}disc{&}anid=2946{#}tab3.

[54] M. Ehsani, Y. Gao, S. Longo, and K. Ebrahimi. *Modern Electric, Hybrid Electric, and Fuel Cell Vehicles, Third Edition*. CRC Press, New York, NY, 2018. ISBN 9780429504884. doi: 10.1201/9780429504884.

[55] G. Chen and T. J. Richardson. Thermal instability of Olivine-type LiMnPO4 cathodes. *Journal of Power Sources*, 195(4):1221–1224, 2010. ISSN 03787753. doi: 10.1016/j.jpowsour.2009.08.046.

[56] C. De Cauwer, J. Van Mierlo, and T. Coosemans. Energy consumption prediction for electric vehicles based on real-world data. *Energies*, 8(8):8573–8593, 2015. ISSN 19961073. doi: 10.3390/en8088573.

[57] R. H. Shumway and D. S. Stoffer. *Time Series Analysis and Its Applications*. Springer Texts in Statistics. Springer New York, New York, NY, october 20 edition, 2011. ISBN 978-1-4419-7864-6. doi: 10.1007/978-1-4419-7865-3.

[58] D. Ruppert. *Statistics and Data Analysis for Financial Engineering*. Springer Texts in Statistics. Springer New York, New York, NY, 2011. ISBN 978-1-4419-7786-1. doi: 10.1007/978-1-4419-7787-8.

[59] Y. Chou. *Statistical Analysis for Business and Economic Applications*. Holt Rinehart and Winston, 1963. URL https://books.google.pt/books?id=NPV9tAEACAAJ.

[60] D. A. Howey, R. F. Martinez-Botas, B. Cussons, and L. Lytton. Comparative measurements of the energy consumption of 51 electric, hybrid and internal combustion engine vehicles. *Transportation*

Research Part D: Transport and Environment, 16(6):459–464, 2011. ISSN 13619209. doi: 10.1016/j.trd.2011.04.001.

[61] S. A. Birrell, A. McGordon, and P. A. Jennings. Defining the accuracy of real-world range estimations of an electric vehicle. *2014 17th IEEE International Conference on Intelligent Transportation Systems, ITSC 2014*, pages 2590–2595, 2014. doi: 10.1109/ITSC.2014.6958105.

Appendix A

Controller Configuration

Name	Value
Nominal Voltage	78.5 V
Under-voltage	2 V
User Overvoltage	115 %
User Undervoltage	80 %
Reset Volts p/cell	2.04 V
Empty Volts p/cell	1.73 V
Discharge Time	70 min
BDI Reset percent	100 %

Table A.1: Battery Menu controller parameters

Name	Value
Drive Current	100 %
Regen Current	100 %
Brake Current	100 %
EMR Current Limit	100 %
Interlock Brake	100 %

Table A.2: Current Limits controller parameters

Name	Value
Type	2
Foward Deadband	1 V
Foward Map	15 %
Foward Max	4.5
Foward Offset	0 %
Reverse Deadband	1V
Reverse Map	4.5V
Reverse Max	4.5V
Reverse Offset	0
HPD/SRO Type	1
Sequencing Delay	0.1
VCL Throttle Enable	OFF

Table A.3: Throttle Configurations controller parameters

Name	Value
Brake Pedal Enable	ON
Brake Type	5
Brake Deadband	0.5V
Brake Map	50 %
Brake Max	4.5
Brake Offset	0 %
Brake Filter	0
VCL Brake Enable	OFF

Table A.4: Brake Configurations controller parameters

Appendix B

Data Format

Label App	Label	Byte Location	Units
Voltage 1	V_TOT	04-05	10 $\times$ Volt
Voltage 17	V_CELL_01	06-07	10^3 $\times$ Volt
Voltage 18	V_CELL_02	08-09	10^3 $\times$ Volt
Voltage 19	V_CELL_03	10-11	10^3 $\times$ Volt
Voltage 20	V_CELL_04	12-13	10^3 $\times$ Volt
Voltage 21	V_CELL_05	14-15	10^3 $\times$ Volt
Voltage 22	V_CELL_06	16-17	10^3 $\times$ Volt
Voltage 23	V_CELL_07	18-19	10^3 $\times$ Volt
Voltage 24	V_CELL_08	20-21	10^3 $\times$ Volt
Voltage 25	V_CELL_09	22-23	10^3 $\times$ Volt
Voltage 26	V_CELL_10	24-25	10^3 $\times$ Volt
Voltage 27	V_CELL_11	26-27	10^3 $\times$ Volt
Voltage 28	V_CELL_12	28-29	10^3 $\times$ Volt
Voltage 29	V_CELL_13	30-31	10^3 $\times$ Volt
Voltage 30	V_CELL_14	32-33	10^3 $\times$ Volt
Voltage 31	V_CELL_15	34-35	10^3 $\times$ Volt
Voltage 32	V_CELL_16	36-37	10^3 $\times$ Volt
Voltage 33	V_CELL_17	38-39	10^3 $\times$ Volt
Voltage 34	V_CELL_18	40-41	10^3 $\times$ Volt
Voltage 35	V_CELL_19	42-43	10^3 $\times$ Volt
Voltage 36	V_CELL_20	44-45	10^3 $\times$ Volt
Voltage 37	V_CELL_21	46-47	10^3 $\times$ Volt
Voltage 38	V_CELL_22	48-49	10^3 $\times$ Volt
Voltage 39	V_CELL_23	50-51	10^3 $\times$ Volt
Voltage 40	V_CELL_24	52-53	10^3 $\times$ Volt
Voltage 41	V_CELL_25	54-55	10^3 $\times$ Volt
Voltage 42	V_CELL_26	56-57	10^3 $\times$ Volt
Voltage 44	V_CELL_27	58-59	10^3 $\times$ Volt
Voltage 45	V_CELL_28	60-61	10^3 $\times$ Volt
Voltage 46	V_CELL_29	62-63	10^3 $\times$ Volt
Voltage 47	V_CELL_30	64-65	10^3 $\times$ Volt
Voltage 48	V_CELL_31	66-67	10^3 $\times$ Volt
Voltage 49	V_CELL_32	68-69	10^3 $\times$ Volt
Voltage 50	V_CELL_33	70-71	10^3 $\times$ Volt
Voltage 02	I_TOT	72-73	10$\times$ Volt
Voltage 04	SOC_%	74	percent (%)
Voltage 03	SOC(AH)	79-82	$10^6\times$ (AH)
Voltage 11	T1	91-92	Degree
Voltage 12	T2	93-94	Degree
Voltage 13	T3	95-96	Degree
Voltage 14	T4	97-98	Degree
Voltage 15	T5	99-100	Degree
Voltage 16	T6	101-102	Degree
Voltage 06	POWER	113-114	Watt (W)
-	N_CELL_MAX	115	Number
Voltage 07	V_CELL_MAX	116-117	10^3 $\times$ Volt
-	N_CELL_MIN	118	Number
Voltage 08	V_CELL_MIN	119-120	10^3 $\times$ Volt
Voltage 09	V_CELL_AVG	121-122	10^3 $\times$ Volt
-	N_CELLS	123	Number

Table B.1: Table containing the decoding of the serial communication protocol of the BMS. The **Byte Nr** stats at zero.

Appendix C

Technical Drawings

C.1 Batteries

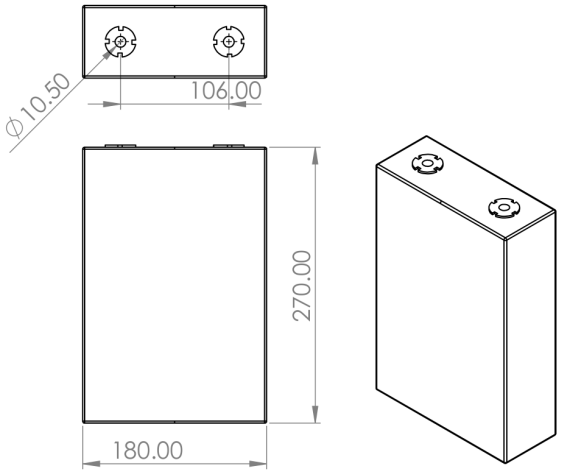

Figure C.1: Technical drawings concerning the batteries used in this work.

C.2 Connectors

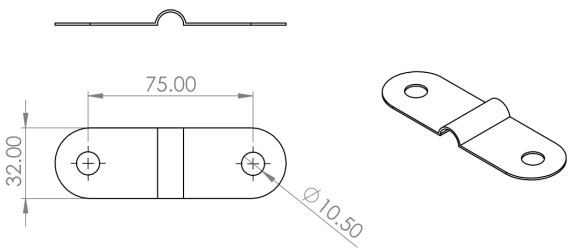

Figure C.2: Technical drawings concerning the horizontal connector.

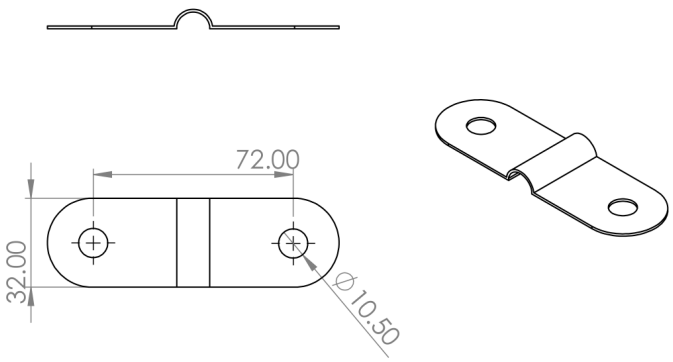

Figure C.3: Technical drawings concerning the vertical connector.

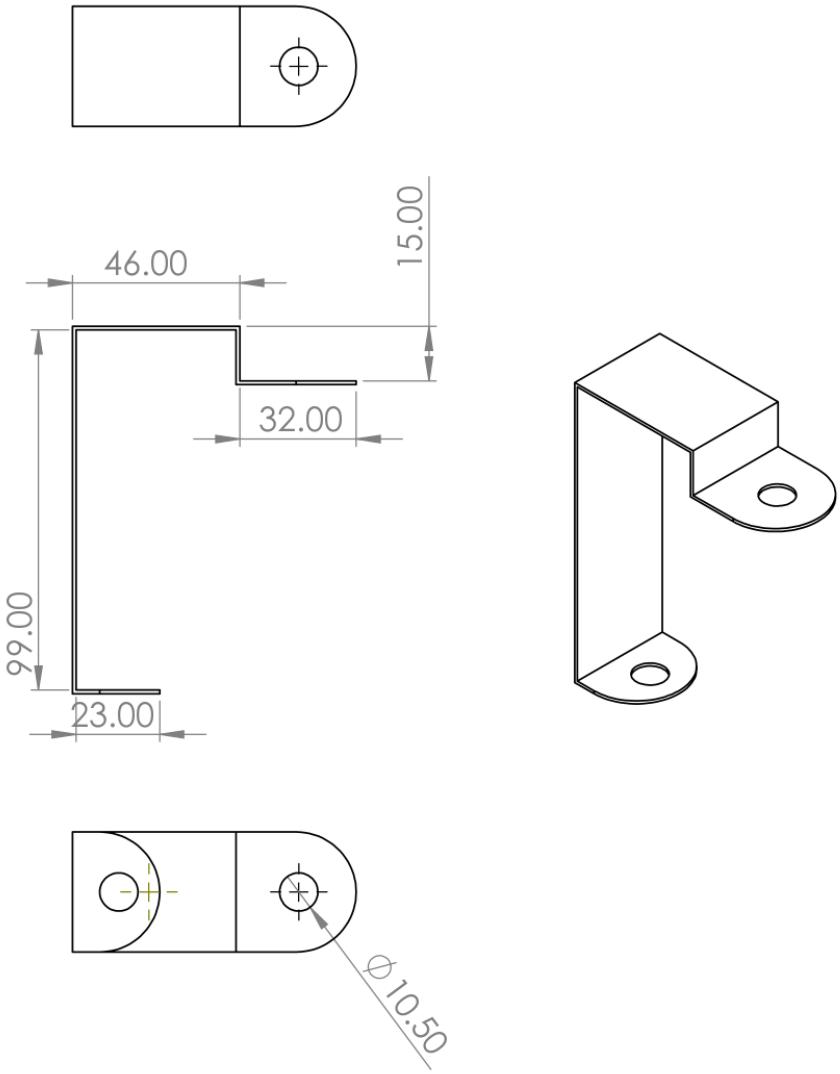

Figure C.4: Technical drawings concerning the fuse connector.

C.3 Battery Compartment

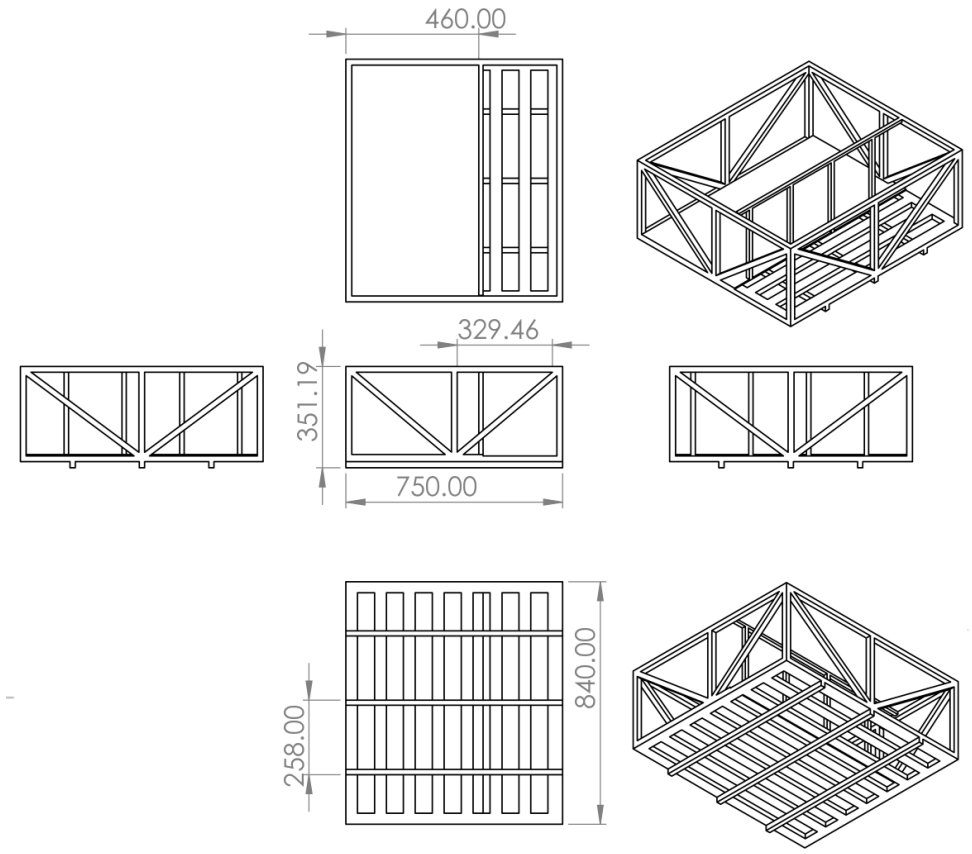

Figure C.5: Technical drawings concerning battery compartment.

C.4 Holding Bars

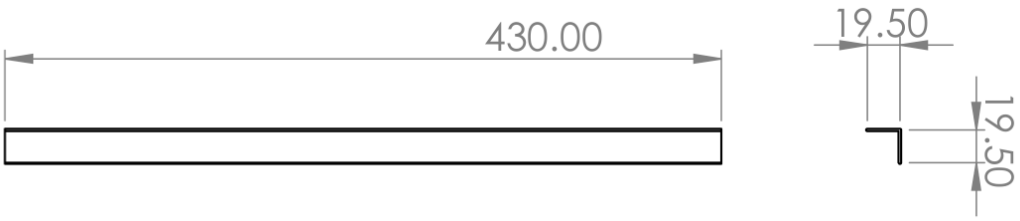

Figure C.6: Technical drawings concerning the L-shaped bar.

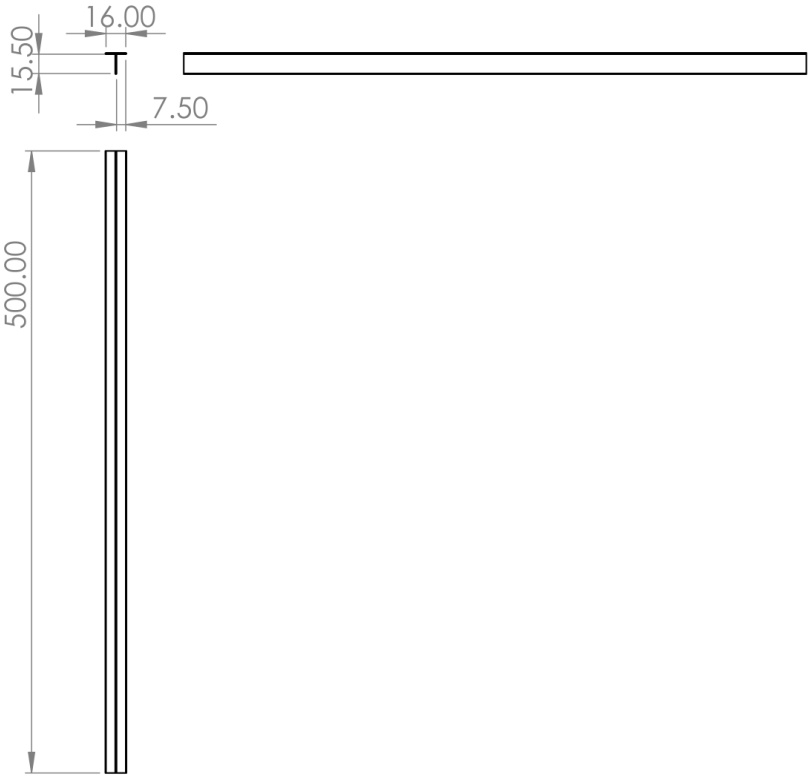

Figure C.7: Technical drawings concerning T-shaped bar.

C.5 Assembly

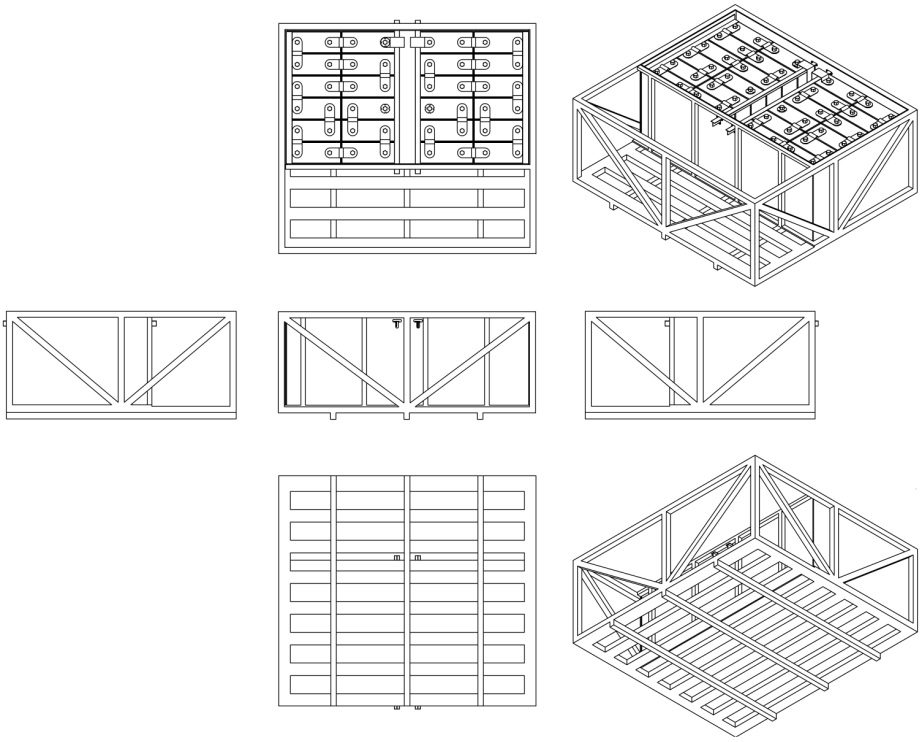

Figure C.8: Technical drawings concerning The full assembly.